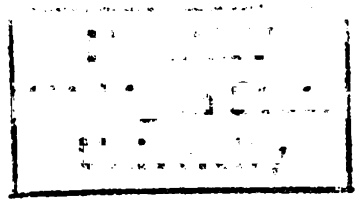

This is to certify that the

thesis entitled

CYCLIC DOWEL ACTION AND PULL-OUT BEHAVIOR OF BEAM REINFORCEMENT AT REINFORCED CONCRETE JOINTS

presented by

Kienuwa Obaseki

has been accepted towards fulfillment
of the requirements for

Ph.D degree in Civil Engineering

Major professor

Date 12/19/85

O-7639

*MSU is an Affirmative Action/Equal Opportunity Institution*

# CYCLIC DOWEL ACTION AND PULL-OUT BEHAVIOR OF BEAM REINFORCEMENT AT REINFORCED CONCRETE JOINTS

BY

Kienuwa Obaseki

AN ABSTRACT OF A DISSERTATION

Submitted to

Michigan State University

in partial fulfillment of the requirements

for the degree of

DOCTOR OF PHILOSOPHY

Department of Civil and Environmental Engineering

1985

ABSTRACT

CYCLIC DOWEL ACTION AND PULL-OUT BEHAVIOR OF BEAM REINFORCEMENT AT REINFORCED CONCRETE JOINTS

by

Kienuwa Osama Obaseki

An integrated experimental-theoretical investigation was performed on the cyclic dowel and pull-out behavior on beam longitudinal bars at beam-column connections.

Dowel tests investigated the behavior of bars with different sizes bearing against the concrete core and cover and their cyclic performance. Analytical models were developed for predicting the ultimate strength and constitutive behavior of dowel bars at beam-column interfaces. Effects of the diameter, yield strength and tensile stresses of bars as well as the compressive strength of concrete, on the behavior of dowel bars were studied analytically.

An improved hysteretic model was developed for the local bond stress-slip relationship, and it was incorporated into a new mathematical model for predicting the cyclic pull-out behavior of the longitudinal beam reinforcement embedded in the interior beam-column connections. This new model is based on the displacement method of analysis, and it is more efficient than the other available models for analysis of bonded bars by computer. Parametric studies were performed on the effects of bar diameter and its yield strength, concrete compressive

strength and the rate of loading on the pull-out behavior of bars in the interior beam-column connections.

Tests were also performed on the pull-out behavior of beam longitudinal bars hooked in the exterior beam-column connections. These tests studied the effects of the bar size, the confinement provided in the column, and the concrete compressive strength on the hook pull-out behavior. An empirical constitutive model was developed for hooks, and it was incorporated into an analytical procedure for predicting the overall behavior of hooked bars. The resulting procedure was used to check the current U.S design guidelines for 90° hooked bars.

To the memory of my father

Aiguokunrueghian Obaseki

and

To my ever loving and caring mother

Ayanor Obaseki

ACKNOWLEDGEMENTS

The present work has been carried out under Dr. Parviz Soroushian to whom the author is most deeply indebted. Dr. Soroushian's contribution to this work are truely priceless and the author wishes to hope that he will continue to be his mentor.

The author is greatful to other members who served on his committee and appreciate their useful suggestions.

Finally, the author is most indebted to his wife Adesuwa for her patience and understanding during the sleepless nights of his doctoral program. The author also wishes to thank his family for their support and prayers.

TABLE OF CONTENTS

LIST OF TABLES

LIST OF FIGURES

## CHAPTER 1

## INTRODUCTION

Fixed-end rotation and sliding shear at beam-column connections [Figure 1.1(a)] are generally considered as some of the major factors influencing the seismic response characteristics of reinforced concrete frames.[33,36,44] Excessive fixed-end rotations and sliding shear deformations in frames under earthquake excitations are not desirable. This is due to the limited amount of hysteretic energy that can be absorbed by these deformations under inelastic loads. The deteriorating nature of the mechanisms resisting fixed-end rotations and sliding shear at joints [dowel action and pull-out behavior of longitudinal bars and aggregate interlocking of crack faces shown in Figure 1.1(b)] is the main factor for such inferior energy absorption capacity.

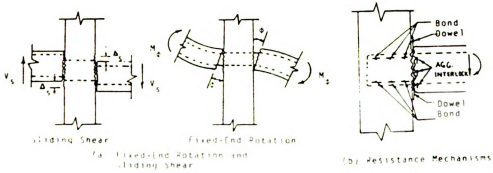


(a) Fixed-End Rotation and Sliding Shear

(b) Resistance Mechanisms

Figure 1.1 Reinforced Concrete Beam-Column Interface Under Seismic Forces

Development of analytical methods for considering the effects of fixed-end rotation and sliding shear in seismic

analysis of reinforced concrete frames is a task yet to be fulfilled. The main problems in this regard are:
(a) Limited understanding of the dowel and pull-out behavior of longitudinal bars and aggregate interlocking of crack faces at beam-column joints under cyclic loads; and
(b) lack of practical methods for simulating these phenomena in structural analysis processes.

The main objectives of the research described herein were to generate experimental data on the dowel action and pull-out behavior of beam longitudinal bars at beam-column connections, and to come up with analytical methods for analyzing these types of behavior. The results are expected to facilitate consideration of fixed-end rotation and sliding shear in nonlinear seismic analysis of reinforced concrete frames.

In the following description of this research project, Chapter 2 reviews the literature on the behavior of dowel bars, and Chapter 3 presents the results of an experimental study that was followed by development of empirical models for the dowel action of beam longitudinal bars under monotonic and cyclic loads at beam-column interfaces.

Chapter 4 summarizes the available literature on the behavior of bonded bars, and Chapter 5 illustrates the results of an analytical study on the pull-out behavior of beam reinforcement in the interior beam-column connections [Figure 1.2(a)]. The study illustrated in Chapter 5 has led to an analytical procedure for predicting the anchored bar

behavior under random cyclic load histories. This procedure is distinguished from the other available ones by its time-efficiency for analysis by computer.

Finally, Chapter 6 presents the results of an integrated exerimental-analytical study on the pull-out behavior of beam longitudinal bars hooked in exterior beam column connections [Figure 1.2 (b)].

The major findings of this research project are summarized in chapter 7.

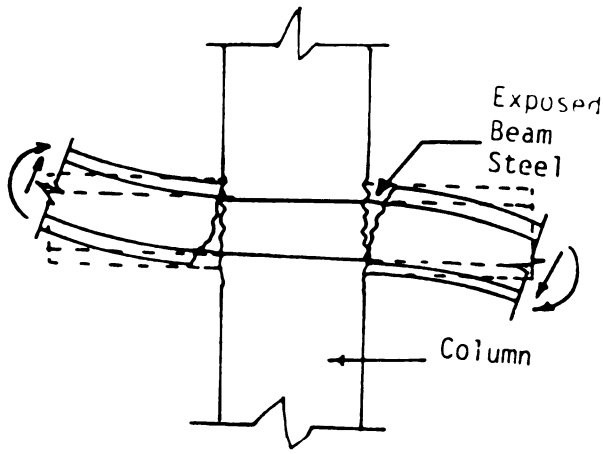


(a) Interior Connection

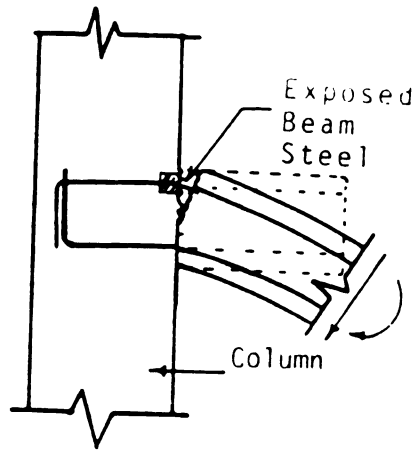


(b) Exterior Connections

Figure 1.2: Interior and Exterior Beam-Column Connections.

# CHAPTER 2

# LITERATURE REVIEW ON DOWEL ACTION OF BEAM LONGITUDINAL BARS AT BEAM-COLUMN INTERFACES

## 2-1 Introduction

The sliding shear deformations at beam-column interfaces [Figure 2.1(a)] are resisted by the dowel action of longitudinal bars and the aggregate interlock between rough faces of the interface crack [Figure 2.1(b)][23,36,44]. Aggregate interlock diminishes rapidly with crack opening,[29,30] and hence dowel bars play a major role in preventing the sliding shear failure.

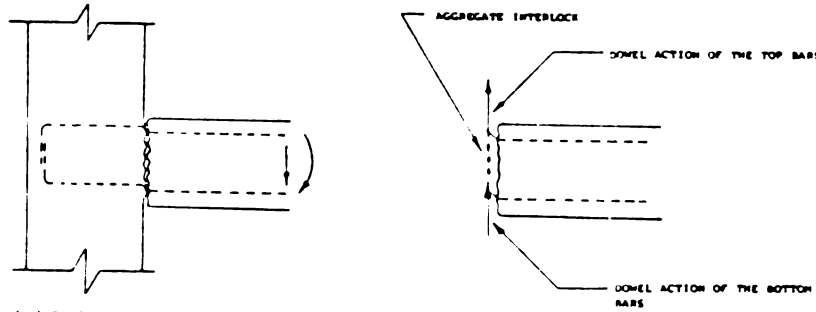


Figure 2.1: Dowel Action at Beam-Column Interface

In studying the dowel action at the beam-column interface, distinction should be made between the action of dowel bars when pushed against the concrete core [bottom bars in Figure 2.1(b)] and when pushed against the concrete cover [top bars in Figure 2.1(b)]. In the first case, when the bar is pushed against the core, the concrete above the bar works like a flexible foundation [Figure 2.2(a)][4,14,29,30,37]. The maximum capacity in this

condition is reached when the bar yields in flexure and concrete fails under the bearing stresses. In the second case, with the bar pushing against the concrete cover, split cracking soon separates the cover from the core, and the dowel bar acts like a beam supported by ties near the interface [Figure 2.2(b)].[4,29,31,36] The maximum capacity in this case is reached when the dowel bar or the tie yields. In both cases, the axial force in the dowel bar reduces the maximum dowel capacity.

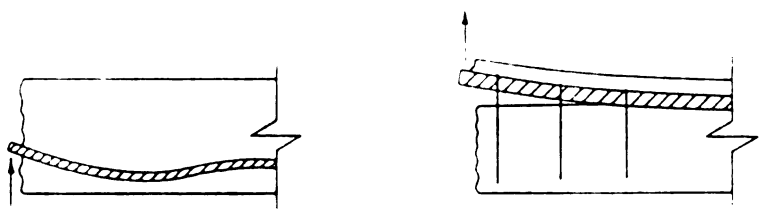

(a) Push Against Core (b) Push Against Cover

Figure 2.2: Dowel Bar Action Against Concrete Core and Against Concrete Cover

## 2-2 DOWEL ACTION AGAINST CONCRETE CORE

**2-2.1 Test Results**: The only two test techniques that closely simulate the dowel action against the concrete core were presented in Ref. 14 [Figure 2.3(a)] and Ref. 37 [Figure 2.3(b)]. In the shear plane of the specimen shown in Figure 2.3(a), aggregate interlock was eliminated by two layers of lubricated brass sheet [thickness = 0.0078 in. (0.20 mm)] placed at the shear plane. The relatively small dowel bars tested in this reference failed by yielding of the bar and crushing of the concrete supporting the bar. A typical dowel force-slip relationship for a test on a 0.39

in. (10 mm) dowel bar with yield strength of 41,890 psi (289.0 MPa) and concrete compressive strength of 4,540 psi that was inclined at an angle of 20° from the line normal to the crack is shown in Figure 2.3(c). The effects of the reinforcement angle, dowel bar diameter, and concrete strength were studied experimentally in Ref. 14. It was concluded that the ultimate dowel force increases noticeably with increasing bar diameter and concrete strength. The effect of the inclination angle of dowel bar was found to be small.

The specimen shown in Figure 2.3(b) represents the action of dowel bars in concrete pavement joint.[37] In this case, the dowel force is directly applied on the bar at a distance from the concrete face. A typical dowel load-dowel deflection diagram obtained in this type of test is shown in Figure 2.3(d) for a dowel bar with a diameter of 0.75 in. (19.0 mm) embedded 6 in. (154 mm) in concrete blocks with a concrete compressive strength of 3,440 psi (23.7 MPa) and a total depth of 8 in. (200.4 mm). Test results in Ref. 37 on dowel bars with 0.75 in. (19.0 mm), 1.00 in. (25.4 mm), 1.50 in. (38 mm), and 2 in. (51 mm) diameters, and different embedment lengths and concrete block depths showed that: (1) Dowel failure is reached as a result of concrete split cracking in the plane of the dowel bar and dowel load; (2) the cracking load is slightly affected by dowel length if this length is greater than eight times the bar diameter; (3) the cracking load increases with increasing concrete

depth underneath the dowel bar; and (4) an increase of the width of the concrete block beyond the width to height ratio of 1.5 does not seem to have any definite influence on the cracking load.

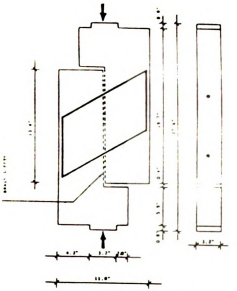

(a) Ref. 14 Test Specimen

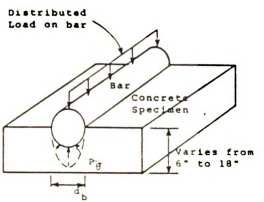


(b) Ref. 37 Test Specimen

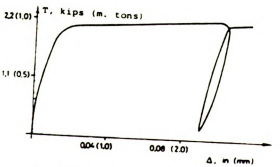


(c) Ref. 14 Typical Test Results

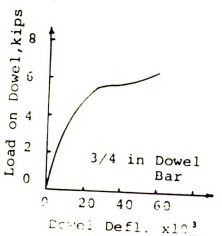


(d) Ref. 37 Typical Test Results

Figure 2.3: Test On Dowel Acting Against Concrete Core.

2-2.2 Ultimate Strength Computation: In order to compute the ultimate strength of dowel bars acting against concrete core, their behavior has been treated as the action of a beam on an elastic foundation [Figure 2.4(a)].[4,14,24,29,37] Using the beam on an elastic foundation theory together with some simplifying assumptions on bearing stress distribution, an equation for ultimate load can be derived. Figures 2.4(b) and 2.4(c) show the actual bearing stress distribution and its simplified distribution pattern used in Ref. 14, respectively. Failure in this model is assumed to be reached when the critical bar section reaches the plastic hinge moment and the stress on concrete reaches the ultimate bearing strength of concrete.

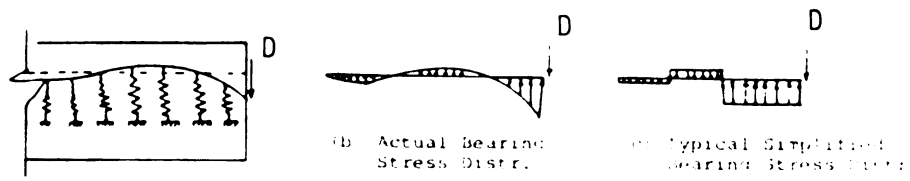


Figure 2.4 Beam on Elastic Foundation Model for Dowel Action Against Concrete Core

Well-developed models that have followed the beam on an elastic foundation idealization,[4,14] have not paid enough attention to the bearing strength of concrete. Ref. 4 assumes a bearing strength of 1.445 times the concrete compressive strength, while Ref. 14 takes the bearing strength to be four times the concrete compressive

strength. Both of these references assumed that the bearing failure under the dowel bar occurs by concrete crushing. This assumption is based on test results reported in Ref. 14 on small-diameter dowel bars. Tests on more common sizes of dowel bars in Ref. 37 have shown that the bearing strength is reached when the concrete underneath the dowel bar splits in the plane formed by the bar and the dowel load. These tests showed that the bearing strength of concrete at split cracking depends on many factors including the dimensions of the loaded area, depth of concrete below the dowel bar, and the tensile strength of concrete. Tests in Ref. 37 disclosed that the ratio of concrete bearing strength to its compressive strength in a 12 in. (304.8 mm) deep specimen is on the average 2.6 for 0.75 in. (19.0 mm) dowel bars, 2.3 for 1 in. (25.4 mm) diameter, 1.8 for 1.50 in. (38.0 mm) diameter, and 1.8 for 2.00 in. (50.8 mm) diameter dowel bars. The bearing strength for six inches deep specimens was from 1.22 to 1.37 times the bearing strength of 12 in. deep specimens, depending on the dowel bar diameter. The bearing strength for 18 in. deep specimen was between 0.98 and 1.09 times the one for 12 in. deep specimens. The shallow blocks seem to have larger bearing strength than the deeper ones ( noting that the specimens simulate a pavement joint with some base friction resisting split cracking).

The other parameter that governs the behavior of the beam on an elastic foundation model of dowel bars acting

against concrete core is the foundation modulus. Different investigators[29,30,37] have concluded from test results that the concrete foundation modulus varies from 750,000 to 2,500,000 psi/in. (203.7 to 679.1 MPa/mm), and a typical value of 1,000,000 psi/in. (271.7 MPa/mm) has been commonly used.

Dowel bars are generally subjected to axial forces, produced by flexural moments (Figure 2.1). The bar axial force reduces its plastic hinge moment, and the bond stresses of a bar subjected to axial tension might produce radial stresses around the bar that tend to accelerate split cracking of concrete under bearing stresses. Ref. 30 suggests that the interaction between the bar axial and dowel forces is negligible for axial forces smaller than 80% of the bar pull-out strength, but it becomes important at higher axial forces. Refs. 14 and 29 suggest that an elliptical interaction formulation can predict test results with reasonable accuracy.

2-2.3 Monotonic Dowel Load-Deflection Formulation: The beam on an elastic foundation theory has been found to be incapable of predicting the inelastic constitutive behavior of dowel bars acting against the concrete core.[4,14] This is probably due to the noticeable effect of the concrete and steel inelasticities, that are not considered when the beam on an elastic foundation model is used for determining dowel deformations. Hence, Refs. 4 and 14 have developed load-deflection expressions by curve fitting to the results

of tests reported in Ref. 14 (Figure 2.5). These tests used unrealistically small dowel bars and thus the empirical models are not necessarily applicable to the commonly used dowel bar sizes. Besides, the constitutive model of Ref. 14 gives dowel load in terms of dowel deflection. If dowel deflection is to be derived in terms of dowel load, as required in the widely used displacement method of analysis, time-consuming iterative methods are needed to achieve this solution. The constitutive model of Ref. 4 gives the dowel deflection in terms of dowel load, but this model is not complete in the sense that the user should input an initial dowel stiffness that should be derived from test results.

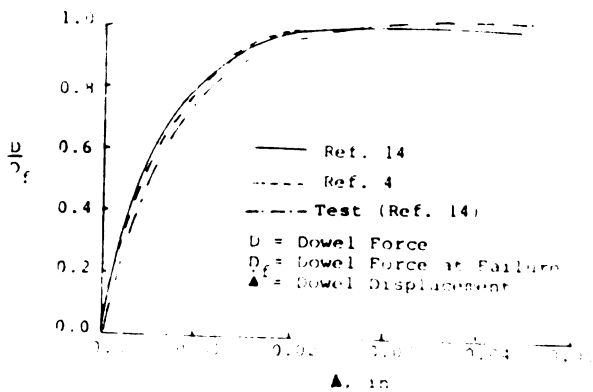


Figure 2.5 Experimental And Theoretical Dowel Load Deflection Relationships For 0.39 in. Diameter Dowel Bar Acting Against Core With f'c of 4,540 psi. (Refs. 4 & 14).

Some investigators[42] have also studied the dowel bar behavior within the crack. The results are applicable to conditions with very wide cracks. Dowel strength in this

case may be derived from three mechanisms: the flexure of the bar [Figure 2.6(a)], the shear force across the bar [Figure 2.6(b)] , and the kinking of the bar [Figure 2.6(c)]. These figures also show the ultimate dowel force in terms of the bar strength. In these figures:

$D_u$ = ultimate dowel strength;

$A_s$ = bar area;

$d_b$ = bar diameter; and

$f_y$ = bar yield strength

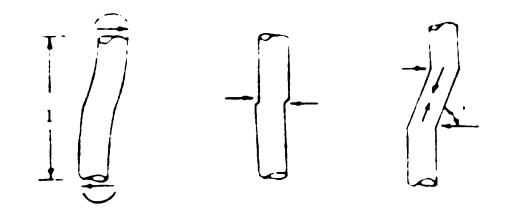


(a) Flexure (b) Shear (c) Kinking

Figure 2.6: Mechanisms of Dowel Action Within the Crack (Ref. 42).

Ref. 29 suggests that the dominant mode of dowel action changes according to the magnitude of dowel force. For very small dowel forces, the force transfered across the crack produces shear deformations in the reinforcement [Figure 2.6(a) above]. At this stage, the bar spans a distance approximately equal to the initial crack width. As the dowel force increases, the bearing stresses induced by the dowel bar on concrete deteriorates the concrete around the bar, and consequently the unsupported length of the dowel

bar increases. Dowel forces are then transfered across the crack primarily by the bending action of the reinforcement [Figure 2.6(a)]. With further increase in dowel force, the unsupported length of the dowel bar decreases and the bar curves around the concrete, and consequently the dowel stiffness increases due to the kinking action [Figure 2.6(c)]. The unsupported length of the dowel bar is thus a difficult parameter to estimate and depends, on the initial crack width, the state of stresses in the concrete surrounding the bar, the level of axial and dowel forces sustained by the reinforcement, and the bar diameter.

## 2-3 DOWEL ACTION AGAINST CONCRETE COVER

**2-3.1 Test Results**: A number of test set-ups have been suggested in the literature for simulating the action of dowel bars against the concrete cover. Ref. 22 used the specimen shown in Figure 2.7(a) to idealize the behavior of a dowel bar acting against cover in a reinforced concrete beam at the closest crack to the support. This reference also suggests the test specimen shown in Figure 2.7(b) for simulating the dowel action between two flexural cracks along the beam span. Ref. 54 used the specimen shown in Figure 2.7(c) for modeling the dowel behavior at the first diagonal crack from the support. The specimen of Figure 2.7(d) has been suggested in Ref. 34 for idealizing the behavior of a dowel bar acting against concrete cover at a beam shear-flexural crack.

On the basis of test results presented in Refs. 8 and

54, it can be concluded that the constitutive behavior of dowel bar acting against the concrete cover after split cracking [Figure 2.2(b)] depends primarily on the spacing of the stirrup closest (supporting the dowel bar) to the crack. Maximum dowel capacity when the first stirrup is spaced further than about one inch (25.4 mm) from the crack was reached when split cracking occurred (curve A in Figure 2.8). In the cases with a stirrup was placed closer than one inch (25.4 mm) to the crack, the dowel load could be increased after split cracking, and the maximum dowel capacity was reached when the stirrup yielded in tension (curve B in Figure 2.8). Figure 2.8 also shows a typical constitutive behavior of dowel bars pushed against concrete core (curve C) that is generally superior to the behavior of dowel bars acting against cover.

From test results on specimens similar to the one shown in Figure 2.7(d), it has been concluded in Ref. 8 that in dowel action against cover, the splitting load increases with increasing beam width, bar diameter, and concrete strength. The beam depth, concrete cover, and crack width did not affect the dowel capacity of the reinforcement. The presence of two layers of reinforcement increased the dowel strength by approximately 40% over that of one layer. Test results presented in Ref. 54 on similar test specimens confirmed the above results and also showed that the distance between the support and the diagonal crack does not affect the dowel capacity. Some results contradicting

the above conclusions have also been presented in the literature. For example in the test results reported in Ref. 27, bar size did not noticeably influence the split cracking load, and Ref. 32 concluded from test results that the split cracking load depends on the concrete cover thickness (especially if the dowel bar is subjected to axial tension).

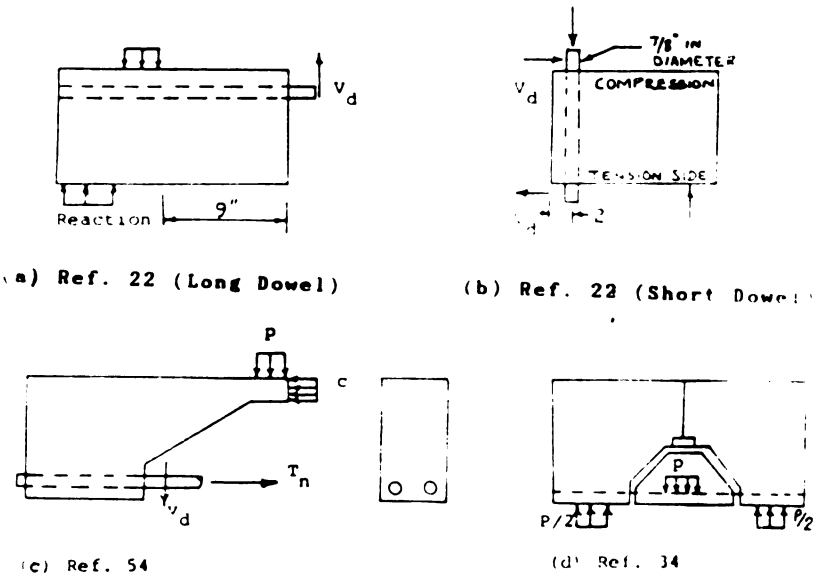


Figure 2.7: Tests On Dowel Bar Acting Against Concrete Cover (Refs. 22, 34, and 54).

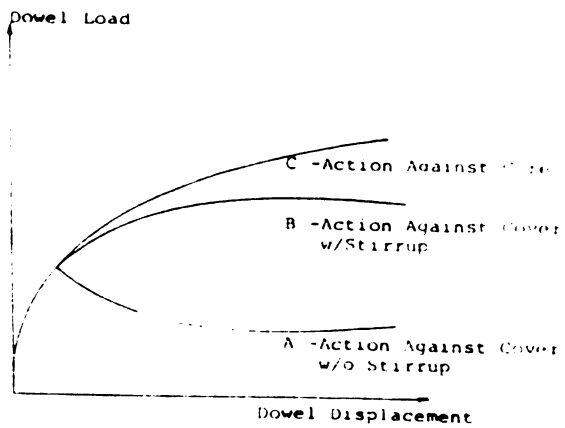


Figure 2.8: Dowel Constitutive Behavior.

Large axial tension (of the order of 80% of the bar pull-out strength) in dowel bars acting against cover also has been observed to reduce the dowel stiffness and strength by cracking the surrounding concrete and also by lowering the bar plastic hinge capacity. Small axial loads, however, have been observed to slightly improve the dowel capacity.[18,27,32,47] Figure 2.9 shows test results from Ref. 47 on the interaction of the dowel and axial forces.

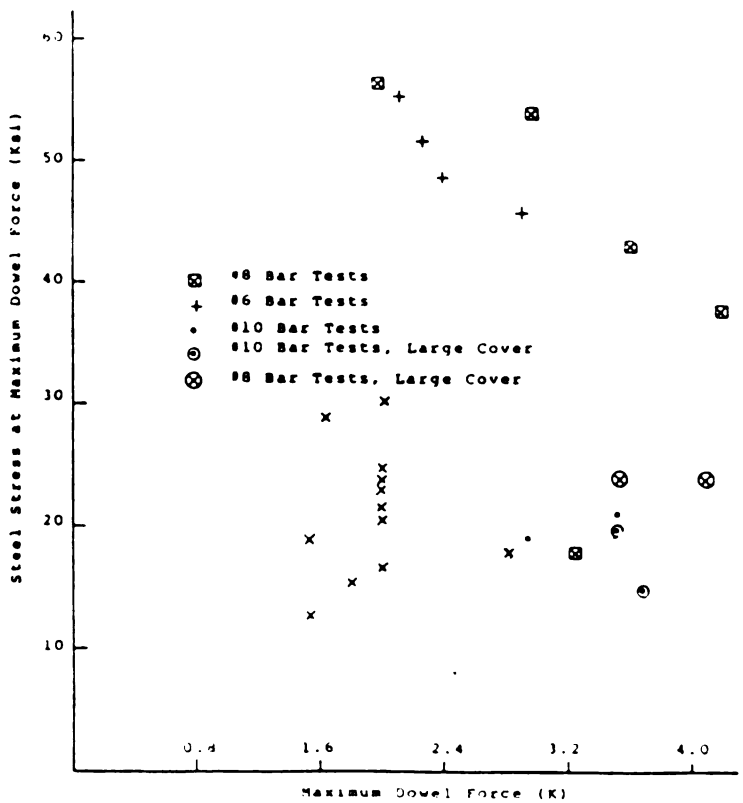


Figure 2.9 Interaction of Axial Stress with Force Acting Against Concrete Cover (Ref. 47)

2-3.2 Dowel Strength and Monotonic Load-Deflection

**Formulations**: Ref. 47 suggest that before split cracking, the dowel bar acting against cover can be idealized as a beam supported by concrete that works as an elastic foundation, and the stirrups that work as flexible supports [Figure 2.10(a)]. The beam in this idealization is composed of the dowel bars together with the concrete cover [Figure 2.10(b)]. Failure in this model takes place by the occurrence of one or a combination of the following actions: split cracking, yielding of the bar, and yielding of the stirrup. A complex formulation based on this theory[10] compares relatively well with experimental results.

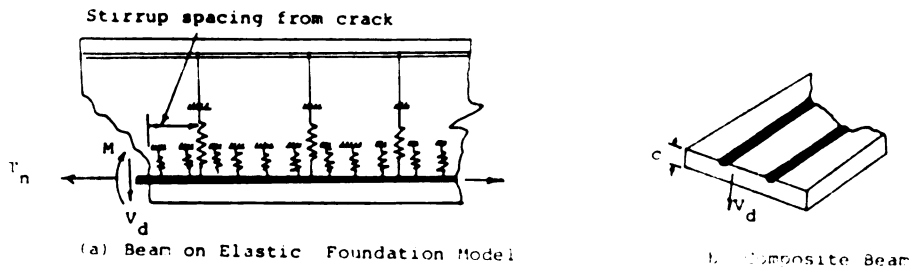


(a) Beam on Elastic Foundation Model

(b) Composite Beam

Figure 2.10: Idealization of Dowel Action Against Concrete Cover (Ref. 31).

For the cases without stirrups, many investigators.[8,22,27,29,30,34,54] have used the above beam on an elastic foundation model [assuming that the idealized beam is either the composite one shown in Figure 2.10(b) or simply the dowel bars acting alone] to derive a simple

expression for the dowel stiffness before cracking as well as the dowel load corresponding to split cracking (that is also the dowel strength for the case without close-by stirrups). The dowel strength in these formulations generally increases proportionally with the available beam width, concrete tensile strength, and in some cases the embedded length of the dowel bar. The dowel stiffness on the other hand depends basically on the dowel bar diameter and modulus of elasticity as well as the concrete foundation modulus. Most of these references assumed that upon split cracking, the dowel deflection starts to increase with a constant dowel load. Ref. 54, however, assumes that upon split cracking the dowel load drops suddenly to 80% of the split load and then remains constant with increasing dowel deflection. Some of these dowel load-deflections and strength formulations for dowel bars acting against concrete cover with no stirrup support are compared in Figure 2.11 for the typical dowel bar shown in this figure.

As far as formulating the interaction of the axial and dowel forces is concerned, an elliptical curve seems to be a simple and accurate idealization of the actual failure condition.[29,32,47]

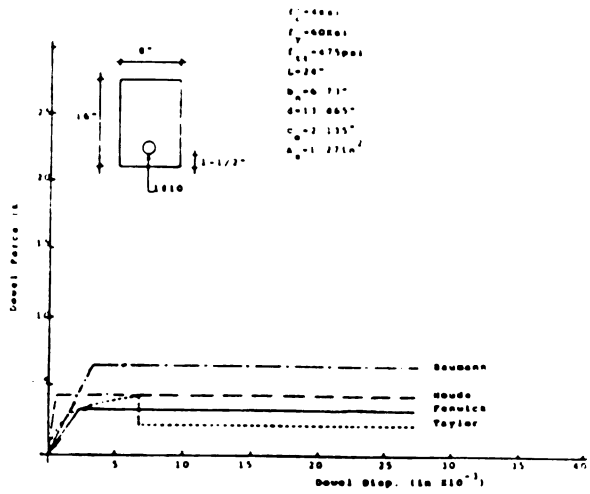

Figure 2.11: Proposed Constitutive Models For Dowel Bars Acting Against Concrete Cover With No Stirrup Supports (Ref. 29).

## 2-4 DOWEL BEHAVIOR UNDER CYCLIC LOADS

**2-4.1 Test Results:** Experimental studies specifically concerned with the behavior of the beam top or bottom longitudinal bars subjected to cyclic dowel loads have not been reported in the literature available to the author. Some cyclic tests, however, have been performed on dowel bars in specimens that simulate the behavior of the reinforcing bars placed in concrete panels [Figure 2.12(a)].[29,30,50]

The aggregate interlock in these specimens was eliminated by means of two 0.01 in (0.25 mm) brass plates placed at the shear plane. Specimens with different dowel bar sizes, numbers and placement configurations were tested. A typical cracking pattern, and the cyclic load

deflection diagram observed in test on a specimen with four #9 bars and concrete compressive strength of about 3,100 psi (21.4 MPa) are shown in Figures 2.12(b) and 2.12(c), respectively.

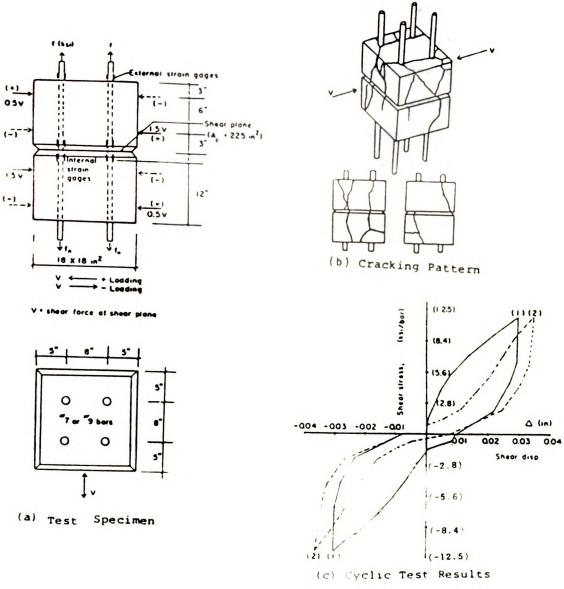


Figure 2.12. Dowel Test Results On Specimens Representing the Reinforced Concrete Panel (Ref. 30)

As shown in Figure 2.12(c), the dowel stiffness deteriorates significantly in the second cycle, and it exhibits a hardening type of behavior (pinching). This indicates permanent distortion and damage in the concrete produced by the dowel force. The concrete degradation was observed to be enhanced by the application of large tensile stresses to the reinforcement and by the presence of shrinkage cracks around the dowel bars. In general, the dowel specimen experienced large deteriorations under the first loading cycle. For subsequent cycles at the same load amplitude, the response tended to stabilize and the rate of degradation decreased with increasing cycle number.

It was also observed that while the area enclosed by the hystersis loop initially decreases with cycles [Figure 2.12(c)], this area increases significantly when the specimen cycles at a shear stress very close to its failure load. The crack width change due to dowel was found to be negligible except for dowel forces near to the ultimate dowel strength. Typical increases in crack width at the maximum shear stress were of the order of 17% of the initial crack width.

In an attempt to justify the stiffness degradation of dowel bars subjected to cyclic loads, Ref. 29 suggests the following illustration. As a result of the high bearing stresses produced by the dowel bar in the vicinity of the crack, the concrete in this area crushes and hence in the second load cycle it can provide support to the dowel bar

only if the dowel deflection is large enough to provide contact between the dowel bar and the uncrushed concrete. After the contact is made, the stiffness of the dowel increases considerably.

2-4.2 Hysteretic Modeling: Two different analytical models for predicting the cyclic behavior of dowel bars have been developed in the literature. The first one[29,30] is a hysteretic model for the dowel action of the panel reinforcement [Figure 2.12(a)]. The first loading cycle is assumed to behave linearly which is true for relatively small dowel loads (Figure 2.13). The subsequent cycles are idealized to be highly non-linear with a pinching type of behavior. This model does not attribute any hysteretic energy dissipation capacity to dowel. It is based on the assumption that the dowel energy dissipation [Figure 2.12(c)] is relatively small when compared with the other sources of energy dissipation in reinforced concrete. The details of the hysteretic model shown in Figure 2.13 have been derived empirically in Ref. 30 using the test data presented in Ref. 29. This model is not directly applicable to the dowel action of the beam longitudinal bars when pushed against the concrete cover [Figure 2.2(b)] that cannot be idealized by the panel test specimen shown in Figure 2.12(a).

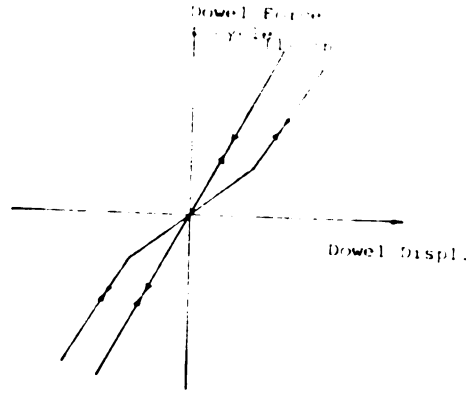


Figure 2.13 Idealization for Dowel Action Experimental Hysteresis (Ref. 29).

Another dowel hysteretic model has been developed in Ref. 36 for the action of the beam dowel bars at the beam-column joint [Figure 2.14(a)]. In the physical idealization of the dowel behavior, the contribution of the concrete cover to the dowel stiffness was neglected, and the dowel bar was assumed to behave like a beam. Some typical boundary conditions of this beam are shown in Figure 2.14(b) for the condition with the bar in contact with either the beam end or the stirrup; in Figure 2.14(c) for the condition with the bar in contact with both the first and the second stirrups; and in Figure 2.14(c) for the condition with the bar in contact with the first stirrup but not the second one. The dowel stiffness in this idealization is then taken equal to the flexural stiffness of the dowel bar with the assumed boundary conditions.

In the research project describe below, an integrated experimental-theoretical approach was adopted for modeling the dowel action of beam longitudinal bars at the beam-

column interface. This involved studies on the behavior of: (a) concrete core under dowel bar bearing stresses, (b) dowel action against core, (c) dowel action against cover, and (d) behavior of dowel bars under cyclic loads.

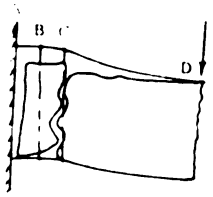


a) Beam-Column Interface (Note Concrete Cover Assumed Crushed)


b) Boundary Conditions For Portion AB With Contact at B


(c) Boundary Conditions For Portion BCD with Contact at C

(d) Boundary Conditions For Portion BCD with no Contact at C

Figure 2.14: The Physical Model For Predicting the Dowel Bar Hysteresis (Ref. 36).

# CHAPTER 3

# EXPERIMENTAL AND ANALYTICAL STUDIES ON DOWEL ACTION OF BEAM LONGITUDINAL BARS AT BEAM-COLUMN INTERFACES

## 3-1 Introduction

The available experimental data on dowel bars applicable to situation of longitudinal beam reinforcements at joints are limited to test results on unrealistically small dowel bars against concrete core. The empirical formulations that are based on this limited test data are not necessarily applicable to the actual conditions of dowel bars at the beam-column connections.

This Chapter illustrates the experimental and analytical studies performed in this research project on the behavior of dowel bars at beam-column connections. First, the studies on the bearing strength and stiffness of concrete core under dowel bars are presented, and then the works on the behavior of dowel bars acting against concrete core are discussed. The rest of this Chapter is devoted to illustrating behavior of dowel bars acting against concrete core and cyclic performance of dowel.

## 3-2 BEARING STRENGTH AND STIFFNESS OF CONCRETE UNDER REINFORCING BARS

3-2.1 Introduction: The ultimate resistance and stiffness of the dowel bars bearing on concrete core (e.g. the bottom beam reinforcement in the condition of Figure 3.1) depends on the bearing strength and the bearing stiffness (foundation modulus) of the concrete core under the action

of the dowel bars.[4,14,30,37]

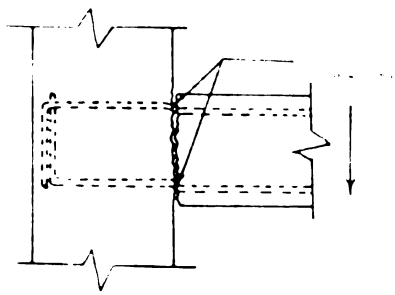

Figure 3.1: Dowel Action of Reinforcing Bars.

Test results on concrete bearing strength are scarce, and consequently the values proposed by different investigators for these two properties of concrete are wide apart. The values suggested for the bearing strength[23,43] range from 1.45 to 4.00 times the concrete compressive strength, and the values of bearing stiffness used by different investigators[30,38(b)] range from 750 ksi/in. (203.7 MPa/mm) to 4,000 ksi/in. (1,244.1 MPa/mm).

Experimental data on the behavior of dowel bar under concrete bearing stresses was obtained, and empirical expressions were derived for the bearing strength and stiffness of concrete.

3-2.2 Test Program: The specimen shown in Figure 3.2(a) was designed to simulate the behavior of dowel bars bearing against concrete core. The properties of the test specimens are summarized below in Table 3-1. A total of 33 tests were performed for studying the effects of the following variables on the bearing behavior of concrete: (a) the bar diameter (series II tests); (b) the concrete strength

(series III tests); (c) the width of the concrete block (series IV tests); (d) the depth of the concrete block (series V tests); (e) the embeddment length of the dowel bar (series VI tests); (f) the number of dowel bars [Figure 3.2(b), series VII tests]; and (g) confinement of the concrete block [Figure 3.2(c), series VIII tests].

All the specimens were constructed with type III Portland cement and normal-weight aggregate. The maximum size of the aggregate was 3/4 in. The specimens were covered with plastic in their wood forms for 24 hours. The forms were then removed and the specimens were placed in a moist room with 72°F (22.2°C) temperature and 100% humidity. After 5 days, the specimens were exposed to the regular lab environment and they were tested at the age of 25$\pm$ 2 days. The values of concrete strength specified in Table 3-1 were recorded at the test age.

The test set-up is shown in Figure 3.3. The load was applied quasi-statically by a hydraulic testing machine, and the tests were all load-controlled. The load was distributed uniformly along the length of the dowel bar, and the bottom surface of the specimen was greased in order to prevent development of frictional forces. The penetration of the dowel bar into the concrete under load was measured by two electrical displacement transducers as shown in Figure 3.3. The errors in both displacement and force measurements were smaller than 1%.

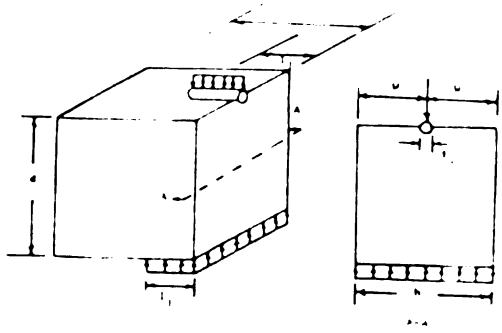

(a) General Geometry

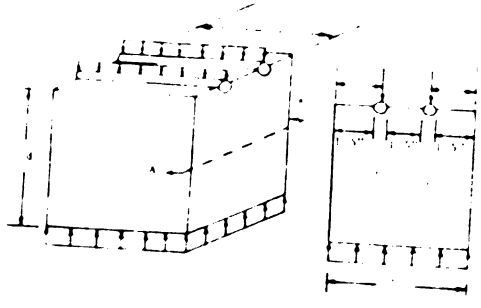

(b) Multiple-Bar Specimen

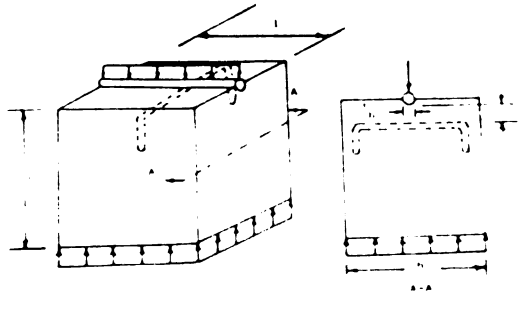

(c) Confined Specimen

Figure 3.2: Test Specimens of Bearing Strength

Table 3.1 Properties of Test Specimens & Results On Bearing Strength of Concrete

| Series | | b (in) | d (in) | t (in) | $t_1$ (in) | w (in) | $d_b$ (in) | $f'_c$ (ksi) | $f_b$ (ksi) | $K_f$ (ksi/in) | Comments |
|---|---|---|---|---|---|---|---|---|---|---|---|
| I | | 6 | 9 | 6 | 6 | 3.0 | 1.00 | 5.84 | 10.67 | 365 | -------- |
| | | 6 | 9 | 6 | 6 | 3.0 | 1.00 | 6.00 | 11.00 | 457 | -------- |
| II | BAR DIAMETER | 6 | 9 | 6 | 6 | 3.0 | 0.50 | 5.60 | 16.00 | 571 | -------- |
| | | 6 | 9 | 6 | 6 | 3.0 | 0.50 | 5.60 | 15.00 | 578 | -------- |
| | | 6 | 9 | 6 | 6 | 3.0 | 0.75 | 5.60 | 12.11 | 368 | -------- |
| | | 6 | 9 | 6 | 6 | 3.0 | 0.75 | 5.60 | 14.44 | 407 | -------- |
| | | 6 | 9 | 6 | 6 | 3.0 | 1.25 | 5.76 | 10.59 | 265 | -------- |
| | | 6 | 9 | 6 | 6 | 3.0 | 1.25 | 5.76 | 10.43 | 258 | -------- |
| III | CONCRETE STRENGTH | 6 | 9 | 6 | 6 | 3.0 | 1.00 | 3.63 | 7.83 | 239 | -------- |
| | | 6 | 9 | 6 | 6 | 3.0 | 1.00 | 3.63 | 7.67 | 290 | -------- |
| | | 6 | 9 | 6 | 6 | 3.0 | 1.00 | 5.47 | 11.25 | 308 | -------- |
| | | 6 | 9 | 6 | 6 | 3.0 | 1.00 | 5.47 | 9.25 | 281 | -------- |
| | | 6 | 9 | 6 | 6 | 3.0 | 1.00 | 5.47 | 11.08 | 308 | -------- |
| IV | BLOCK WIDTH | 3 | 9 | 6 | 6 | 1.5 | 1.00 | 6.76 | 9.67 | 306 | -------- |
| | | 3 | 9 | 6 | 6 | 1.5 | 1.00 | 6.68 | 8.00 | 265 | -------- |
| | | 9 | 9 | 6 | 6 | 4.5 | 1.00 | 6.76 | 10.58 | 281 | -------- |
| | | 9 | 9 | 6 | 6 | 4.5 | 1.00 | 5.60 | 13.30 | 364 | -------- |
| V | BLOCK DEPTH | 6 | 6 | 6 | 6 | 3 | 1.00 | 6.76 | 8.70 | 271 | -------- |
| | | 6 | 6 | 6 | 6 | 3 | 1.00 | 6.76 | 10.04 | 416 | -------- |
| | | 6 | 12 | 6 | 6 | 3 | 1.00 | 5.76 | 9.50 | 340 | -------- |
| | | 6 | 12 | 6 | 6 | 3 | 1.00 | 5.76 | 8.75 | 276 | -------- |
| VI | BAR LENGTH | 6 | 9 | 6 | 2 | 3 | 1.00 | 5.84 | 16.25 | 578 | -------- |
| | | 6 | 9 | 6 | 2 | 3 | 1.00 | 5.84 | 21.25 | ** | -------- |
| | | 6 | 9 | 6 | 4 | 3 | 1.00 | 6.68 | 14.50 | 378 | -------- |
| | | 6 | 9 | 6 | 4 | 3 | 1.00 | 6.68 | 13.25 | 471 | -------- |
| VII | # OF BARS | 6 | 9 | 6 | 6 | 2 | 1.00 | 5.75 | 8.75 | 216 | Two Dowel Bars |
| | | 6 | 9 | 6 | 6 | 2 | 1.00 | 5.75 | 8.79 | 216 | Two Dowel Bars |
| | | 8 | 9 | 6 | 6 | 2 | 1.00 | 5.75 | 10.61 | 188 | Three Dowel Bars |
| | | 8 | 9 | 6 | 6 | 2 | 1.00 | 5.75 | 8.19 | 229 | Three Dowel Bars |
| VIII | CONFINEMENT | 6 | 9 | 6 | 6 | 3 | 1.00 | 6.72 | 12.67 | 326 | One Confining Bar |
| | | 6 | 9 | 6 | 6 | 3 | 1.00 | 6.72 | 12.85 | 322 | One Confining Bar |
| | | 6 | 9 | 6 | 6 | 3 | 1.00 | 6.72 | 12.21 | 306 | Two Confining Bars |
| | | 6 | 9 | 6 | 6 | 3 | 1.00 | 6.72 | 19.15 | 480 | Two Confining Bars |

** Not measured

3-2.3 Test Results: All the specimens behaved elastically up to failure, and failure in the unconfined specimens occurred suddenly when the dowel bar together with a concrete wedge underneath it pushed into the specimen and produced a split crack (Figure 3.4). In general the split crack divided the concrete block into two roughly symmetric segments [Figures 3.5(a) and 3.5(b)], but in the case that the embedded length of the dowel bar was much shorter than

the total block length, the crack pattern was similar to the one shown in Figure 3.5(c).

Failure in the multiple bar specimens was also caused by split cracking of concrete in the plane of each of the bars (Figure 3.6), with no significant interactions between the bars.

Failure in the confined specimen was relatively ductile and the confining bar crossing the split crack prevented a sudden drop in the bearing resistance of the specimen after split cracking. The load dropped gradually in these confined specimens, and transfer of bearing stresses to the confining bars finally resulted in split cracks in the plane of the confining bars (as shown in Figure 3.7 for a specimen confined with two bars).

The values of bearing strength ($f_b$) and bearing stifness ($k_f$) obtained in tests are given in Table 3-1. The bearing strength was derived by dividing the failure load by the projected area of the dowel bar on concrete [$f_b$ = failure load/$l_1 d_b$ in Figure 3.2(a)], and the bearing stiffness was defined as the slope of the bearing stress-bearing deflection diagram (that was found in tests to be linear). The bearing strength obtained in tests ranged from 1.2 to 3.0 times the concrete compressive strength, and the bearing stiffness was between 200 and 600 Ksi/in (54.3 to 163.0 MPa/mm).

Figure 3.3: Test Set-up.

Figure 3.4: Split Cracking of the Specimen.

(a) Fully Embedded Bar.

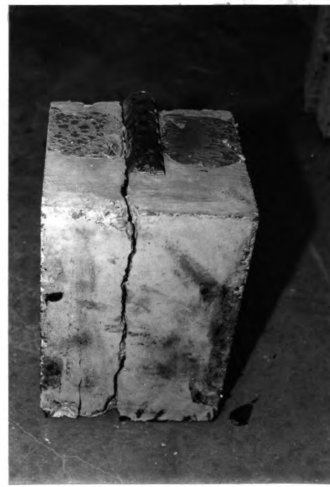

(b) Long, Partially Embedded Bar.

(c) Short, Partially Embedded Bar.

Figure 3.5: Crack Pattern in Different Specimens.

Figure 3.6: Split Cracking of Multiple Bar Specimen.

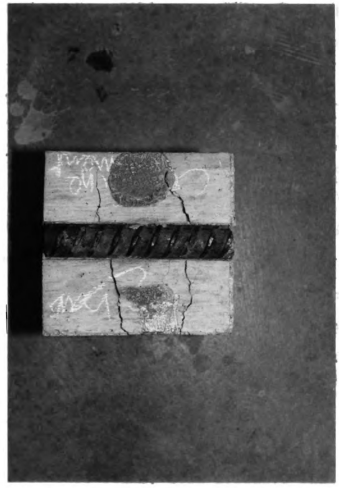

Figure 3.7: Failure of Confined Concrete.

From the test results presented in Table 3-1, it can be concluded that: (a) both the bearing strength and the bearing stiffness of concrete under dowel bars increases with decreasing bar diameter and increasing compressive strength; (b) with increasing width of the concrete block or decreasing the embedded length of dowel bars, the bearing strength tends to increase while the bearing stiffness remain unchange; (c) neither the bearing strength nor the bearing stiffness was sensitive to variations in the specimen depth; (d) when more than one bar with clear spacing of one inch (25.4 mm) was bearing against concrete, the bearing strength is still close to the bearing strength of specimens with a single dowel bar, whereas the bearing stiffness was reduced in the case of multiple-bar specimens; (e) confinement that has favorable effect on the ductility of concrete under bearing stresses, did not considerably influence the concrete bearing strength or stiffness.

**3-2.4** Empirical Equations: The values of bearing strength obtained in tests on unconfined concrete specimens are shown in Figure 3.8. This figure also presents the results of two earlier test programs on similar specimens: one with rectangular plates (instead of dowel bars) bearing against unconfined concrete[26(a)], and the other with dowel bars bearing on unconfined concrete blocks with frictional forces resisting split cracking at their bottom faces.[37] The bearing strength in both of these earlier

investigations are seen in Figure 3.8 to be larger than the values obtained in this study.

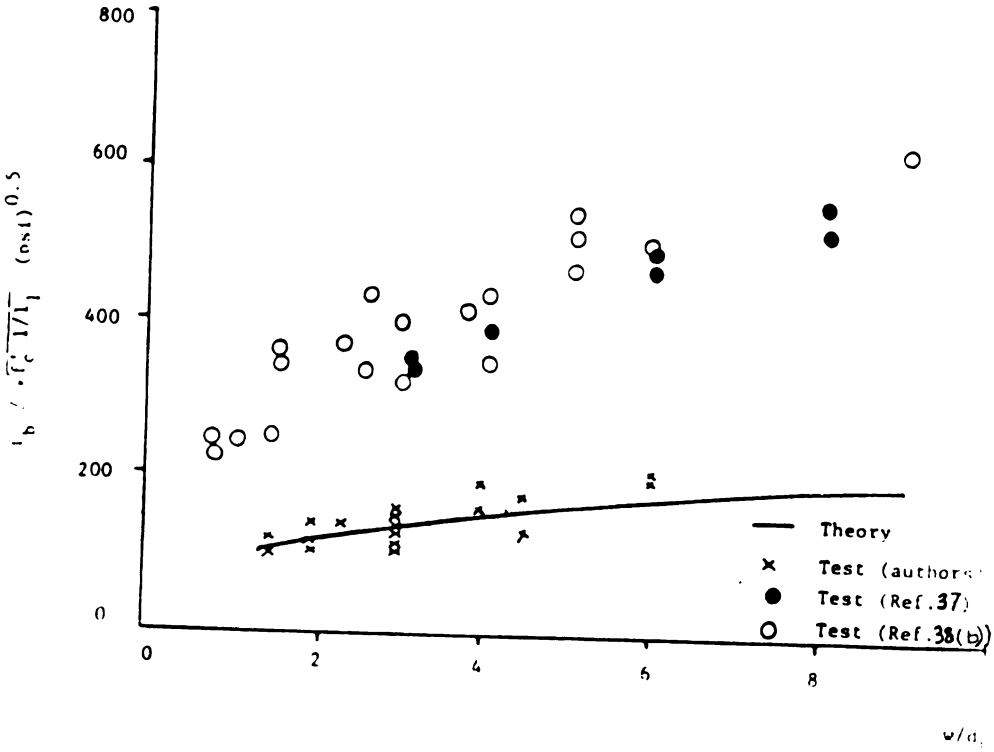


Figure 3.8 Bearing Strength of Concrete.

The trend of the test results can be represented by the following equation (see Figure 3.8):

$$f_b = \begin{cases} 96\sqrt{f_c' l/l_1}\,(w/d_b)^{1/3} & \text{if } f_c' \text{ in psi} \\ 8\sqrt{f_c' l/l_1}\,(w/d_b)^{1/3} & \text{if } f_c' \text{ in MPa} \end{cases} \qquad (3\text{-}1)$$

where: $f_b$ = concrete bearing strength;

$f_c'$ = concrete compressive strength; and other variables are described in Figure 3.2

It should be noticed that due to the limited range of variables in tests, it seems reasonable to limit the ratios of $l/l_1$ and $w/d_b$ in Eqn. (3-1) to 4.0 and 8.0, respectively. Further test results are also needed for studying the effects of confinement on the bearing strength.

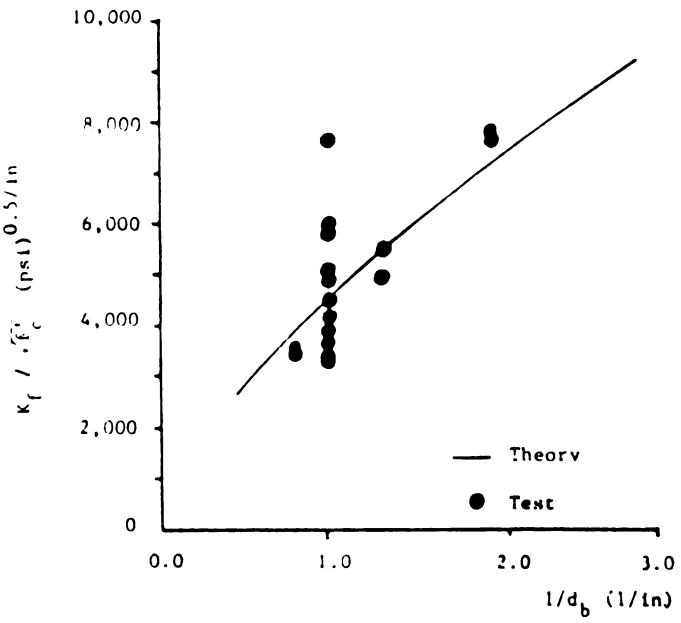


Figure 3.9 Bearing Stiffness of Concrete

The bearing stiffness values derived from tests conducted on unconfined specimens with a single dowel bar are shown in Figure 3.9. The trend of test results can be represented by the following equation that is also shown in

Figure 3.9:

$$k_f = \begin{cases} 4500C_1 f_c'(1/d_b)^{2/3} & \text{if } f_c' \text{ in psi, } d_b \text{ in inches} \\ 127C_1 f_c' (1/d_b)^{2/3} & \text{if } f_c' \text{ in MPa, } d_b \text{ in mm} \end{cases} \quad (3\text{-}2)$$

where: $k_f$ = concrete bearing stiffness (foundation modulus);

$f_c'$ = concrete compressive strength;

$d_b$ = bar diameter; and

$C_1$ = a coefficient ranging from 0.6 for a clear bar spacing of one inch to 1.0 for large bar spacings.

More test data are needed to check the valididy of the above equation outside the range of variables used in this experimental study.

**3-3 BEHAVIOR OF DOWEL BARS IN ACTION AGAINST CONCRETE CORE**

**3-3.1 Test Program**: The reinforcement in a typical specimen tested in this study is shown in Figure 3.10. The shear plane in this specimen was 6 in. (152.4 mm) by 12.5 in. (317.5 mm) in cross-section, and two 0.008 in. (0.203 mm) greased brass plate were used to eliminate the aggregate interlock at this plane. The shear resistance at shear plane was provided by two dowel bars shown in Figure 3.11(a). These bars simulate the dowel action of two identical longitudinal beam reinforcing bars. When the specimen is subjected to compression in the shear plane, the top bar in Figure 3.11(a) in the left hand side block acts like a beam longitudinal bar with 2 in. (5.08 mm) cover

that acts against the beam core. This is also true for the bottom bar in the right hand side of the block. The right side of the top bar as well as the left side of the bottom bar, represent the dowel bar continuation into the column where the bar is well-surrounded by concrete.

Figure 3.11(b) shows the section A-A through shear plane of the specimen. The blocks on the two sides of the specimen were sufficiently reinforced such that failure could not precede failure under dowel forces.

Three specimens were tested under compression, and they were designed to overcome the shortcomings of the test program reported in Ref. 14 on specimens with unrealistically small dowel bars (diameter less than 0.546 in. or 13.9 mm). The dowel bars used in this study were #4, #6, and #8 grade 60 deformed bars. The average compressive strength of concrete in the specimens was 6,400 psi (44.1 MPa) at test age. The specimens were constructed with type III Portland cement, and water/cement ratio was 0.5. The concrete air content was 2 % on the average, and its average slump was 1.5 in. (38.1 mm). The specimens were removed from their wood moulds after 24 hrs, and were placed in a curing room with 72°F (22.2°C) temperature and 100% relative Humidity for 7 days. The test specimens were then exposed to the uncontrolled laboratory environment, and were tested at the age of 28 days.

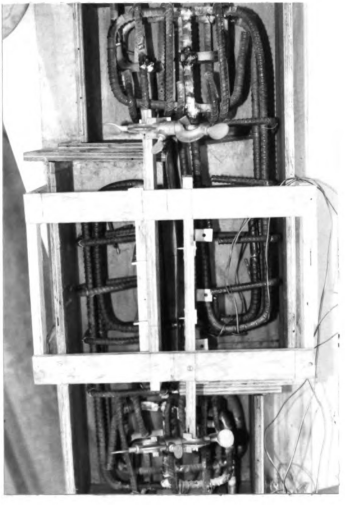

Figure 3.10: Typical Specimen Reinforcement.

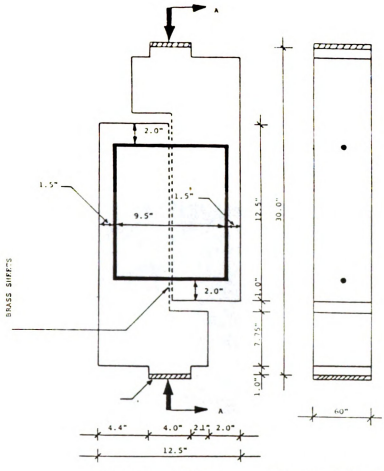


(a) Dowel Bars (b) Section A-A

Figure 3.11: Test Specimen Under Compression Load.

The compressive load was applied by a hydraulic actuator (Figure 3.12), and the load was measured by a load cell. Measurements during tests were made on the crack opening ( with two electrical displacement transducers) and the relative slippage of the two concrete faces at the shear plane (with two other electrical displacement transducers). The dowel bar strain was also measured at three points near the shear plane with electrical strain

gages. Locations of the load cell, displacement transducers and the strain gages are shown in Figure 3.13. The maximum error in the displacement transducer readings was 0.4 %, and the load cell was capable of reading loads with an accuracy of 0.2%.

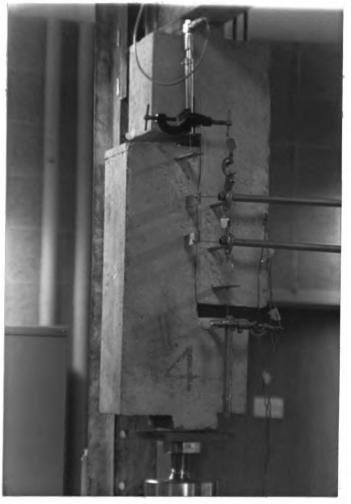

Figure 3.12: Test Set-Up For Dowel Action Against Core.

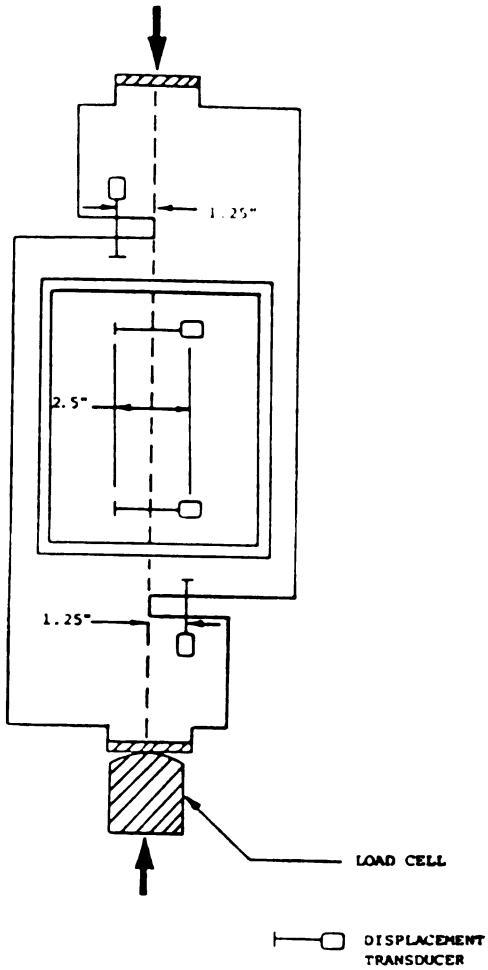


Figure 3.13 Specimen Instrument.

**3-3.2 <u>Test Results</u>: Figures 3.14(a), 3.14(b), and 3.14(c) show the dowel load-dowel displacement curves obtained in the test on #4, #6, and #8 dowel bars, respectively. These figures also show some theoretical predictions that will be disscussed later.**

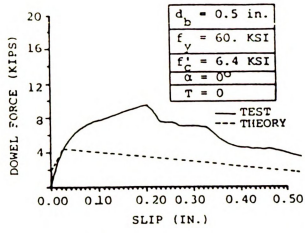


(a) #4 Dowel Bar

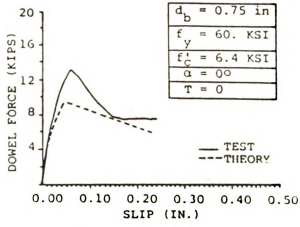


(b) #6 Dowel Bar

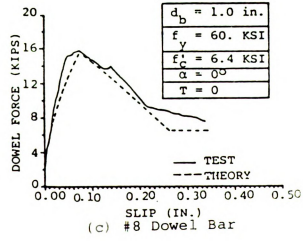


(c) #8 Dowel Bar

Figure 3.14: Dowel Load-Dowel Deflection Relationships.

Figures 3.15(a), 3.15(b), and 3.15(c) present the dowel load-crack opening curves obtained in tests on #4,#6, and #8 dowel bars, respectively.

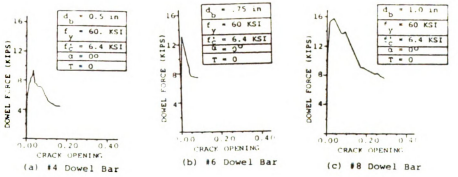


Figure 3.15: Dowel Load Crack Opening Relationships

The maximum capacity of all three bars in action against concrete core was reached when a split crack appeared in the plane formed by the dowel load and the dowel bar. Figure 3.16 shows the split crack of the blocks of a specimen (with the other block removed). Occurrence of this split crack has not been reported in Ref. 14 for tests on small-diameter dowel bars with low yield strength. According to this reference, the maximum dowel capacity in action against concrete core was reached when the concrete underneath the bar crushed and the dowel bar itself yielded. Strain gage readings in tests revealed that yielding occurred in all the dowel bars at about the same time that the maximum dowel capacity was reached.

An important observation in Figure 3.14 is that while #4 dowel bar after reaching its maximum capacity can still resist considerable dowel loads up to relatively large dowel displacements, dowel bars, #6, and #8, show a rather sudden drop in their resistance just after reaching the maximum dowel capacity. The behavior of #6, and #8 dowel bars after reaching their maximum capacity invalidates the assumption made in the available dowel load-deflection models[4,14] according to which there is no loss in dowel bar capacity after failure.

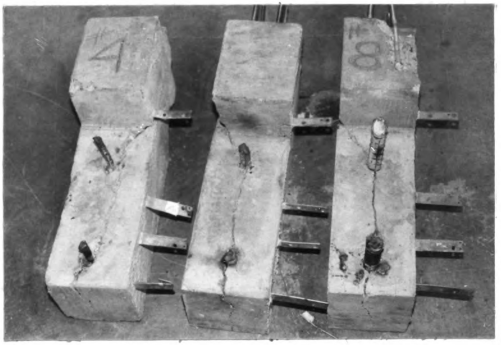


Figure 3.16: The Split Crack Observed at Maximum Dowel Capacity.

The measured crack openings shown in Figure 3.15 are observed to be small prior to reaching the maximum dowel capacity. Thereafter, the crack starts to widen in an increasing rate. Very small crack openings before the maximum dowel strength is reached might be attributed to the slight out-of-straightnesses of the two crack surfaces. The increase in crack opening after maximum dowel capacity (Figure 3.15), might be caused by the kinking action of dowel bars [Figure 2.6(c)].

3-3.3 Formulation of Dowel Strength:

The action of a dowel bar against concrete core [Figure 3.17(a)] is assumed to be similar to the action of a beam (dowel bar) on an elastic foundation ( the surrounding concrete) as shown in Figure 3.17(b). The distribution of stresses on concrete as well as the moment in the reinforcement as predicted by the beam on elastic foundation theory are also shown in Figure 3.17(b).[13]

According to the beam on elastic foundation theory[13], the maximum moment in the dowel bar occurs at a distance x from the crack(where c = 0) given by the following expression:

$$x = \pi/4\beta \qquad (3\text{-}3)$$

where:

$$\beta = \sqrt[4]{\frac{K}{EI}}$$

E = dowel bar modulus of elasticity

I = dowel bar moment of inertia

$d_b$ = $d_b^4/64$

= bar diameter

K = elastic foundation stiffness per unit length [ unit = force/(length)$^2$ ]

= $k_f d_b$

$K_f$ = concrete foundation modulus

[ unit = force/(length)$^3$ ]

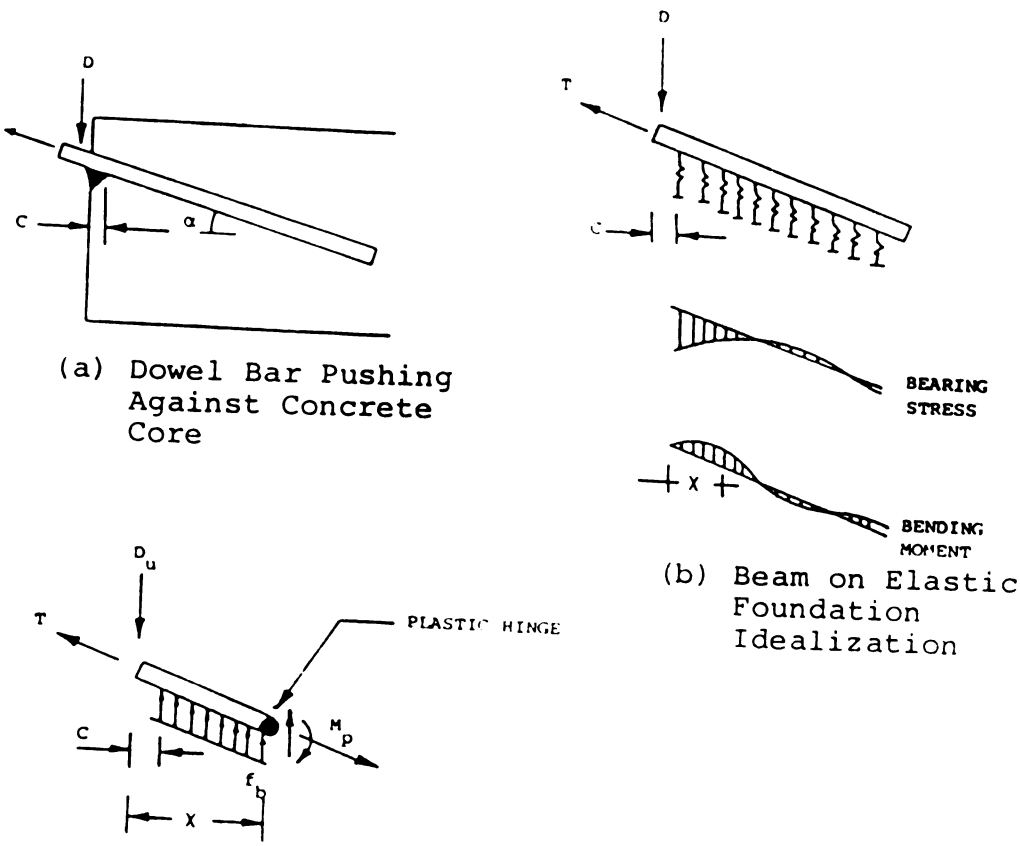


Figure 3.17: Dowel Action Idealization.

Failure in this model is assumed to occur when the dowel bar develops a plastic hinge at the point of maximum moment, and the surrounding concrete reaches its bearing strength marked by the development of the split crack shown in Figure 3.16. It is assumed in this study that concrete bearing stresses between the crack and the plastic hinge are uniformly distributed at a value equal to the concrete bearing strength ($f_b$). The assumed failure condition is shown in Figure 3.17(c). The assumed uniform bearing stress distribution can be justified by inelastic stress redistributions.

The dowel force $D_u$ can now be derived by satisfying equilibrium of moments around the plastic hinge in Figure 3.17(c):

$$D_u = 0.5\, f_b\, (0.37\gamma\, d_b - c)^2 + 0.45\, f_y\, d_b^2\, (1-T^2/T_y^2)/\gamma \qquad (3\text{-}4)$$

where: $\gamma = \sqrt[4]{E_s/K_f d_b}$ ;

$c$ = length of the crushed concrete zone ( derived empirically in Ref. 14)

$= 0.05\, f_y\, d_b \sin\alpha / f_c'$ ;

$K_f$ = concrete foundation modulus ( $10^6$ psi/in or 271.7 MPa/mm);

$d_b$ = dowel bar diameter;

$E_s$ = dowel bar modulus of elasticity ( 29 x $10^6$ psi or 2 x $10^5$ MPa);

$f_b$ = concrete bearing strength [ Eqn. (3-1)]

$f_y$ = dowel bar yield stress;

$T$ = dowel bar axial force;

$T_y$ = dowel bar yield axial force;

$f_c'$ = concrete compressive strength; and

$\alpha$ = angle of inclination of dowel bar to line normal to crack plane.

Values of concrete bearing strength ($f_b$) and its foundation modulus can be derived from Eqns. (3-1) and (3-2), respectively. The value of $l_1$ in Eqn. (3-1) is equal to x derived from Eqn. (3-3).

3-3.4 Formulation of Dowel Load-Deflection Relationship:

This section illustrates the steps taken in this study for producing an empirical expression for dowel load (D) versus the dowel bar deflection at the point of load application (S) for dowel bars acting against concrete core. In this derivation, first a relationship was found between the dowel deflection at the instant when ultimate dowel load was reached ($S_u$) and the ultimate dowel load ($D_u$). This relationship was based on results of the three tests perfomed in this study as well as the 15 tests of Ref. 14:

$$S_u = 4.26 \times 10^{-6} D_u + 0.00945 \qquad (3\text{-}5)$$

Figure 3.18 shows that the above linear relationship which fits very well to test results.

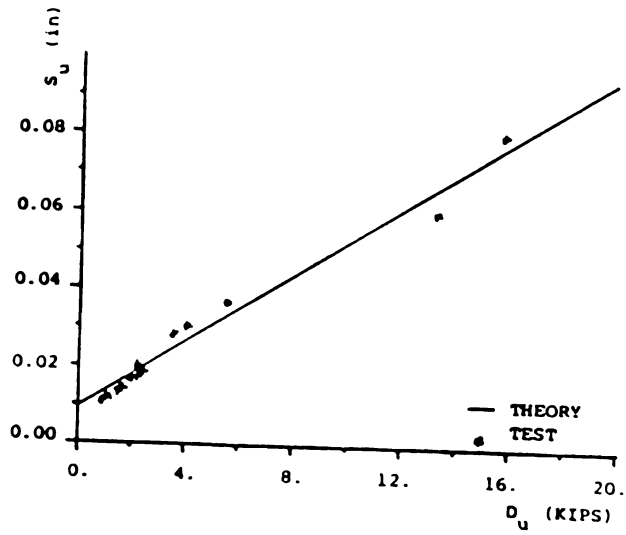


Figure 3.18: Relationship Between Dowel Strength and Corresponding Dowel Deflection.

The following constitutive model was derived by least curve square fitting to the two branches of the three test results performed, as well as the results of 15 tests reported in Ref. 14. With the value of $S_u$ known from the above equation, the dowel load-deflection relationship can be found from the following equation that is developed by

curve fitting to results of 18 tests performed by the author and other investigators.[14]

The following equation was derived empirically to predict the load-deflection diagram:

$$D = \begin{cases} D_u (S/S_u)^{0.5} & \text{for } S < S_u \\ D_u - D_u (S-S_u)/(0.4/d_b - S_u) > 0.4D_u & \text{for } S > S_u \end{cases} \quad (3\text{-}6)$$

where: D = dowel load;

S = dowel displacement;

$D_u$ = ultimate dowel load in action against core [Eqn. (3-4)];

$S_u$ = displacement at ultimate dowel load in action against core [Eqn. (3-5)];

$d_b$ = bar diameter.

The ultimate dowel strengths obtained from Eqn (3-4) are compared in Table (3-2) with the results of 15 tests reported in Ref. 14 as well as the three test results produced in this study. Comparison between test and theory is found to be quite reasonable.

A typical comparison between the dowel load-deflection diagram as predicted by Eqn 3-6 and those obtained in tests of Ref. 14 (test no. 8 in Table 3-2) is shown in Figure 3.19, and Figures 3.14(a), 3.14(b), and 3.14(c) also compare prediction of Eqn. 3-6 with test results produced in this study. The comparison between test and theory is observed in these figures to be reasonable. The extra strength of dowel bar #4 at large slips might have resulted

from the kinking action [Figure 2.6(c)] that was observed to be significant in dowel bar #4.

Table 3-2: Comparison of Experimental & Theoretical Dowel Strength

| Specimen No. | Bar size (in) | $f'_c$ (psi) | $f_y$ (psi) | a | T | Dowel Strength (lb) Test | Theory | Theory/Test |
|---|---|---|---|---|---|---|---|---|
| 1 (Ref.14) | 0.39 | 4540 | 41890 | 10 | 0 | 2381 | 2020 | 0.87 |
| 2 (Ref.14) | 0.39 | 4540 | 41890 | 10 | 0 | 2271 | 2070 | 0.91 |
| 3 (Ref.14) | 0.2535 | 4260 | 35070 | 20 | 0 | 948 | 894 | 0.94 |
| 4 (Ref.14) | 0.2535 | 4260 | 35070 | 20 | 0 | 882 | 894 | 1.01 |
| 5 (Ref.14) | 0.39 | 1420 | 41890 | 20 | 0 | 1720 | 1181 | 0.69 |
| 6 (Ref.14) | 0.39 | 1420 | 41890 | 20 | 0 | 1102 | 1181 | 1.07 |
| 7 (Ref.14) | 0.39 | 4540 | 41890 | 20 | 0 | 2205 | 1908 | 0.87 |
| 8 (Ref.14) | 0.39 | 4540 | 41890 | 20 | 0 | 2712 | 1908 | 0.70 |
| 9 (Ref.14) | 0.39 | 4540 | 41890 | 20 | 0 | 2205 | 1908 | 0.87 |
| 10 (Ref.14) | 0.546 | 4260 | 36490 | 20 | 0 | 4189 | 3145 | 0.75 |
| 11 (Ref.14) | 0.546 | 4260 | 36490 | 20 | 0 | 3488 | 3145 | 0.90 |
| 12 (Ref.14) | 0.39 | 3410 | 41890 | 30 | 0 | 1574 | 1545 | 0.82 |
| 13 (Ref.14) | 0.39 | 3410 | 41890 | 30 | 0 | 1543 | 1545 | 1.00 |
| 14 (Ref.14) | 0.39 | 3410 | 41890 | 40 | 0 | 1830 | 1424 | 0.78 |
| 15 (Ref.14) | 0.39 | 3410 | 41890 | 40 | 0 | 1433 | 1424 | 0.99 |
| 16 (STUDY) | 0.50 | 6400 | 60000 | 0 | 0 | 9419 | 4469 | 0.47 |
| 17 (STUDY) | 0.75 | 6400 | 60000 | 0 | 0 | 13266 | 9337 | 0.70 |
| 18 (STUDY) | 1.00 | 6400 | 60000 | 0 | 0 | 15787 | 16176 | 1.02 |

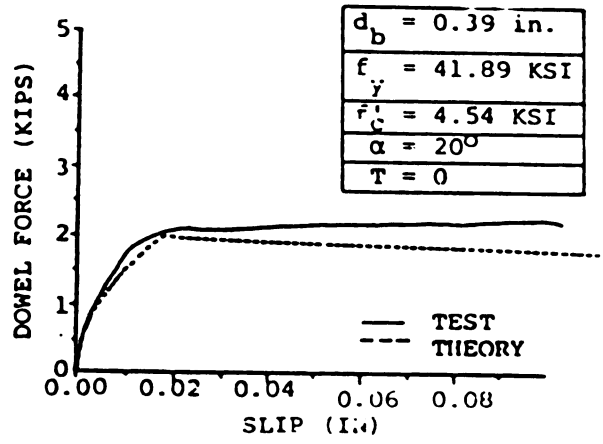


Figure 3.19: Comparison of Theoretical and Experimental Dowel Load-Deflection.

The effects of different factors on dowel strength and dowel load-deflection diagrams were evaluated in this study using Eqns. 3-4 and 3-6. The dowel bar diameter is shown in Figure 3.20(a) to considerably influence the dowel behavior. The yield strength of dowel bar is also shown in Figure 3.20(b) to have some noticable effects. Relatively small influences of the concrete compressive strength and the inclination of dowel bar on dowel load-deflection diagrams can be seen in Figures 3.20(c) and 3.20(d), respectively. Axial load in the dowel bar is shown in Figure 3.20(e) to have important effects on the dowel behavior of the bar especially when its value exceeds about

80% of the bar yield strength.

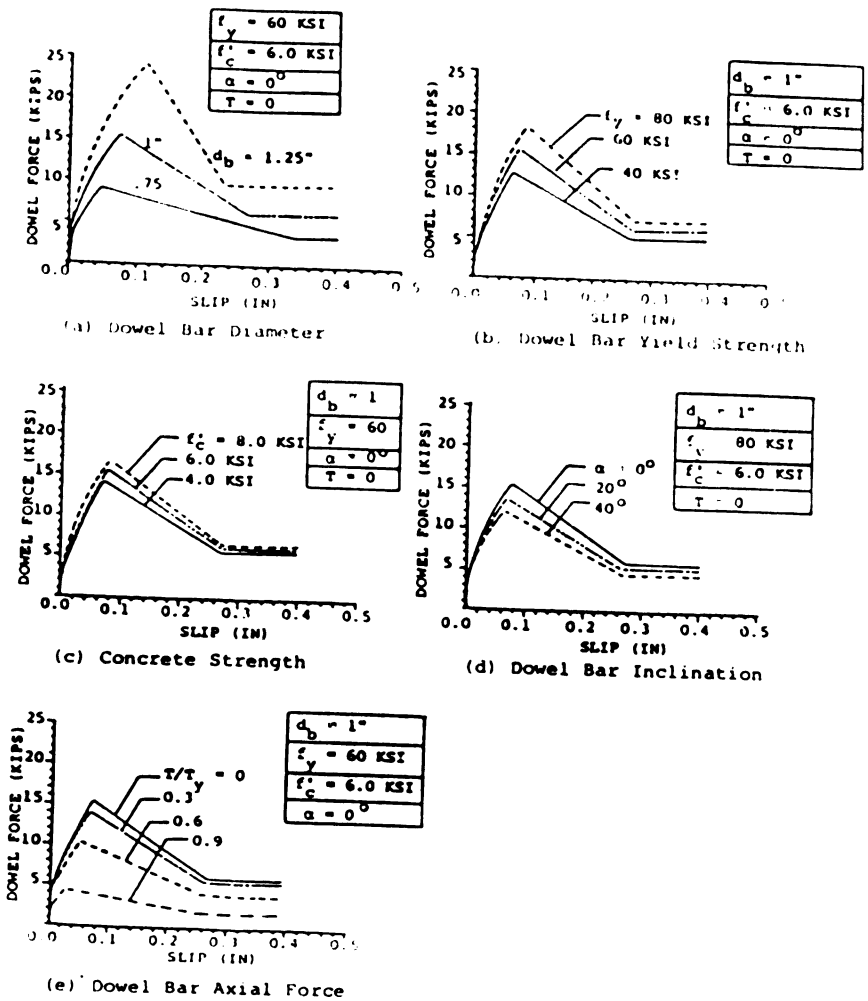


Figure 3.20: Factors Influencing Dowel Bar Behavior.

## 3-4 BEHAVIOR OF DOWEL BARS IN ACTION AGAINST CONCRETE COVER

**3-4.1 Test Program**: The specimens tested in this phase (Figures 3.21 and 3.22) were similar to the ones used for simulating dowel action against core (Figures 3.10 through 3.13) except that the load was reversed, and the dowel bars were supported by #3 stirrups located at 2 in (50.8 mm) from the crack face (shear plane). Applying tension to the specimen as shown in Figure 3.22 results in dowel action of the two bars against concrete cover in one direction and the core in the other. This is similar to dowel action of beam longitudinal bars against beam cover at reinforced concrete joints [Figure 2.1(a)].

Tests were performed on three sizes of grade 60 dowel bars (#4, #6, and #8). Concrete in the specimens was made with type III Portland cement, and the mix proportion and curing condition were similar to the ones in previous specimens (for dowel action against core). The compressive strength of concrete at the test age was 6,200 psi (42.8 MPa). As shown in Figure 3.23, the specimens were fixed through their anchorage bolts to a reaction frame at the top and to a hydraulic actuator at the bottom. The tensile force was measured by a load cell with a maximum error of 0.2%. Opening and slippage of the crack were each measured by two electrical displacement transducers with a maximum error of 0.4%. Loading in all tests was displacement-controlled and quasi-static.

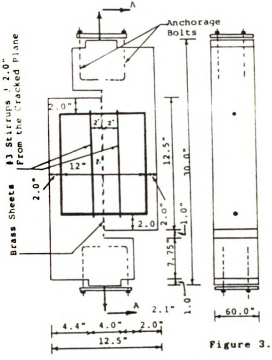


Figure 3.22: Section A-A

Figure 3.21: Test Specimen Under Tension Load.

Figure 3.23: Test Set-Up For Dowel Action Against Cover.

3-4.2 Test Results: Action of dowel bars against concrete cover in all specimens resulted in a split crack separating the concrete cover from the core. After split cracking, stiffness was reduced but resistance of dowel bars continued to increase. Propagation of the split crack was gradual (Figure 3.24) and the concrete cover appeared to be contributing to dowel resistance even after split cracking. The ultimate strength was finally reached when the concrete cover peeled off after which dowel resistance started to drop. Figure 3.25 shows one of the specimens after failure (this is the view after half of the specimen was removed).

Figure 3.26 shows the experimental dowel load-displacement relationships in action against cover. This figure also presents the load-deflection relationships obtained from earlier tests (Figure 3.14) on specimens subjected to compression instead of tension (with dowel bars acting against concrete core). In Figure 3.26, initially the behavior in dowel actions against core and cover were similar, but upon split cracking, stiffness of dowel bars acting against cover dropped suddenly. In these specimens with stirrups located at 2 in (50.8 mm) from the crack face, dowel bars with different sizes all reached a maximum capacity equal to the stirrup yield strength. The deflection at this maximum capacity, however, depended on the bar size, and increased with decreasing diameter of dowel bars.

Figure 3.24: Split Cracking Resulting From Dowel Bars Acting Against Cover.

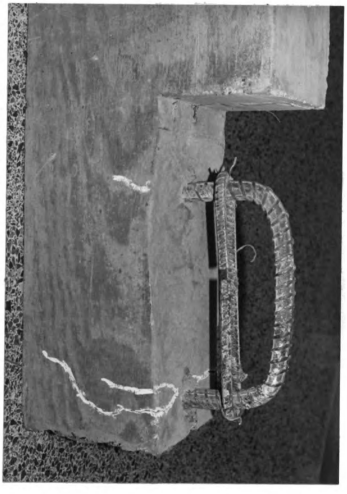

Figure 3.25: View of Half-Section of Specimen Showing Crack Pattern.

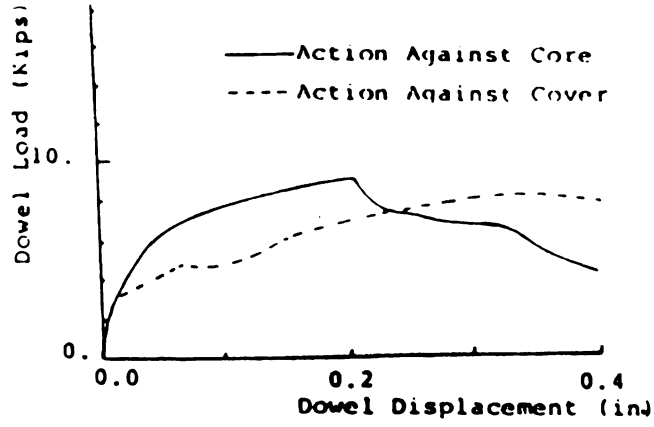


(a) Dowel Bar #4

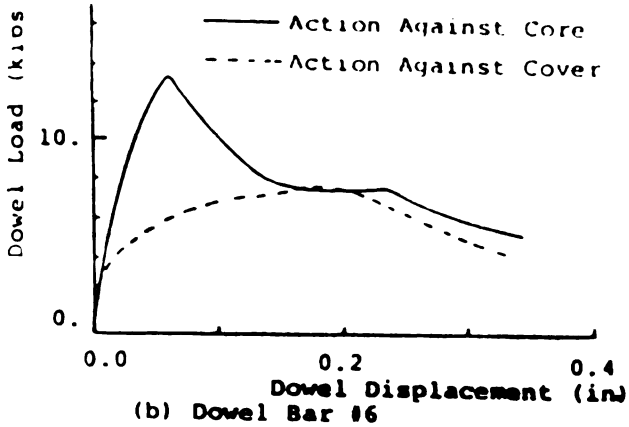


(b) Dowel Bar #6

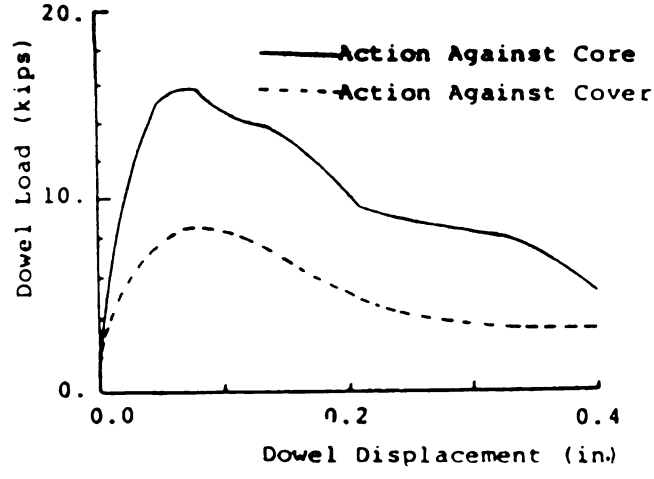


(c) Dowel Bar #8

Figure 3.26: Dowel Load-Deflection Relationships.

Dowel load-crack opening relationships for dowel bars acting against cover and core are shown in Figure 3.27 for different bar sizes. The trend in crack opening is observed in these figures to be similar in both cases.

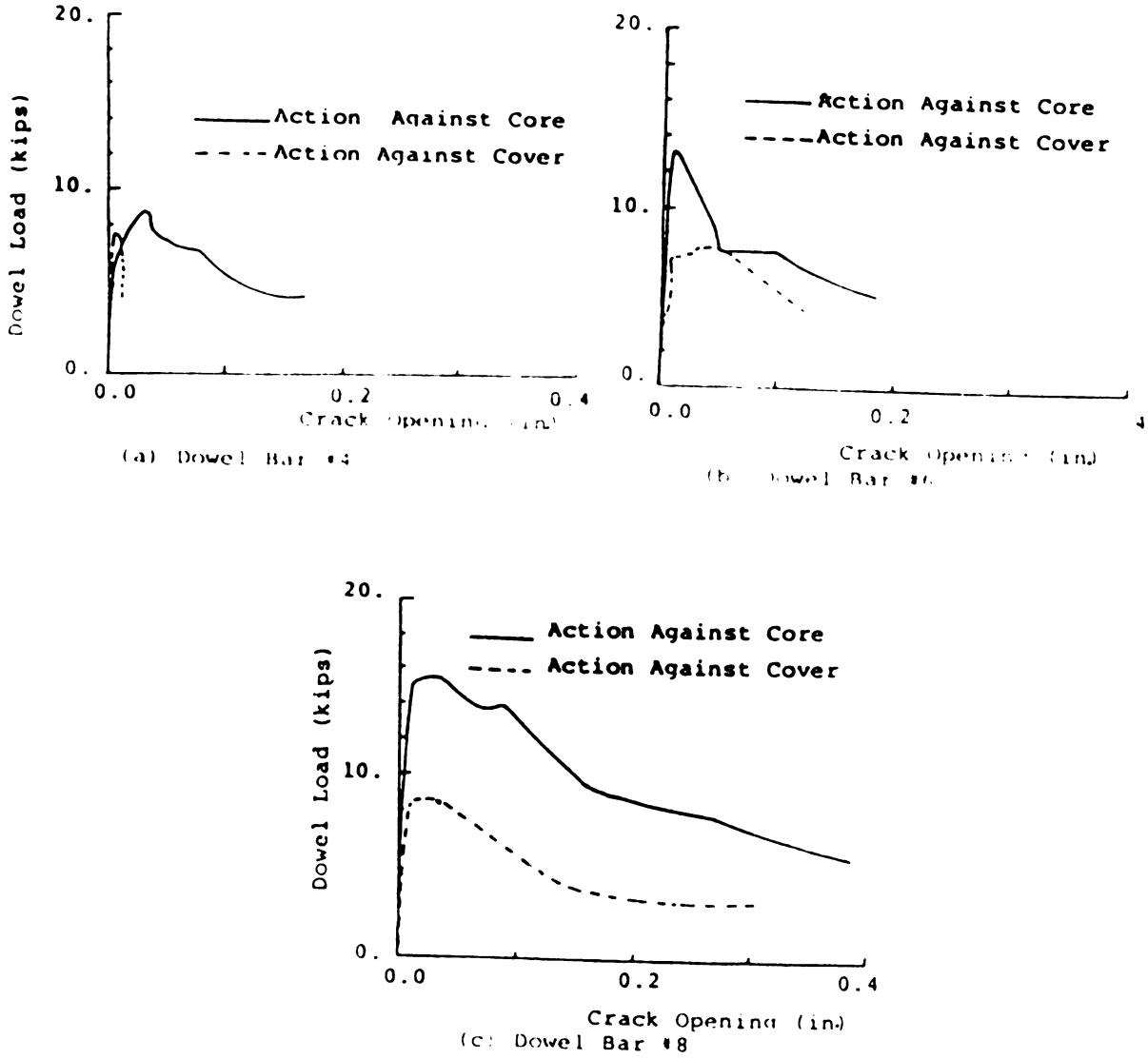


Figure 3.27: Dowel Load-Crack Opening Relationships.

3-4.3 Formulation of Dowel Strength and Load-Deflection Relationship: Before split cracking, the load deflection diagram of dowel bars acting against cover coincides with those ones acting against core. This relationship can be represented by the following expression derived earlier for push against core:

$$D = D_u(s/s_u)^{0.5} \qquad \text{for } s < s_u \tag{3-7}$$

where: $D$ = dowel load;

$s$ = dowel displacement;

$D_u$ = ultimate dowel load in action against core

= $0.07 f_b \gamma^2 d_b^2 + 0.45 f_y d_b^2/\gamma$ (for dowel bars perpendicular to crack with zero axial stress);

$s_u$ = displacement at ultimate dowel load in action against core

= $4.2\times10^{-6} D_u + 0.00945$ (for $s_u$ in inches, $D_u$ in lb)

= $2.43\times10^{-5} D_u + 0.240$ (for $s_u$ in mm, $D_u$ in N);

$k_f$ = concrete foundation modulus [Eqn. (3-2)]

$d_b$ = dowel bar diameter;

$E_s$ = dowel bar modulus of elasticity;

$f_b$ = concrete bearing strength [Eqn. (3-1), with $l_1 = x$ in Eqn. (3-1)]

$f_y$ = dowel bar yield stress.

In order to find the dowel load at the initiation of cover splitting ($D_{cr}$), where the load-deflection diagram

deviates from Eqn. (3-6), the dowel bar in action against cover before split cracking [Figure 3.28(a)] was modeled as a beam on an elastic foundation [Figure 3.28(b)] in which the effect of stirrup was neglected. Figure 3.28(b) also shows the distribution of bearing loads along the length of the dowel bar. Split cracking was assumed to occur when the sum total of bearing loads under the dowel bar from the crack face up to the inflection point [distance (a) in Figure 3.28(b)] reaches the tensile strength provided by the beam width in distance (a). This resulted in the following expression for dowel load at split cracking of cover:

$$D_{cr} = 0.83(b-d_b).a.f_t \qquad (3\text{-}8)$$

where: $b$ = beam width;

$f_t$ = concrete tensile strength

$= 7.5\sqrt{f_c'}$ (psi)

$= 90\sqrt{f_c'}$ (MPa);

$a = \pi/(2\sqrt[4]{k_f d_b/4E_s I_b})$

$E_s$ = steel elastic modulus ( $29\times10^6$ psi or $2\times10^5$MPa)

$I_b$ = dowel bar moment of inertia

$= \pi d_b^4/64.$

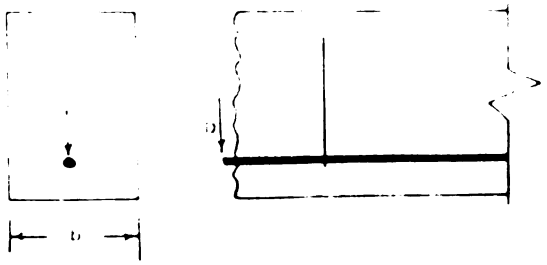


(a) Actual Condition

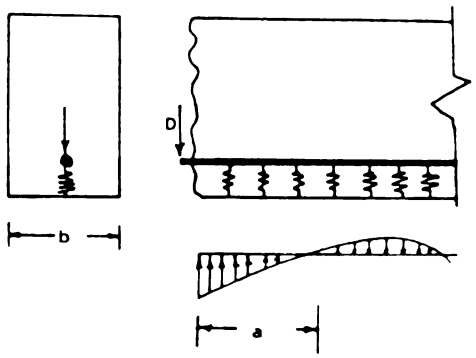


(b) The Proposed Model

**Figure 3.28: Idealization of the Pre-Split Cracking Dowel Bar In Action Against Cover.**

The split cracking load from the above equation compares well with test results:

| BAR SIZE | SPLIT CRACKING LOAD kips (KN) | |
|---|---|---|
| | TEST | THEORY |
| #4 | 3.9 (17.3) | 3.9 (17.3) |
| #6 | 4.6 (20.5) | 5.0 (22.2) |
| #8 | 5.5 (24.5) | 5.9 (26.2) |

After split cracking, concrete cover still contributed to dowel resistance until the ultimate dowel load (that was roughly equal to the stirrup yield force) was reached. This contribution of concrete cover cannot be guranteed in actual conditions where the axial tension in bars tends to

damage the cover.

3-5 BEHAVIOR OF DOWEL BARS UNDER CYCLIC LOADS:

3-5.1 Test Program: Test specimens used for cyclic loading were similar to the ones used for simulating the monotonic action of dowel bars against concrete cover and core. The loading was, however, applied cyclically [Figure 3.29(a)]. The history of deflection application in cyclic tests is shown in Figure 3.29(b). Three cyclic tests on grade 60 dowel bars #4, #6, and #8 were performed. The same concrete mix as in the case of similar tests on dowel action against concrete core and cover was used. The concrete compressive strength was on the average 6,200 psi (42.8 MPa).

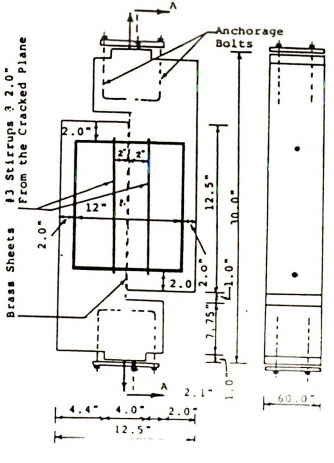


(a) Test Specimen

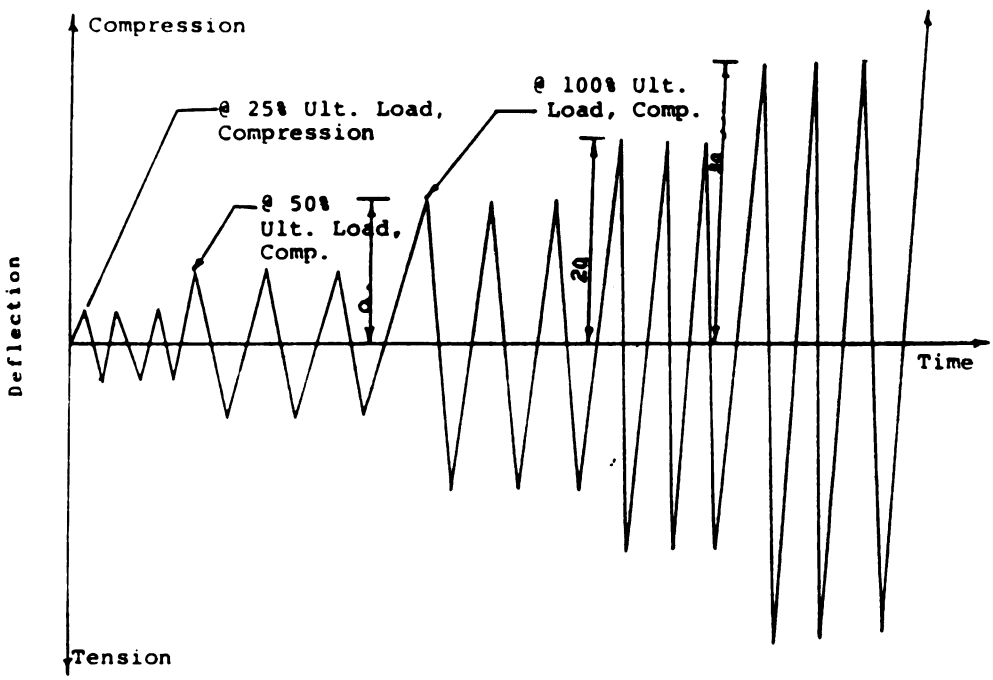


(b) History of Deflection Application

Figure 3.29: Cyclic Tests On Dowel Bars.

3-5.2 Test Results: The first sign of distress in the specimens under cyclic loads was initiation of a split crack between cover and core resulting from dowel action against cover [like the one shown in Figure 3.30(b)]. At large loads, dowel action against core also resulted in a split crack in the plane of dowel bar normal to the direction of the previous crack. Both of these cracks propagated and widened as the loading progressed. In fact,

towards the end of the load history, the cover fully separated from the core. This resulted in deterioration of dowel resistance in action against cover at large-amplitude cycles. Figure 3.30(c) shows the two split cracks in one of the specimen blocks (with the other block removed) after test.

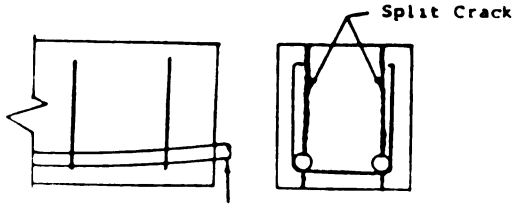


(a) Action Against Core

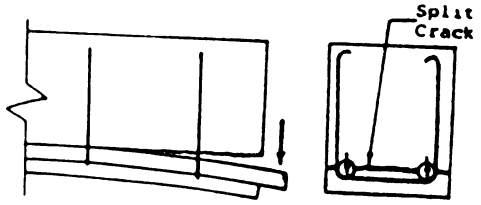


(b) Action Against Cover

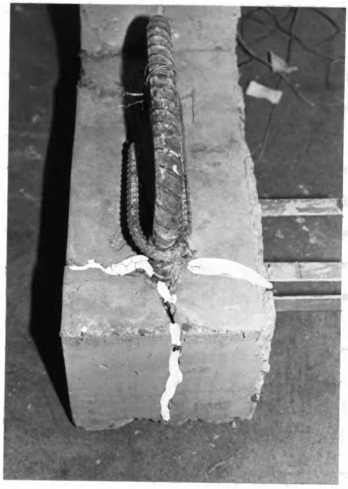

(c) Split Cracks of Specimen Resulting From Cyclic Dowel Action.

Figure 3.30: Split Cracks Resulting From Cyclic Dowel Action.

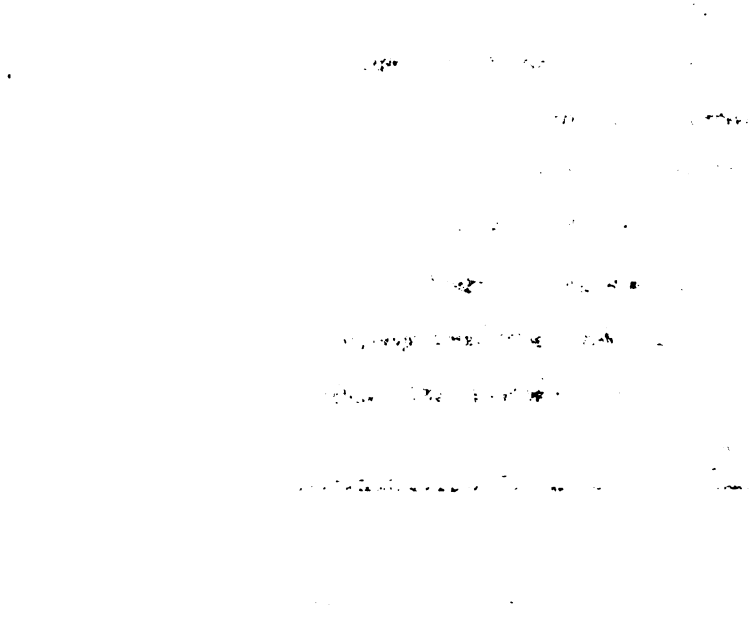

Figures 3.31(a), 3.31(b), and 3.31(c) show the cyclic dowel load-deflection diagrams obtained in tests on bars #4, #6, and #8, respectively. These figures also show the load-deflection diagrams obtained in monotonic tests. Test results presented in Figure 3.31 show that the stiffness and the energy dissipation capacity of dowel bars deteriorate severely with repetition of inelastic load cycles. The hysteretic envelope on the compression side (with push against core) is practically the same as the monotonic load deflection diagram. This means that there is no significant deterioration of strength with repeated cycles on this side. This was also true for dowel bars #6, and #8 on the tension side (with action against cover). Dowel bar #4, however, showed considerable deterioration of strength in push against cover.

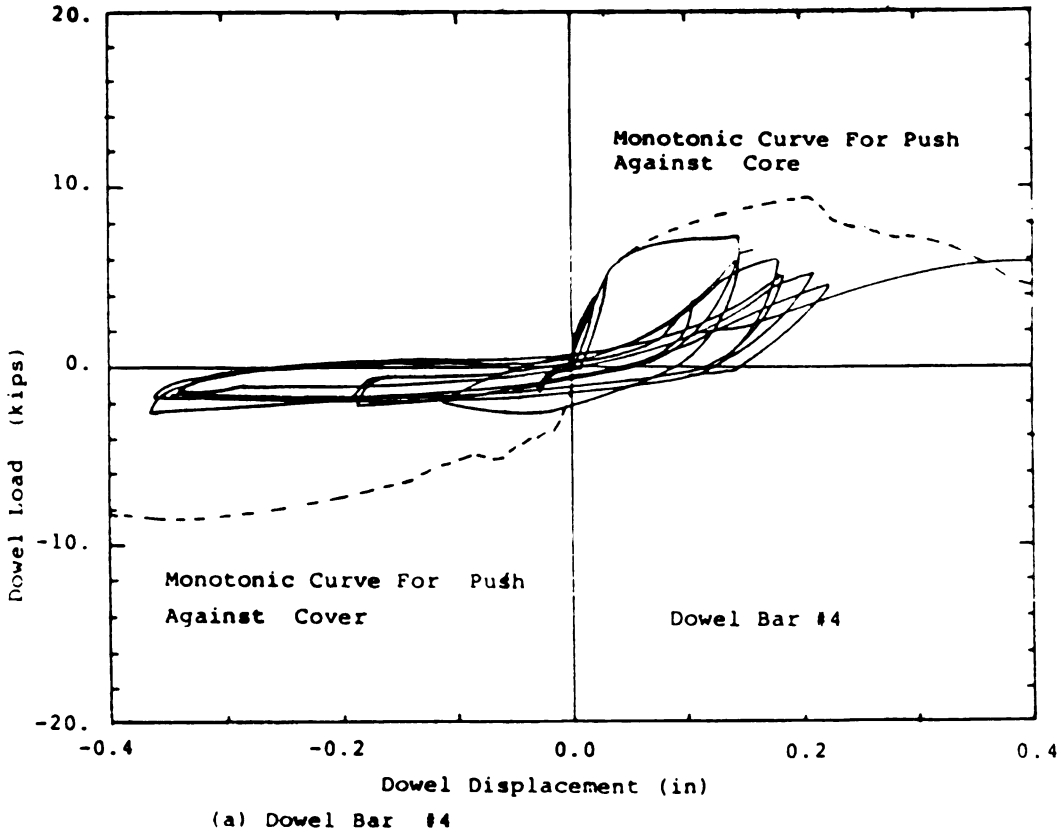


(a) Dowel Bar #4

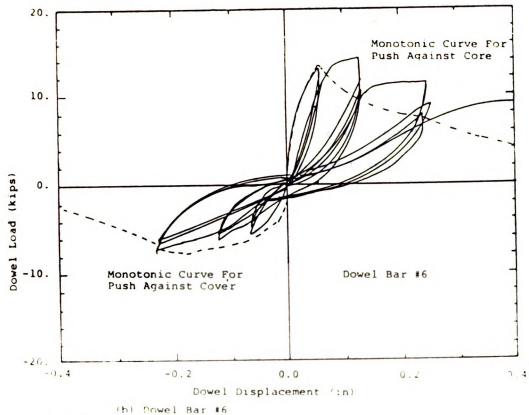


(b) Dowel Bar #6

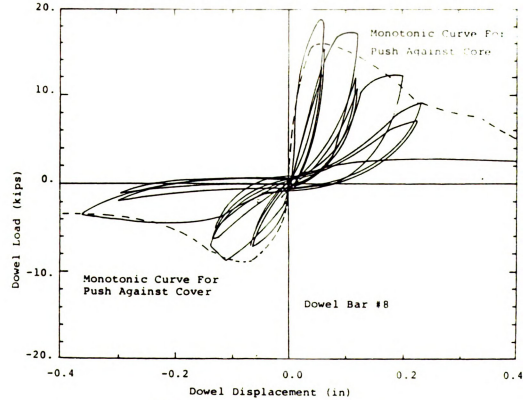


(c) Dowel Bar #8

**Figure 3.31: Experimental Cyclic Dowel Load-Deflection Relationships.**

The diagram shown in Figure 3.32 presents the experimentally obtained dowel load-crack opening relationships. It can be observed that the crack width continues to grow with application of inelastic cyclic loads. This is expected because both actions against core and cover tend to open the crack and there is no tendency towards crack closure. Hence, in the inelastic region, the residual crack width after unloading cannot be overcome with loading in the opposite direction.

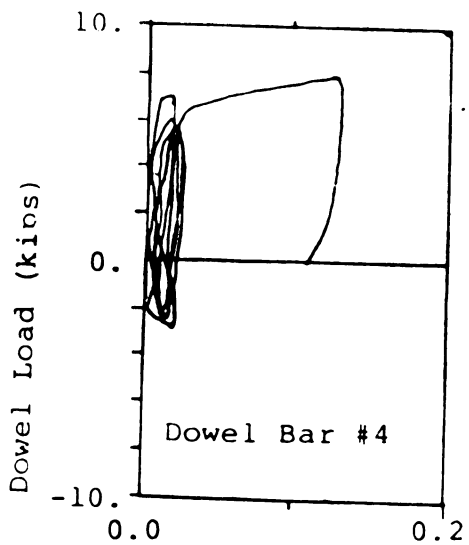


(a) Dowel Bar #4

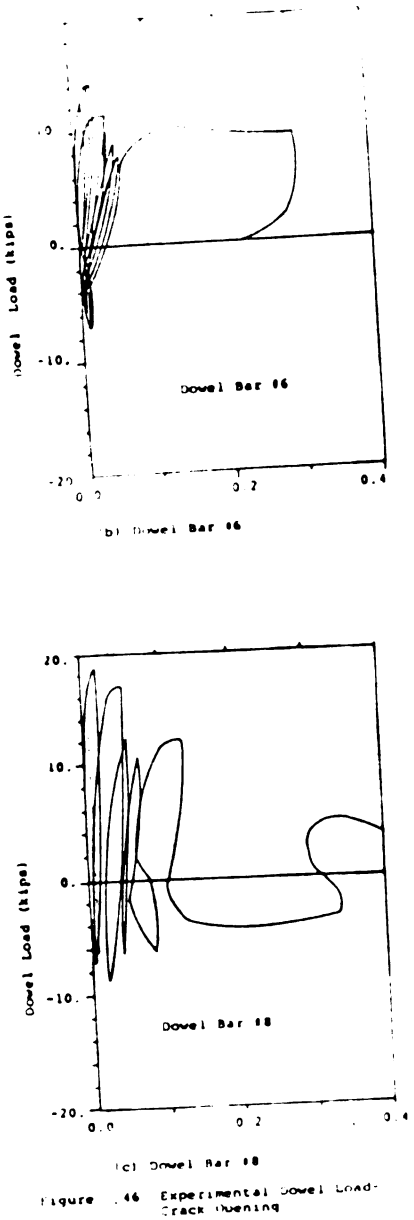


Figure 3.32 Experimental Cyclic Dowel Load-Crack Opening Relationships.

3-5.3 Hysteretic Modeling: A number of monotonic constitutive models have been suggested in the literature for dowel action against core or cover.[4,14,29] Lack of cyclic test data, however, has been an obstacle in developing hysteretic models for dowel bars. In this study, hysteretic rules governing the constitutive behavior of dowel bars under repeated load reversals were derived from test results.

It was assumed that the hysteretic envelopes in push against cover and core follow the respective monotonic load deflection diagrams. This was true for test results on #6, and #8 bars, but not fo #4 bar in action against cover. Dowel bar #4 is not, however, regularly used as beam longitudinal reinforcement.

Figure 3.33 shows the proposed empirical hysteretic rules by adopting the hysteretic envelopes (monotonic dowel load-deflection diagrams) from earlier tests. In a typical cycle for a compressive dowel load ($D^+$) against core and a tensile dowel load ($D^-$) against cover, assuming that $D^+$ is reached first, unloading takes place with a stiffness of 275 kips/in. (4.8 N/mm) up to a dowel load equal to 25% of $D^+$. Then the unloading path go linearly to the origin. The load-deflection diagram in the opposite direction coincides with the last path followed in that direction. This path is the envelope curve in the first loading in any direction. Unloading from $D^-$ results in transfer towards the origin. Loading in the positive direction takes place along the

last path in that direction, but deviates from this path at 75% of $D^+$ in the second cycle and 65% of $D^+$ in the subsequent cycles. This is also true in the tension side with $D^-$ substituting $D^+$. In Figure 3.33, the first cycle is repeated three times and then the deflection is increased to a new maximum value in the compression side. As a result, at point A the stiffness drops to 50% of the initial unloading stiffness (50% of 275 kips/in. in push against core) and then the load-deflection diagram follows path AB until it reaches the envelope curve at point B. Then the envelope is followed until another load reversal takes place at point C with a new value of $D^+$. Unloading at point C also takes place towards the origin. Loading in the tension side then takes place along the last path in this direction up to 65% of D-. Then, here also, stiffness drops to 50% of the initial unloading stiffness (50% of 175 kips/in. in push against cover) and thereafter follow the monotonic curve.

Figures 3.34(a), 3.34(b), and 3.34(c) show the hysteretic diagrams of bars #4, #6, and #8, respectively, as constructed with the above hysteretic rules and the monotonic dowel load-deflection diagrams reported earlier. Comparison of experimental and theoretical hysteretic diagrams in Figures 3.31 and 3.34 show that the proposed model can approximate the test results with a reasonable accuracy. More test data are, however, needed for improving the above empirical hysteretic model.

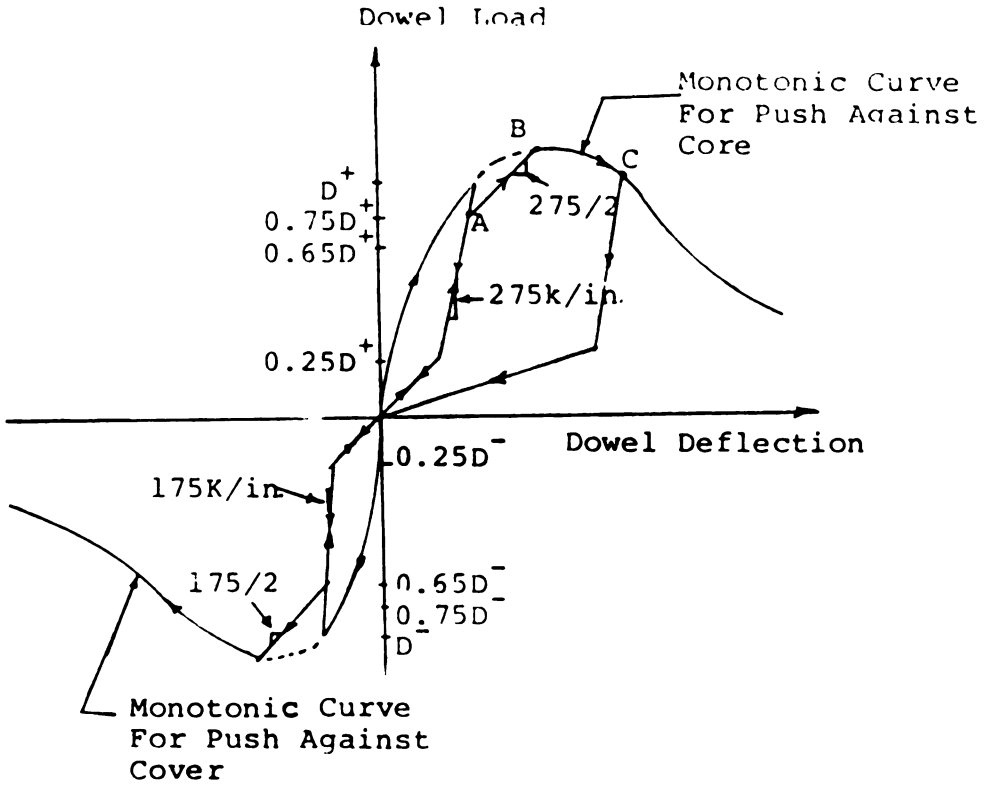


**Figure 3.33: Demonstration of Hysteretic Rules.**

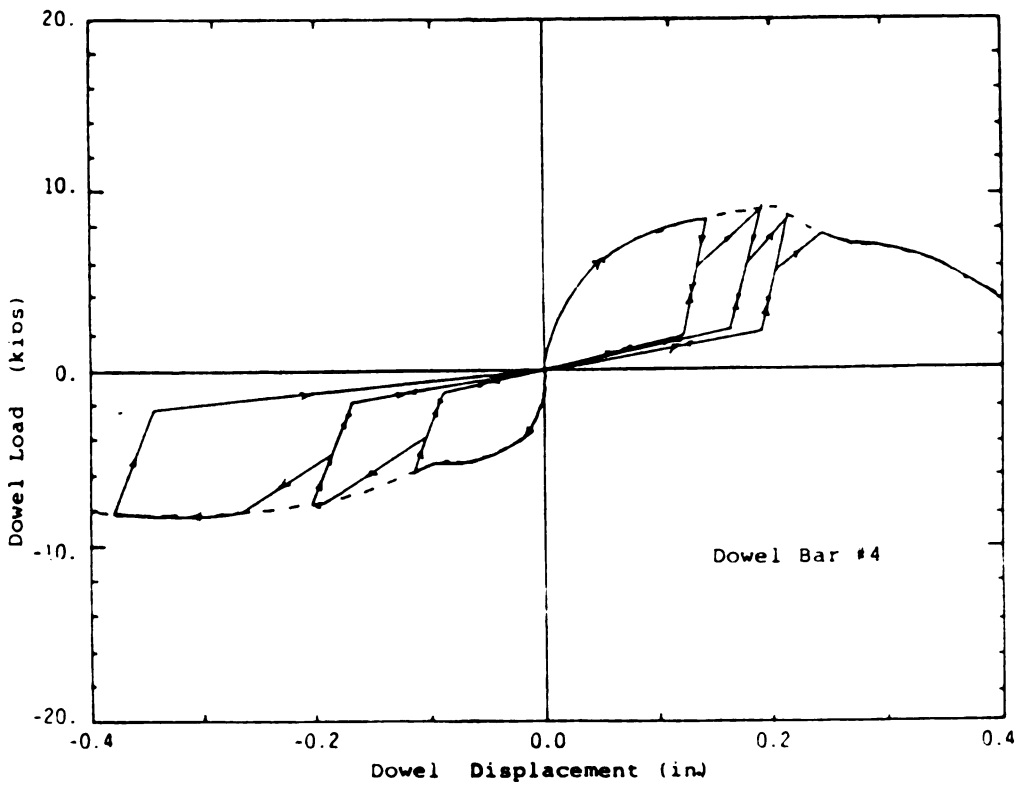


(a) Dowel Bar #4

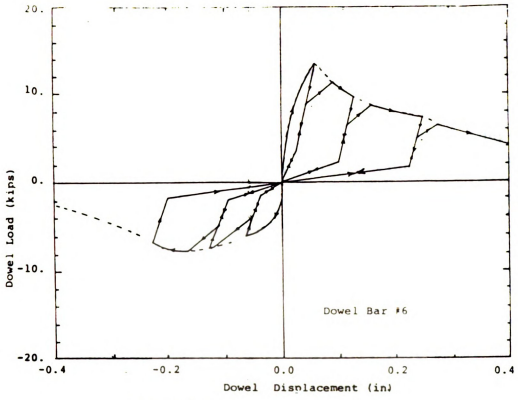


(b) Dowel Bar #6

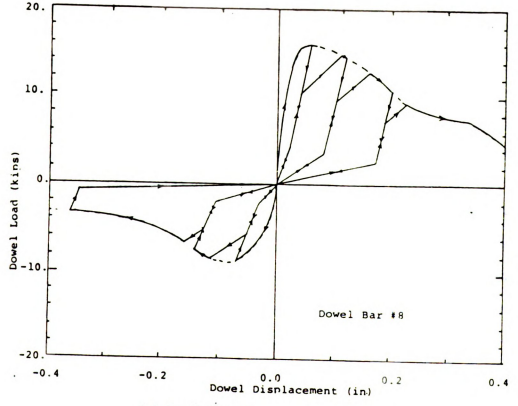


(c) Dowel Bar #8

**Figure 3.34: Hysteretic Diagrams For Dowel Bars.**

# CHAPTER 4

# LITERATURE REVIEW ON PULL-OUT BEHAVIOR OF BEAM LONGITUDINAL BARS BONDED IN BEAM-COLUMN CONNECTIONS

## 4-1 INTRODUCTION

The interaction of deformed bars with concrete depends mainly on the mechanical interlocking between the bar lugs and concrete. Adhesion and friction between the rough bar surface and concrete add only a little to the bond resistance.

Bar slippage is caused mainly by crushing of concrete in front of the lug.[19,23,44,48,53] Under small pull-out forces, the bond resistance is basically made up of adhesion. At higher loads, however, mechanical interlocking between the lugs and concrete is the main source of resistance against pull-out. The high pressure in front of the lugs causes tensile stresses in the concrete which result in internal inclined cracks [Figure 4.1(a) and 4.1(b)], called herein the bond cracks.

Bond cracks modify the response of concrete to loading, and reduce the pull-out stiffness of the anchored bar. After the occurence of bond cracks, the stress transfer from steel to concrete is achieved by inclined compressive forces spreading from the lugs into concrete at an angle as shown in Figure 4.1(c) above. The components of these forces parallel to the bar axis are proportional to the bond stress. The radial components, with respect to the bar axis, load concrete like an internal pressure and induce

tensile hoop stresses which cause splitting cracks. When this crack reaches the concrete surface and none or only a small amount of confining reinforcement is provided, the bond resistance will drop to zero. However, if the concrete is well confined, the load can be increased further.

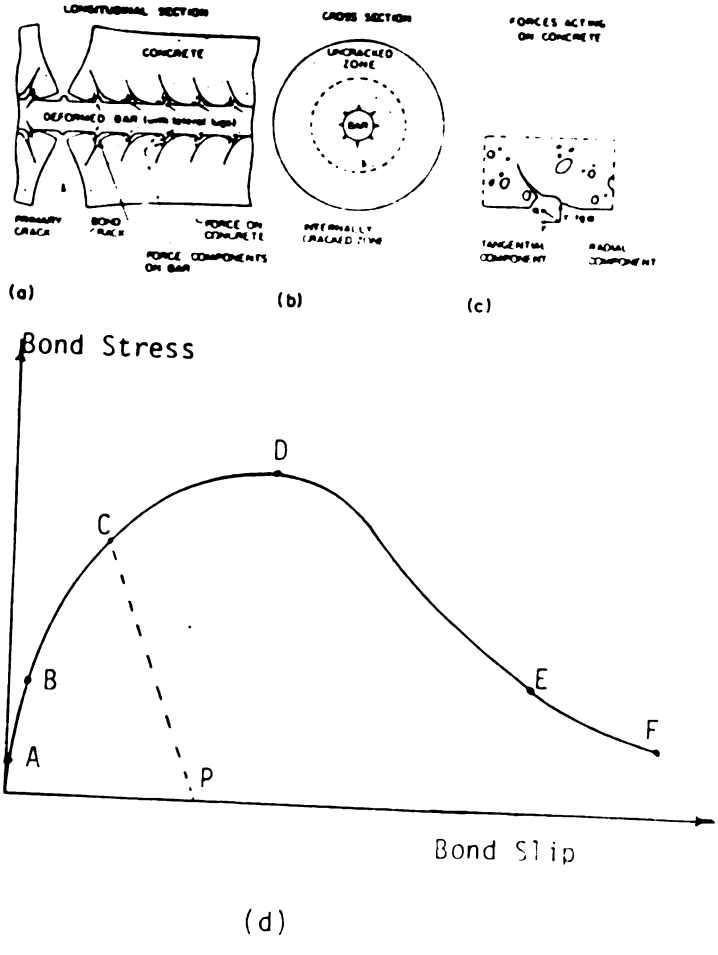


**Figure 4.1: Internal Bond Cracks and Forces Inside Concrete (Ref. 19).**

Figure 4.1(d) shows a typical bond stress-slip relationship. Up to point A in this curve, adhesion is the main source of bond resistance. Bond cracking occurs at

point B, and the splitting cracks (produced by radial stresses) reach the center surface at point C. Curve CP represents the behavior of bond in unconfined concrete, and curve CDEF shows how bond behaves in confined concrete.

When approaching the maximum bond stress in confined concrete [at point D in Figure 4.1(d)] shear cracks in parts of the concrete keys between ribs are initiated as shown below in Figure 4.2.

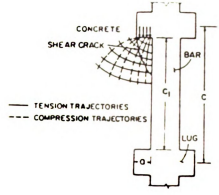


**Figure 4.2: Shear Cracks in the Concrete Keys Between Lugs (Ref. 19).**

When more slippage is induced, an increasing larger part of the concrete is sheared off without much drop in bond resistance. When the slip reaches the clear lug distance, the lug has traveled into the position of the neighboring rib (point E) in Figure 4.1(d), and the concrete between lugs has been sheared off. Thereafter, only frictional resistance is left which is practically independent of the deformation pattern.

Figure 4.3 shows a closer view of the bond cracking process. The inclined bond cracks shown in Figure 4.3(a) do not grow much wider than that developed at maximum bond stress when shear cracks initiate [see Figure 4.3(b)]. In fact, some new inclined cracks might develop as shown by dashed lines in Figure 4.3(c) due to the high compressive forces on concrete in front of the lugs.

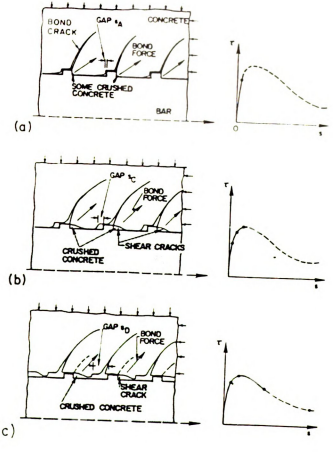


Figure 4.3: Mechanisms of Bond Resistance Monotonic Loading (Ref. 19).

The above illustration of bond failure conditions has not been accepted by some investigators. For example, Tassios[53] assumed that the maximum bond resistance is controlled by compression failure of the compression strut spreading out from the lugs into the concrete.

The adhesive bond resistance is rather small ($\tau_A \approx$ 72 to 145 psi or 1.0 MPa). The bond stress at the occurence of internal bond crack can be roughly estimated to be $\tau_B$ = 208 to 245 psi or 1.43 to 1.70 MPa for a concrete with $f_c'$ = 4,350 psi or 30 MPa[23]. Analysis of these values reveals that even under service loads, adhesion can be overcome and internal bond cracks might occur.

The splitting resistance depends mainly on the concrete failure strength, concrete cover, bar spacing, amount of transverse reinforcement, and transverse pressure. The bond stress $\tau_c$ at splitting may be as low as 290 psi (2.0 MPa) or as high as 1,015 psi (7.0 MPa) for $f_c'$ = 4,350 psi (30 MPa) and with no transverse pressure applied.

The maximum bond resistance, $\tau_{max}$ is mainly influenced by the concrete strength, bar deformations, and the position of the bar during casting. The influence of the bar diameter is relatively small if all dimensions (height and spacing of the bar lugs, and concrete dimensions) are kept constant as multiple of the bar diameter. The bond strength might be influenced by confining reinforcement and transverse pressure. Some investigators have assumed that $\tau_{max}$ is proportional to $f_c'$, but others have taken it

proportional to the $\sqrt{f_c'}$ .

The influence of the bar deformation pattern on the bond behavior has been generally described by the so called relative rib area, $\alpha_{sR}$, that is the relation between bearing area (area of the lug perpendicular to the bar axis) to the shearing area (bar perimeter times lug spacing):

$$\alpha_{sR} = (K.F_R .\mathrm{Sin}\beta / \pi .d_b.C) \qquad (4\text{-}1)$$

where: K =is the # of transverse lug around perimeter;

$F_R$ =is the area of one transverse lug;

$\mathrm{Sin}\beta$ =is the angle between lugs and longitudinal axis of bar.

C =is the center to center distance between tranverse lug.

Bond strength and bond stiffness increase with increasing $\alpha_{sR}$. Common U.S. deformed bars have $\alpha_{sR}$ between 0.05 and 0.08. Depending on the relative rib area, the value of maximum bond stress between 58 to 1,450 psi or 0.4 to 10 MPa for $f_c'$ = 4,350 psi (30 MPa).

There is a large scatter in the experimental bond stress-slip relationships. This large scatter is due to difficulty in measuring slip between steel and concrete correctly and also due to the use of different test specimens with different stress conditions in the concrete surrounding the bar. The position of the bar during casting also influences the local bond laws. The larger bar

stiffness is for the bar cast vertically and loaded against the casting direction of fresh concrete. Bars cast horizontally (especially with a large depth of concrete underneath them) have smaller stiffness and strength. Bars cast vertically but loaded in the casting direction of concrete may perform worse than bars cast horizontally.

The local bond stress-slip relationship is also dependent on the location along the embedment length. In Refs. 19 and 23, three different regions with very different bond stress-slip behavior were identified in a beam-column joint: unconfined concrete in tension, confined concrete and unconfined concrete in compression. These regions are shown in Figure 4.4(a), and typical bond stress-slip relationships in different regions are compared in Figure 4.4(b).

If slip reverses before shear cracking, after unloading [path AF in Figure 4.5(a)], a gap remains open with a width equal to slip at point F. Continuing slip reversal will have a frictional resistance which is rather small because of the smooth surface of concrete surrounding the bar. At point H in Figure 4.5(a), the contact between lugs and concrete reinitiates. With increase in load, the previous cracks close and new inclined cracks perpendicular to the old ones will appear. If the magnitude of bond stress continues to rise, the old and new crack might even join. Confinement makes this part of reversal path close to the monotonic envelop. At point I in Figure 4.5(a), a gap with

a width equal to the difference between slips at points F and I has opened. When again reversing the slip at point I in Figure 4.5(a), the bond mechanism for the loading path IKL is similar to the one for path AFH described earlier. However, the bond resistance starts only to increase again at point L, when the lugs start to press broken pieces of concrete against the previous bearing space. With further movement, cracks close. At point M, lugs and concrete are fully in contact again. With more slip in the same direction, the monotonic envelope is reached again and followed thereafter.

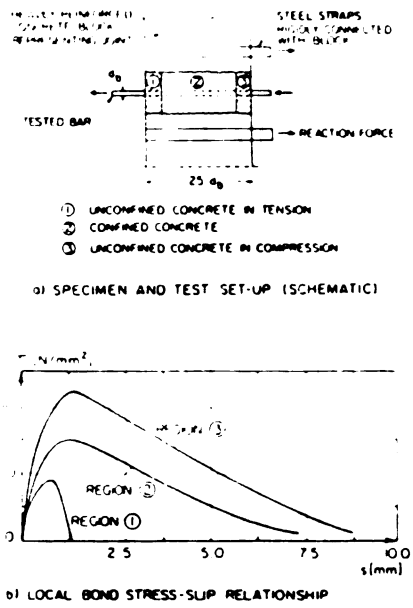


Figure 4.4: Bond Stress-Slip For Monotonic Loading For Different Regions (Ref. 56).

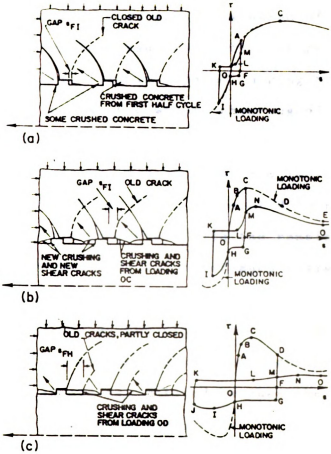


**Figure 4.5: Mechanisms of Bond Resistance Cyclic Loading (Ref. 19).**

Behavior is different if the slip is reversed after the initiation of shear cracks in concrete keys. In this case, the bond resistance in the opposite direction is reduced compared to the monotonic envelope [path CFGHI in Figure 4.5(a)]. This is because after load reversal, the lug presses against a key whose resistance is lower due to the shear crack over part of its length induced by the first half cycle. When reversing the slip again [path IKLMN in

Figure 4.5(b)], only the remaining intact part of the concrete between lugs must be sheared off, resulting in an even lower maximum resistance than at point I.

If a large slip is imposed during the first half cycle resulting in almost complete shearing of concrete keys [Figure 4.5(c)], in reversal the friction is larger than before because the concrete surface is rough along the entire width of the lug. At point H in Figure 4.5(c), the lugs are again in contact with the remaining intact parts of the keys which do not offer much resistance. Therefore, the maximum resistance during the second half cycle is almost the same as the ultimate frictional resistance. During reloading [path JKLMNO in Figure 4.5(c)], an even lower resistance is offered because the concrete at the cylinderical surface where shear failure occured has been smoothen already during the first cycle.

From the above consideration it follows that if the bar is cycled between constant peak slip values, the main damage is done during the first cycle. During successive cycles, the concrete at the cylindrical surface where shear failure occurred is ground off, decreasing its interlocking and frictional resistance. This explains the observed decrease in maximum resistance on the path LMN in Figures 4.5(b) and 4.5(c) with increasing number of cycles.

According to the above theory, under otherwise constant conditions, bars with smaller ratio of clear lug spacing to lug height will produce more bond

deterioration than bars with larger ratio of the lug spacing to the lug height when cycled between the same minimum and maximum slip values.

So far, the local bond behavior was discussed. The anchorage of an embedded bar inside concrete is, however, developed along the length of the bar. As shown in Figure 4.6, the bond stress is almost constant over the core region of the joint leading to an almost linear distribution of steel stresses in this region. The bond stress drops outside the joint core. Details of bond stress distribution depend on the boundary conditions (bar stress and slip) at the two bar ends as well as the history of loading.

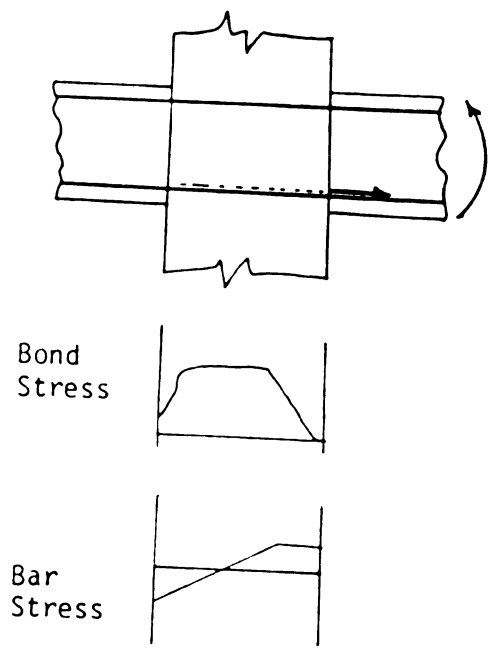


Figure 4.6: Bond Stress Distribution Along Embedded Length of the Bar.

## 4-2 REVIEW OF TEST RESULTS ON BOND

Two comprehensive test programs on the bond behavior inside R/C beam-column connections have been reported in Refs. 12 and 19. The results are discussed in the following.

The subject of study in Ref. 19 has been the local bond stress-slip relationship inside joints under monotonic and repeated loads. The test specimen shown in Figure 4.7 was chosen to represent the conditions found in a beam-column joint.

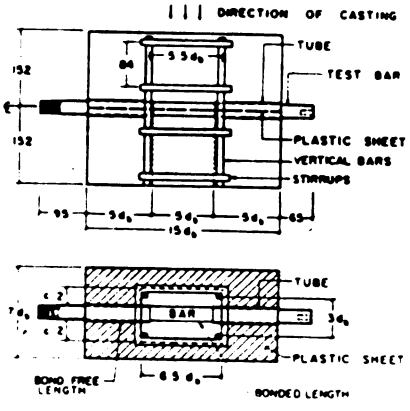


Figure 4.7: Test Specimen Used in Ref. 19.

Only a short length of grade 60 deformed bar was embeded in concrete. During the test, the force acting on the loaded bar end and the slip, at the unloaded bar end were measured. Assuming that bond stresses are evenly

distributed along the bonded length, the value of bond stress can be easily calculated from the measured force. Furthermore, because the steel behaves elastically and the embedment length is short, the slip values at the unloaded and loaded bar ends do not differ significantly. Therefore, the measured slip represents the local slip in the middle of embedment length with sufficient accuracy. Note that strictly speaking the resulting relationship is not a local bond-slip relationship but an average one. The embedded length $5d_b$ shown in Figure 4.7 is short enough to reduce the scatter of test results usually observed in tests with very short bonded lengths.

The bars in the specimen shown in Figure 4.7 were placed in the middle of the specimen and cast in a horizontal position. Therefore, the bond could be expected to be some what superior or inferior to top or bottom bar, respectively.

Ref. 19 has reported the results of 125 tests on specimens similar to the ones shown in Figure 4.7. The "standard" test in this program consisted of a #8 bar embedded in concrete with a compressive strength of 4,350 psi (30 MPa), and confined with #4 bars. No transverse pressure was applied in the "standard" test in which the loading was applied with a slip rate of 0.067 in./min (1.702 mm/min). In the other tests of Ref. 19, one parameter of the standard specimen was varied at each time as follows: concrete stregth ( increased to 7,975 psi or 55 MPa);

transverse pressure (ranging from 725 to 1,914 psi or 5.0 to 13.2 MPa in the direction of the column reinforcement); bar diameter (#6 or #10); confining reinforcement (#8 or #2 or none); bar spacing (increased from $ld_b$ in the standard specimen to $6d_b$); and loading rate [0.67 in./min (1.702 mm/min) and 6.7 in/min (170.0 mm/min) slip rate].

The influences of the above parameters were studied for monotonically increasing slip and for cyclic loading at a peak slip value of 0.065 in. (1.651 mm). In cyclic tests, after performing 10 cycles between fixed slip values, the slip was increased monotonically to failure.

In all tests, except those with an applied transverse pressure, a splitting crack developed prior to failure in the plane of the longitudinal axis of the bar. The bond stress at splitting was about 580 to 1,305 psi or 4 to 9 MPa for concrete with compressive strength of 4,350 psi (30 MPa). After developing this crack, the load dropped rapidly if concrete was not confined. In the case of confined concrete, however, the load could be increased further with a gradually decreasing bond stiffness. This can be explained by the fact that the growth of cracks can be controlled by vertical bars crossing the crack plane.

In all tests conducted on specimens with confined concrete, failure was caused by pulling out of the bars at steel stresses well below yield strength ( between 40% to 80% of yield strength). The concrete between lugs was completely sheared off and almost pulverized. Specimens

with no confining reinforcement failed by splitting of concrete in the plane of the bar longitudinal axis at about 45% of the pull-out load of comparable confined specimens. In these specimens, the concrete between lugs was intact after failure and no severe damage (shear cracks or crushing) could be detected.

Under monotonic loading as shown in Figure 4.8, the stiffness of the ascending branch of the bond stress-slip curve decreased gradually from its initial large value to zero when approaching the maximum bond resistance at a slip value approximately 0.06 in. (1.52 mm). After passing the maximum bond stress, the bond resistance decreased slowly and almost linearly until it leveled off at a slip of about 0.45 in. (11.43). This value is almost identical to the clear distance between lugs. For larger slip values, the bond resistance was almost constant. The scatter of test results was relatively small ( coefficient of variation of bond resistance was about 5%) especially when the specimens were cast from the same concrete batch.

Bond stress-slip relationships for tension and compression were almost identical. However, it can be expected that after yielding (that did not occur in these tests), the diameter of the bar in tension will be significantly reduced due to the necking effect, and this can reduce the bond resistance. The opposite can be true for bars yielding in compression. The necking effect can be expected to change the bond resistance by not more than 20

to 30%.

The absence of confining reinforcement drastically influenced the bond behavior in test reported in Ref. 19 (Figure 4.9). Specimens having no confined reinforcement failed by splitting of concrete at a rather small bond stress (870 psi or 6 MPa). This value compared favorably with:

$$\tau_{crack} = 1.5\, f_{ct} \sqrt{C/d_b} \qquad (4\text{-}2)$$

where: $\tau_{crack}$ = bond stress at occurence of splitting cracks

$C$ = minimum concrete cover

$f_{ct}$ = axial tensile strength of concrete

$d_b$ = diameter of bar.

After splitting, the bond resistance dropped rapidly in unconfined specimens and reached 145 psi (1 MPa) at a slip of 0.16 in. (4.06 mm). This resistance is expected to be provided by the friction at the bearing plate used in the test.

Specimens with confined concrete failed by bar pull out because the split cracks developed in the plane of the longitudinal axis of the bars were restrained by vertical bars (the influence of stirrups was negligible). There was no significant difference between the behavior of confined specimens with different confinements tested in Ref. 19. This shows that there exists an upper limit for the amount

of restraining reinforcement beyond which behavior cannot be improved further.

The maximum bond resistance decreased slightly with increasing bar diameter in monotonic tests (Figure 4.10). The relationship was 1.00 : 0.94 : 0.85 for #6, #8, and #10 bars, respectively. The descending branch of the local bond stress-slip relationships leveled up at slip values that were almost identical with the clear distance between lugs [about 0.36 in. (9.14 mm) for #6 and #10 bars and 0.45 in. (11.43 mm) for #8 bar]. The frictional bond resistance was not influenced much by variations in bar diameter, lug spacing, or the related rib area. It was also observed that increased related rib areas increase the ascending branch stiffness as well as the peak bond resistance.

As can be seen in Figure 4.11, stiffness of the ascending branch as well as bond resistance at equal slip values increase with increasing compressive strength of concrete. Furthermore, maximum bond resistance is reached at smaller slip values in specimens with higher-strength concrete. The increase in bond resistance was proportional to the increase in tensile strength (which is proportional to the $\sqrt{f_c'}$ ).

The bond behavior in tests performed in Ref. 19 improved with increasing bar spacing; however, as shown in Figure 4.12, the influence was relatively small. The small effect of bar spacing is possibly because the split cracks (that are strongly influenced by bar spacing) are

restrained by the confining reinforcement and hence failure is by pull-out and not split cracking.

Increase in transverse pressure is shown in Figure 4.13 to cause increases in the maximum bond resistance and the ultimate frictional resistance.[19] The slip at maximum bond resistance also shifted to slightly larger values with increasing transverse pressure.

The influence of rate of pull-out (or rate of slip) on the local bond constitutive behavior can be seen from Figure 4.14. While the overall shape of bond stress-slip relationship was not changed much, bond resistance increased with increasing rate of pull-out. A change of rate of pull-out by a factor of 100 resulted in a change of maximum bond resistance by about 15%.

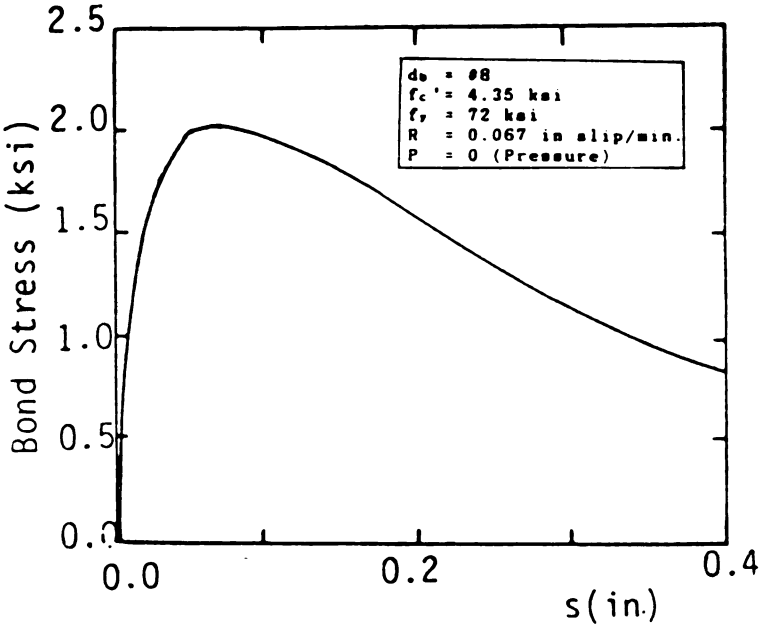


Figure 4.8: Bond Stress-Slip Relationship For All Monotonic Tests (Ref. 19).

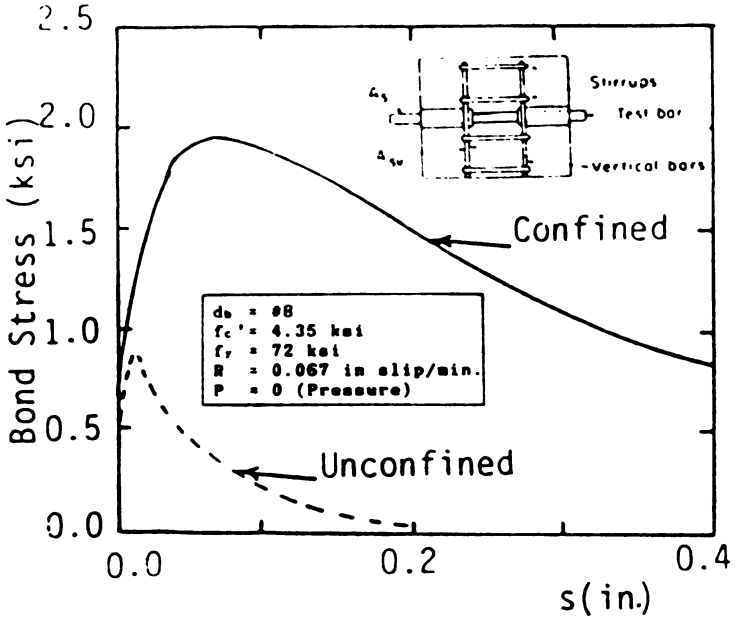


Figure 4.9 Comparison of Bond Behavior In Confined and Unconfined Concrete (Ref. 19).

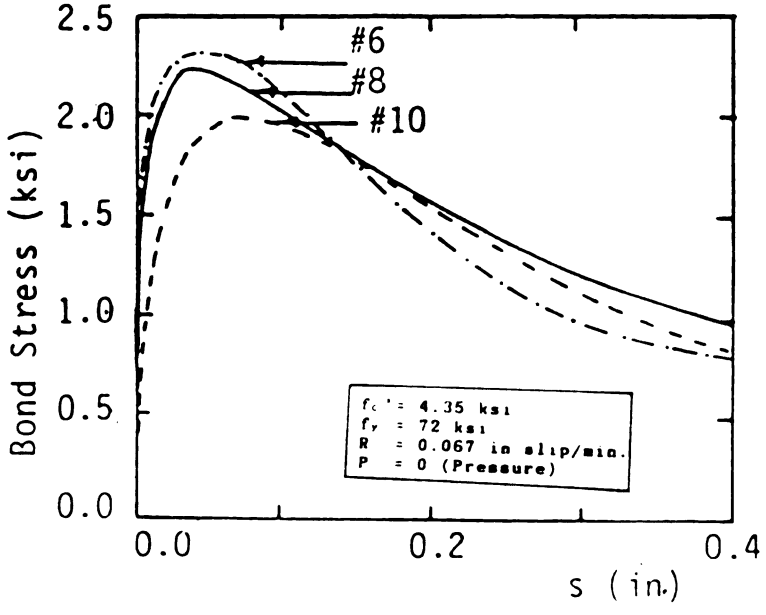


Figure 4.10 Effect of Bar Diameter (Ref. 19).

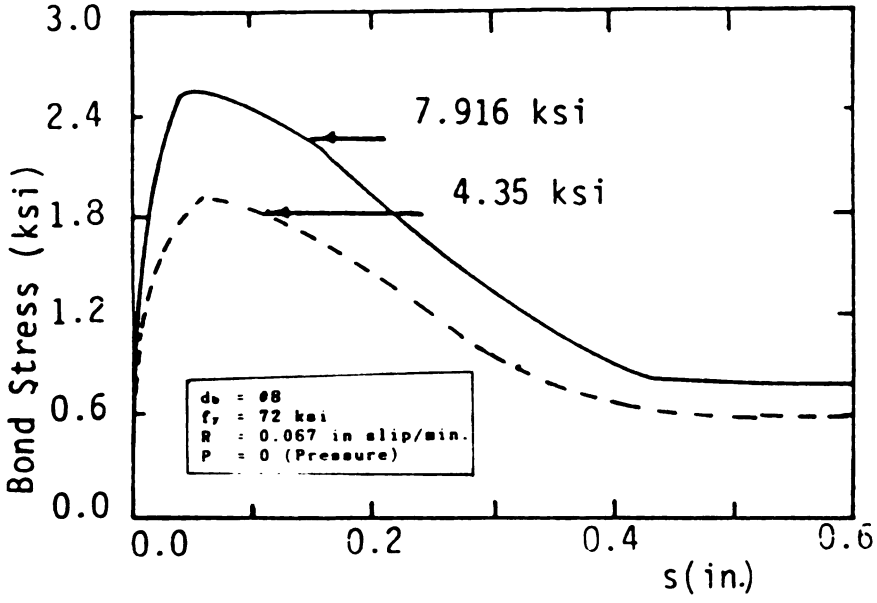


Figure 4.11: Effect of Concrete Strength (Ref. 19).

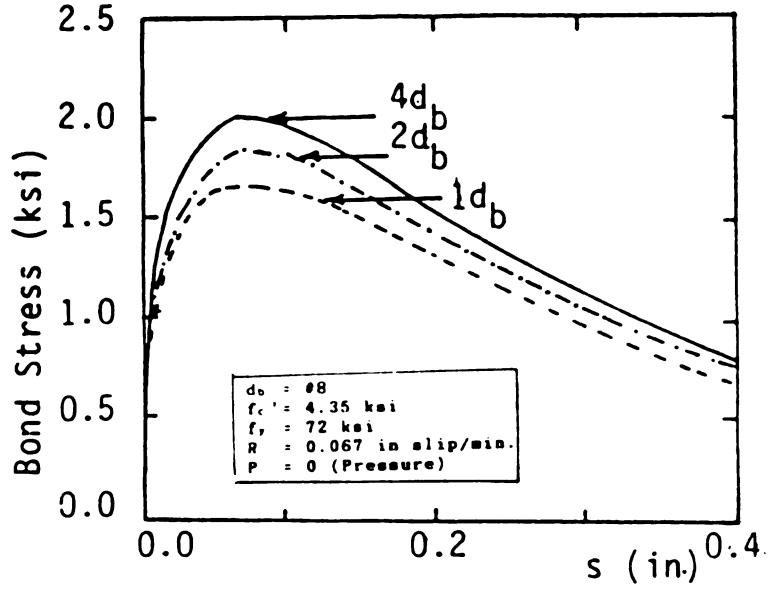


Figure 4.12: Effect of Clear Bar Spacing (Ref. 19).

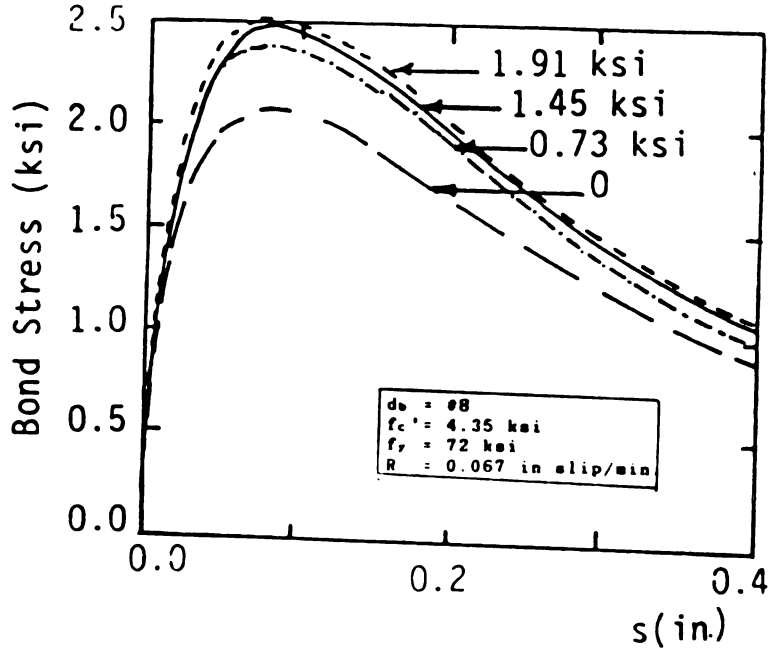


**Figure 4.13: Effect of Transverse Pressure (Ref. 19).**

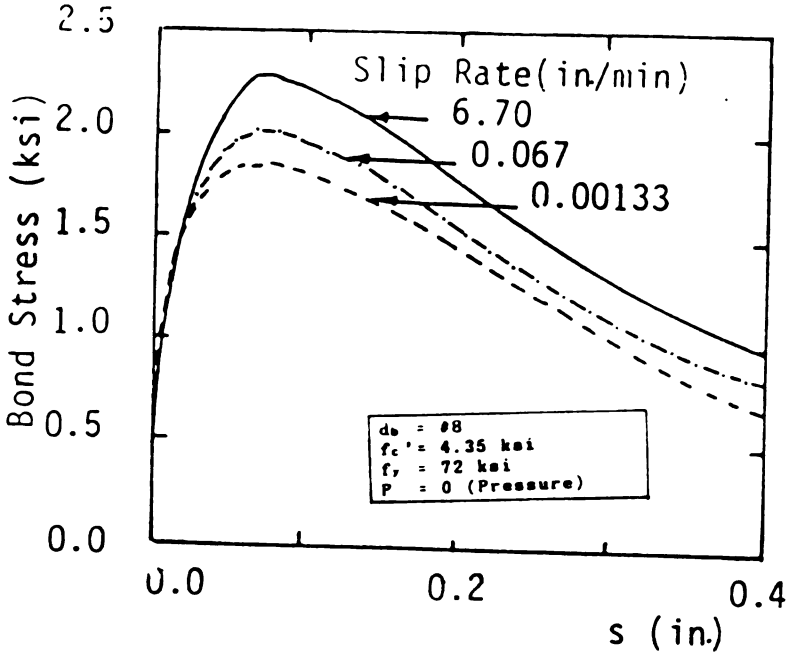


**Figure 4.14: Effect of the Rate of Slip (Ref. 19).**

Some of the hysteretic loops obtained in a cyclic test on the standard specimen together with the monotonic stress-slip relationships are shown in Figure 4.15. In cyclic tests, the scatter of test results was still tolorable especially if the tested specimens were from the same concrete batch. The coefficient of variation of a characteristic bond stress value was between 6 and 10%.

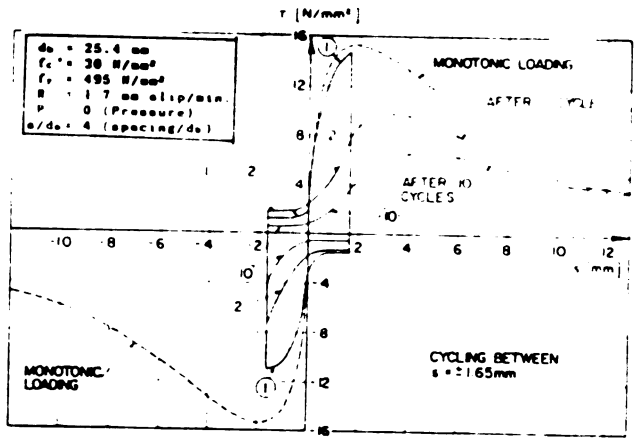


Figure 4.15: Bond Stress-Slip Relationship For Cyclic Loading (Ref. 19).

In cyclic loading, if the peak bond stress during cycling did not exceed 70 to 80% of the monotonic bond strength, the deterioration was moderate (Figure 4.16). No major deterioration was also observed under repeated slip from zero load to a peak slip value, no matter what the peak slip value (Figure 4.17).

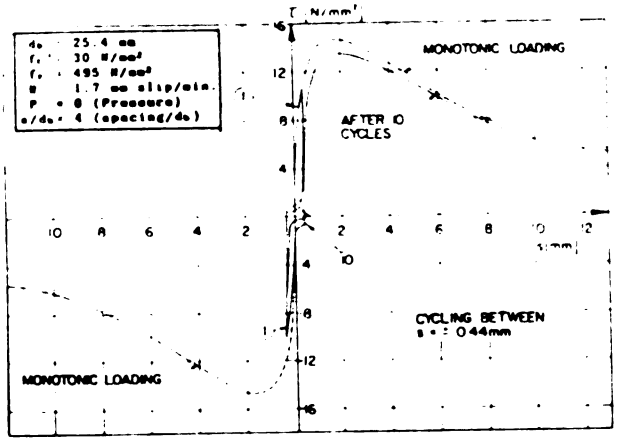


Figure 4.16: Bond Stress-Slip Relationship For Cyclic Loading (Ref. 19).

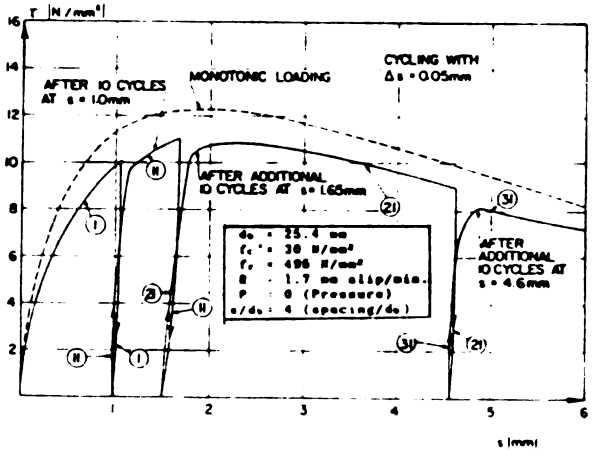


Figure 4.17: Bond Stress-Slip Relationship For Cyclic Loading (Ref. 19).

Loading to a slip value inducing a bond stress larger than 80% of the monotonic bond strength in either direction led to a degradation in the bond stress-slip behavior in the reverse direction (Figure 4.18). As shown in this figure, the bond stress-slip relationship at slip values larger than the peak value during the previous cycle was significantly different from the virgin monotonic envelope. There always was a significant deterioration of the bond resistance which increased with increasing peak slip and increasing number of cycles, and was larger for full reversal of slip than for half cycles. Furthermore, the cycle produced a pronounced deterioration of the bond stiffness and bond resistance at slip values smaller than or equal to the peak slip value.

The frictional bond resistance during cycling was dependent upon the value of the peak slip and the number of cycles. With repeated cycles, the frictional bond resistance deteriorated rapidly [see Figure 4.18].

Cyclic loading with increasing slip values had an added effect on the deterioration of bond stiffness and bond resistance. On the other hand, some additional cycles between smaller slip values than the peak value in the previous cycles did not significantly influence the bond behavior at larger peak value.

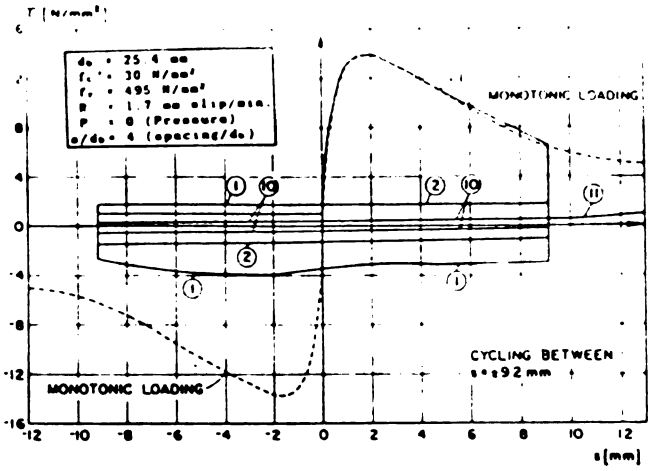


Figure 4.18: Bond Stress-Slip Relationship For Cyclic Loading (Ref. 19).

The cyclic bond deteriorations were approximatly the same when the test bars were first loaded in tension or compression. Substituting #2 bars for #4 bars as transverse (restraining) reinforcement had no significant effect on the cyclic bond deteriorations. This is also true for specimens made out of high strength concrete or with different clear spacings.

Transverse pressure in the investigated range as well as a 100 times faster loading rate did not change the cyclic deteriorations very much. Bars with different related rib areas also had similar deteriorations under cyclic loads in the limited number of tests reported in Ref. 19. The bond resistance was almost independent of the bar size after some load cycles.

In short, it can be stated that the behavior of bond during cyclic loading is not significantly affected by the various parameters investigated if the deterioration of bond resistance is related to the pertinent monotonic

envelope. However, the influence of bar diameter and deformation pattern on the cyclic load behavior were not studied thoroughly in Ref. 19.

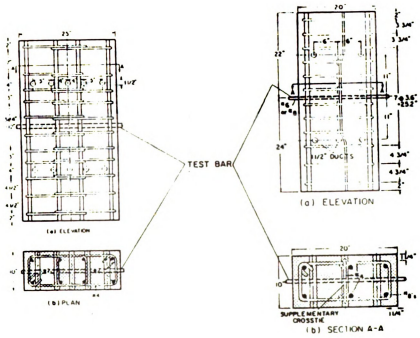


Figure 4.19: Specimen Detail Plan Used In Ref. 12.

Another series of tests have been reported in Ref. 12 on specimens refered to as "column stubs" shown in Figure 4.19. These specimens represent a section of an interior column through which a single bar of a continous beam passes Figure 4.20. The column stub is reinforced to simulate the confinement within a joint core when designed and detailed according to ACI standard 318-71. Of the seven specimens tested in Ref. 12, five were 25 x 10 in. (625 x 250 mm) and two were 20 x 10 in. (500 x 250 mm) in column

cross-section Figure 4.19. The width of 25 and 20 in. (625 and 500 mm) in tested specimens specified the embedment lengths of bars. The overall height of the specimen was 46 in. (1,150 mm), and reinforcing bars were all grade 60. deformed bars. The longitudinal reinforcement for the 25 in. (625 mm) column stub consisted of eight #7 bars and the ties were #4 reinforcing bars; the 20 in. (500 mm) column stub consisted of four #8 and 2#4 reinforcing bars, with #4 ties. The embedded bar is placed so that it is in the middle of the 10 in. (250 mm) thickness, and approximately in the center of the column stub height. The concrete type in the specimens included 4 ksi normal weight, 4 ksi light weight and 9 ksi normal weight.

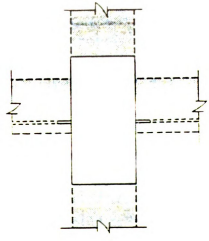

Figure 4.20: Column Stub Specimen (Ref. 12).

The test set-up shown in Figure 4.21 below was designed to avoid support reaction from affecting the behavior of the bar being tested. For tests in which both ends of the rebar were loaded, the two end loads were equal but opposite, representing the condition that occurs in a joint after the beam had cracked and the top and bottom beam bars act alone to resist equal couples at the column faces. Some of the tests were also performed with loading at only one end of the bar. The instrumentation monitored behavior of the embedded bar from which the applied loads, displacement of the bar at either end and the load behavior along the embedded length of the bar could be deduced ( the deduction of bond stress-slip relationship required the assumption of Ramberg-Osgood hysteretic model for steel bar).

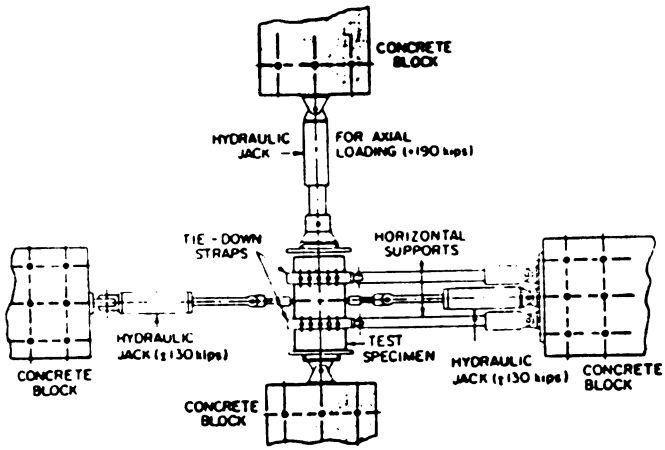


Figure 4.21: Test Set-Up Used In Ref. 12.

Test results in Ref. 12 were presented in the form of the local bond stress-slip relationships. The local bond-slip for different locations along the 25 in. (625 mm) embeddment length in the standard specimen (that was constructed of normal weight concrete and was loaded at both ends) are shown Figures 4.22 and 4.23 for the monotonic loading.

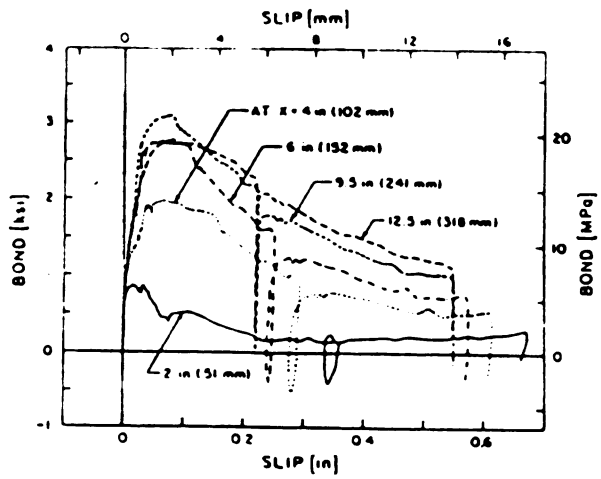


Figure 4.22: Bond-Slip For Monotonic Standard Specimen (Tensile Bar Strain on Pull Side of Specimen). In All Cases x is Measured From Left End of Bar Embedment (Ref. 12).

Figure 4.22 shows the monotonic loading for portions of the bar that are in tension, and Figure 4.23 shows the curves for the portion of bar in compression. Comparison of these figures shows that the compression side exhibits a stiffer response as well as a higher maximum bond resistance.

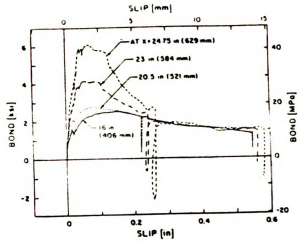


**Figure 4.23: Bond-Slip For Monotonic Standard Specimen (Compressive Bar Strain on Push Side of Specimen) (Ref. 12).**

A typical comparison of cyclic bond-slip curves with monotonic curve at the same relative location in Figure 4.24 reveals how closely the cyclic curve follows the monotonic curve until bond degradation due to cyclic loading causes the curve to fall below the monotonic bond value.

In the case of specimens with light-weight aggregate concrete, the variation of local bond-slip at different locations along the embedded length was less than that with normal weight concrete. For the length of the bar under tension, the response at 6 in. (150 mm) of embedment shows a maximum bond stress 40% less than that of a normal-weight concrete (Figure 4.25). The increase in maximum bond stress in the compression region of the bar is much less for the

light weight concrete. Moreover, the degradation in the compressive region is more severe than with normal weight concrete.

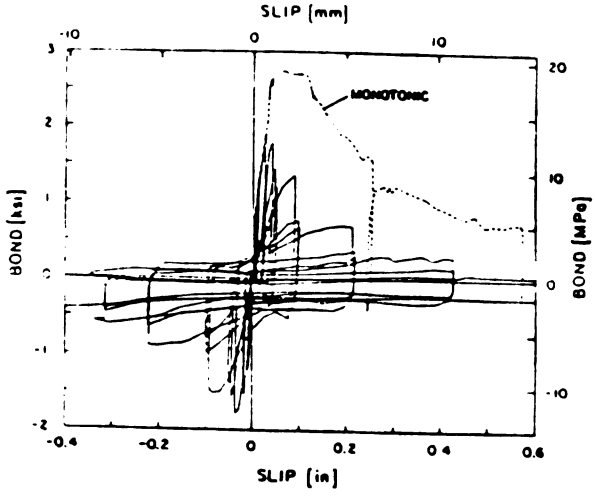


Figure 4.24: Cyclic vs Monotonic Bond-Slip For Standard Specimen At x = 6.0 in. of Embedment (Ref. 12).

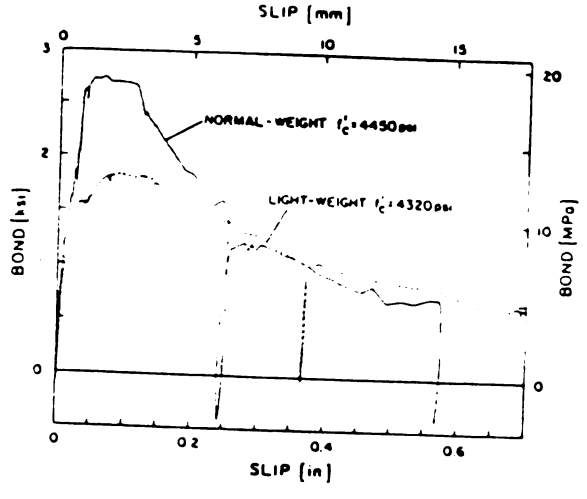


Figure 4.25: Comparison of Standard and Lightweight Specimen Monotonic Bond-Slip at x = 6.0 in. of Embedment (Ref. 12).

Stiffness of the local bond-slip curve in higher strength concrete specimens, that were constructed with a shorter embeddment length of 20 in. (500 mm) in anticipation of higher bond strength, was much greater than a comparable local response for the standard concrete. The increase in maximum bond strength over the standard normal weight concrete was about 60%. This was less than the relative difference in compressive strength (9 ksi or 62 MPa versus 4.5 ksi or 31 MPa), indicating the greater influence of tensile and shear stresses on bond than of compressive stress. The variation over the embedment length of local bond-slip for the high strength concrete specimen was similar to that of the standard specimens. The degradation under cyclic loads in the high strength concrete specimen was more than the standard specimen.

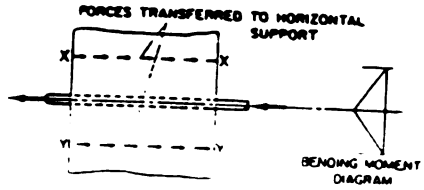


Figure 4.26: Bending Moment Produced Applied Loading (Ref. 12).

Causes of the variation in local bond-slip relationship for different locations along the embedment length have also been discussed in Ref. 2. The first cause according to this reference is due to the bending moment generated by applied loads (Figure 4.26). The resulting stresses produce

a tension field near the bar on the pull side and a compression field on the push side; this produces a change in bond resistance of the concrete, a decrease for tension and an increase for compression.

The second cause, related to poisson's ratio, is the expansion or contraction of the bar diameter. This results in a change of the bearing area of bar lugs against concrete. Tensile strain reduces the area of contact and results in decreased resistance; compressive strain increases the bearing area, resulting in an increased resistance. The bar axial force also changes the distance between lugs. This alters the state of stress in the concrete in the immediate area, there by affecting the strength and stiffness of bond.

## 4-3 REVIEW OF LOCAL BOND CONSTITUTIVE MODELS

A comprehensive model for the local bond stress-slip relationship under cyclic loads inside the reinforced concrete beam-column connections has been developed in the Earthquake Research Center of the University of California, Berkeley.[11,12,19,23,44]

The description of the local bond stress-slip relation between reinforcing bars and surrounding concrete, that has been empirically developed in Berkeley, consists of the following parts:

(1) Two monotonic envelopes, one in tension and one in compression, which are updated in each slip reversal as a function of incurred damage [curves (a) and (b) in

Figure 4.27(a)];

(2) A typical unloading-reloading path described by the current frictional bond resistance ($q_f$), and unloading curve (c) and a reloading curve (d), along with a set of rules for unloading and reloading in the case of incomplete cycles [Figures 4.27(a) and 4.27(b) ];

(3) A set of functional relation which allow updating the monotonic envelope values and the frictional bond resistance as a function of incurred damage.

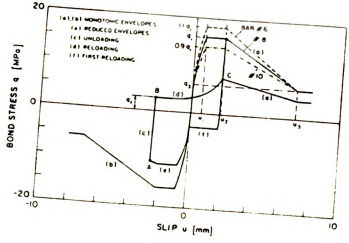


**(a) Complete Slip Reversal**

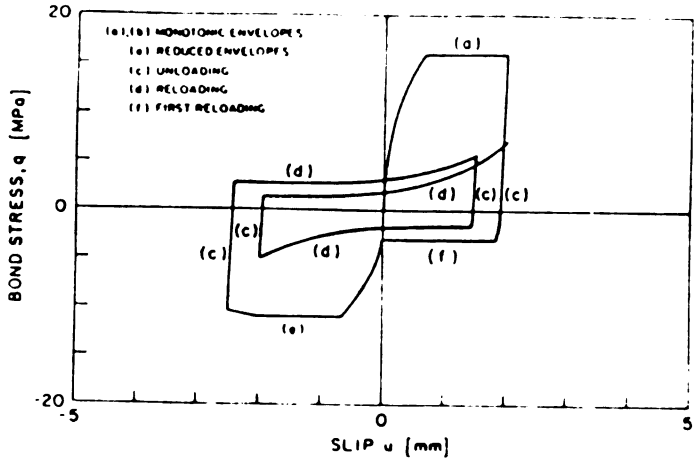


(b) Incomplete Slip Reversal

**Figure 4.27: Bond Model Developed In Berkeley Under Complete and Incomplete Slip Reversal (Ref. 19).**

The simplified monotonic envelope shown in Figure 4.27(a) simulates the experimentally obtained curve under monotonically increasing slip. It consists of an initial non-linear relationship $q = q_1 (u/u_1)^{0.4}$ , varied for $u \leq u_1$ followed by a plateau $q = q_1$ for $u_1 \leq u \leq u_2$. For $u \geq u_2$, q decreases linearly to the value of ultimate frictional bond resistaance $q_3$ at a slip value of $u_3$. This value is assumed to be equal to the clear distance between lugs of deformed bars. In the case of well confined regions, identical envelopes apply to tension and compression, i.e., to the case of the bar being pulled or pushed. In the unconfined case, two different envelopes curves have to be specified.

After imposing a load reversal at an arbitrary slip value [ point A in Figure 4.27(a)], unloading takes place along a steep straight line up to the point where the frictional bond resistance $q_f$ is reached [ point B in Figure 4.27(a)]. Further slippage in the same direction takes place at an almost constant bond stress [curve (d) in Figure 4.27(a)] until reaching near the under the reduced envelope curve [point C in Figure 4.27(a)] which has a slip value equal to the maximum or minimum slip imposed during previous cycles. Beyond point C, a bond stress-slip relationship similar to the virgin monotonic envelope but with a reduced value of bond stress is followed [curve (e) in Figure 4.27(a)]. This curve is called reduced envelope. In case that no slip has been previously imposed in one direction, reloading takes place along a horizontal line until reaching the reduced envelope [curve (f)]. If the slip imposed in one direction does not exceed the maximum slip attained during previous cycle, a typical cycle follows the path depicted in Figure 4.27(b).

Updated envelope curves are obtained in this model from the monotonic envelope by reducing the characteristic bond stresses $q_1$ and $q_3$ by a factor, which is formulated as a function of a parameter, called the "damage parameter", d, The relation proposed in Ref. 19 has the form:

$$q_1(N) = q_1(1-d) \qquad (4-3)$$

where $q_1$ represents the characteristic bond stress values

on the virgin envelope curve and $q_1(N)$ is the corresponding value after N cycles. For no damage, d=0, and the reduced envelope curves coincide with the monotonic curve. For complete damage, d=1, signifying that the bond is completely destroyed. The damage parameter, d was assumed in Ref. 19 to be a function of the total energy dissipation. The proposed relationship (Ref. 19) has the form:

$$d = 1-e^{-1.2(E/E_o)^{1.1}} \qquad (4-4)$$

in which E is the total energy dissipated and the normalizing energy $E_o$ corresponds to the energy absorped under monotonically increasing slip up to the value $u_3$ [ Figure 4.27(a)]. An additional relationship is used in establishing the frictional bond resistance $q_f$, which depends upon the previous slip value $u_{max}$ and relates $q_f$ to the ultimate bond resistance, $q_3(N)$ of the corresponding reduced envelope curve. For subsequent cycles between fixed values of slip, $q_f$ is further reduced by multiplying its initial value with a factor which depends on the energy dissipation by friction alone. Explicit expressions for the above relation are given in Ref. 19.

It is important to realize that the concept of relating damage to one scalar quantity, like the normalized dissipated energy, provides the basis for a relatively easy generalization of local bond behavior to cover random

excitations. Moreover, the bond stress-slip model can be used without any modification over a wide range of parameter values. Typical parameters include bar diameter, concrete strength, degree of confinement, and transverse pressure due to axial load. It should be noted in this context that, with the exception of the characteristic values of the monotonic envelope curve, all expressions prescribed in the model of Ref. 19 are cast in dimensionless forms. Thus only the characteristic values of the pertinent envelope curves are needed in order to establish the hysteretic bond stress-slip relation under any condition. These values can be based on experimental results or, alternatively, on the following empirical values derived in Ref. 19.

**Well-Confined Concrete:** The condition of well-confined concrete is present when a further increase in the amount of transverse reinforcement does not result in significant improvement of the local bond stress-slip behavior. This is depicted in Figure 4.9 presented earlier. In the case of well-confined concrete regions, identical envelopes apply to tension and compression. The following set of characteristic monotonic envelope values represent the average bond condition for #8 reinforcing bars in well confined concrete with a compressive strength equal to 4,350 psi (30 MPa):

$$u_1 = 0.394 \text{ in. } (1.0 \text{ mm})$$

$$u_2 = 0.118 \text{ in. } (3.0 \text{ mm})$$

$$u_3 = 0.413 \text{ in. } (10.5 \text{ mm})$$

$$q_1 = 19.575 \text{ ksi } (13.6 \text{ N/mm}^2)$$

$$q_3 = 0.725 \text{ ksi } (5.0 \text{ N/mm}^2)$$

$$\alpha = 0.4$$

(4-5)

Due to inevitable scatter of experimental results, the values of $q_1$, and $q_3$, and $\alpha$ may well vary up to $\pm$ 15%.

For non-standard condition (bar size different from #8, concrete strength different from 4,350 psi, bar spacing less than $4d_b$, external pressure applied or related rib area different from 0.065), the above characteristic monotonic envelope values for well-confined concrete should be modified as discussed in the following:

(1) The influence of concrete strength can be taken into account by multiplying $q_1$, and $q_3$ with the factor $\sqrt{(f_c'/4,350)}$ where $f_c'$ is the concrete compressive strength in psi. Furthermore, the value of $u_1$ should be reduced approximately in proportion to $\sqrt{(4,350/f_c')}$.

(2) If the clear spacing between bars is smaller than $4d_b$, where $d_b$ is the bar diameter, $q_1$ and $q_3$ should be reduced using the information given in Figure 4.28. The following expressions have been derived in this study on the basis of this figure:

For $s < 4d_b$ $\quad q(s)/q(4d_b) = 1-0.833e^{-1.61(s/d_b)^{0.79}}$

(4-6)

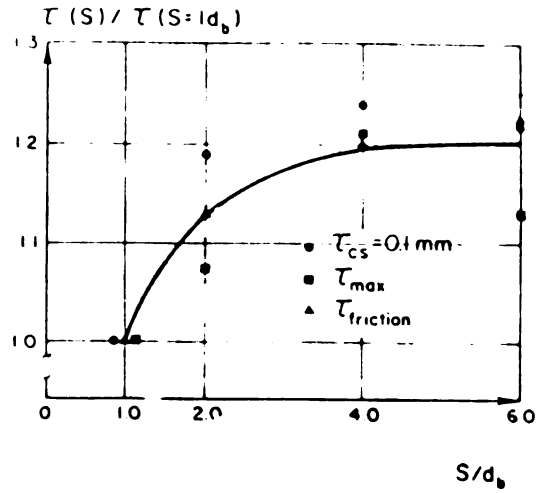


Figure 4.28: Influence of Clear Bar Spacing s/$d_b$ On Bond Resistance (Ref. 19).

(3) The influence of external pressure (e.g. axial compressive column force) can be taken into account by increase in $q_1$ and $q_3$ according to Figure 4.29. Least square curve fitting to test results resulted in the following expression:

$$q(p)/q(p=0) = 1.3-0.3e^{-0.00103p} \qquad (4-7)$$

where: p is the transverse pressure in psi.

(4) If #6 or #10 bars are used, it is recommended to increase or decrease, respectively, $q_1$ by 10%.

(5) If the related rib area , $\alpha_{sR}$, differs from the value 0.065, its influence should be taken into account by modifying $u_1$ and $q_1$ using the data given in Ref. 19.

(6) The given values for $u_1$ , $u_2$, and $u_3$ should be multiplied by a factor $c_1/0.41$, where $c_1$ is the clear

spacings between lugs in inches, but this modification should not be greater than ±30%.

(7) The unloading slope is equal to 26,100 psi (180 MPa) for #8 bars. It should be modified in the same way as $q_1$ for different conditions.

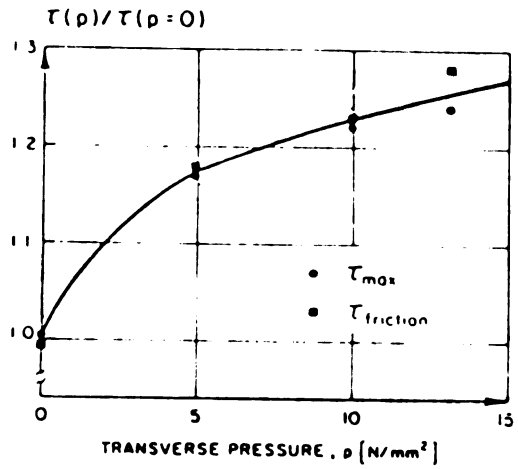


Figure 4.29: Influence of Transverse Pressure On Bond Resistance (Ref. 19).

**Unconfined Concrete:** Unconfined concrete occurs in the column cover region of interior and exterior R/C joints Figure 4.30. It is possible to generalize the local bond stress-slip relation for confined concrete regions by introducing the following modifications:

(1) A different monotonic envelope is specified for

positive slip values than for negative slip values;

(2) The normalizing energy $E_o$ used in the computation of damage is chosen to be the largest between $E_o^+$ and $E_o^-$, which are, respectively, the areas under the monotonic envelopes for positive and negative slip values up to the slip value of $u_3$. To take into account different rates of damage in the two directions of loading, the pertinent total dissipated energies E, used to compute the reduced envelope are multiplied by an amplification factor $\beta$, which is different in the two opposite slip directions. Similar rules for computing damage apply to the friction part of the curve.

The following envelope values are suggested for #8 bars embedded in unconfined concrete with compressive strength of 4,350 psi or 30 MPa (Ref. 19):

Envelope values for the case that the bar is pulled (Figure 4.30):

$$u_1 = 0.0118 \text{ in. } (0.3 \text{ mm})$$
$$u_2 = 0.0118 \text{ in. } (0.3 \text{ mm})$$
$$u_3 = 0.0394 \text{ in. } (1.0 \text{ mm})$$
$$q_1 = 0.725 \text{ ksi } (5.0 \text{ N/mm}^2)$$
$$q_3 = 0$$
$$\alpha = 0.40$$

(4-8)

Envelope values for the case that the bar is pushed (Figure 4.30):

$$u_1 = 0.0394 \text{ in. } (1.0 \text{ mm})$$

$$u_2 = 0.1181 \text{ in. } (3.0 \text{ mm})$$

$$u_3 = 0.413 \text{ in. } (10.5 \text{ mm})$$

$$q_1 = 2.900 \text{ ksi } (20.0 \text{ N/mm}^2)$$

$$q_3 = 1.088 \text{ ksi } (7.5 \text{ N/mm}^2)$$

$$\alpha = 0.40$$

(4-9)

The same modification as in the case of confined concrete apply for different bar diameters and concrete compressive strengths.

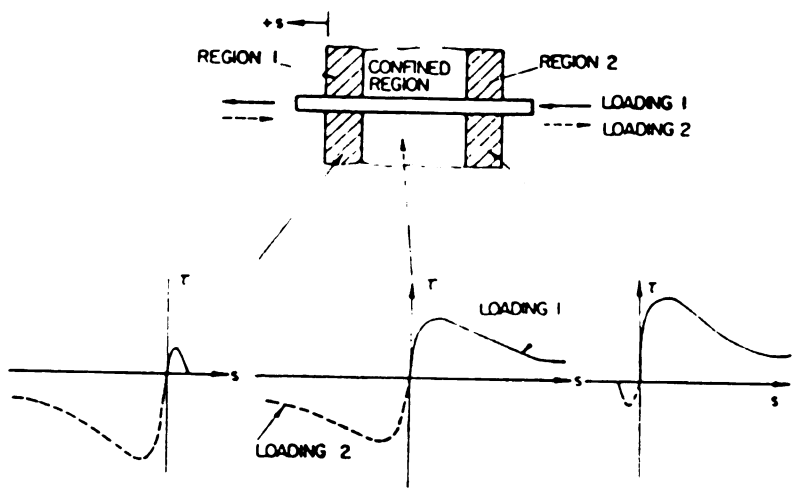


Figure 4.30: Different Regions and Corresponding Bond Stess-Slip Envelope Curves In Interior Joint (Ref. 19).

Less detailed models for the local bond behavior under

cyclic loads have been introduced in Refs. 39, 52, 56. The first analytical model for the local bond stress-slip relationship under cyclic loading was proposed by Morita and Kaku.[39] This model is shown in Figure 4.31. The monotonic envelopes which are different for loading in tension and compression, and for confined and unconfined concrete, are bilinear. The assumed bond stress-slip relationship for the first cycle coincides relatively well with the behavior observed in tests. This model, however, neglects any deterioration in the envelope curve or frictional bond resistance. The model is sufficiently accurate for a small number of cycles between relatively small slip values with corresponding bond stresses smaller than about 80% of the monotonic bond strength. It is, however, inaccurate for a large number of load cycles, and it is not valid for slip values larger than the one corresponding to 80% of the bond strength.

Another bond hysteretic model has been developed by Tassios.[53] As shown in Figure 4.32, the monotonic envelope in this model consists of six succesive straight lines. The coordinates of the controlling points A to E, which have the same physical meanings as describe earlier for the detailed model of Ref. 19, have been theoretically evaluated and given as functions of the relevant influencing parameters in Ref. 53. The same bond stress-slip relationship is assumed regardless of whether the bar is pulled or pushed. After loading to a slip value greater

than the value of slip corresponding to point B on the envelope curve shown in Figure 4.32, the value of the bond stress-slip relationship for loading in the reverse direction are reduced by one-third compared to the monotonic envelope. The bond stress-slip relationship for reloading and for subsequent cycles between fixed slip values is somewhat simplistic in this model compared to the real behavior. However, the deterioration of the bond resistance at peak slip and that of the frictional bond resistance are taken into account. when increasing the slip beyond the previous peak slip value, it is assumed that the monotonic envelope is reached again. This model an improvement over the one developed by Morita and Kaku[39] because the descending branch of the local bond stress-slip relationship is considered, and the influence of load cycles on bond deterioration is also taken into account. However, the assumption that for slip values larger than the peak value in the previous cycle, the monotonic envelope is reached again and followed thereafter, is not representative of the experimentally observed behavior. For monotonic loading, the model seems accurate for the total slip range. However, for the cyclic loading, it is valid only for slip values smaller than the slip at ultimate bond strength.

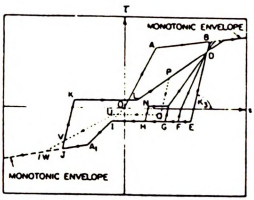


$T_D = \beta \cdot T_B$ $T_K = \alpha \cdot T_J$ $s_L = (s_B + s_J)/2$

$T_V = \beta \cdot T_J$ $T_N = \alpha \cdot T_H$ $s_U = (s_J + s_P)/2$

$T_E = \alpha \cdot T_B$ $T_Q = \alpha \cdot T_P$ $s_Q = s_P/2$

$K_3 = 400\ N/mm^3$

$\alpha = 0.18$

$\beta = 0.9$ $s \le 0.05\ mm$

$\beta = 0.9 - 0.44(s - 0.05)$ $0.05 \le s \le 0.3\ mm$

**Figure 4.31:** Analytical Model For Local Bond Stress-Slip Relationship Proposed By Morita/Kaku (Ref. 39).

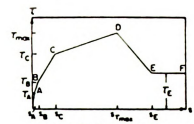


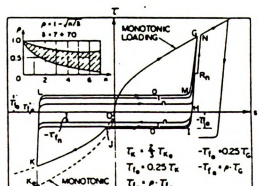


**Figure 4.32:** Analytical Model For Local Bond Stress-Slip Relationship Proposed By Tassios (Ref. 53).

## 4-4 REVIEW OF ANALYTICAL MODELS FOR PULL OUT BEHAVIOR OF EMBEDDED BARS

The above discussion mainly concentrated on the local bond stress-slip behavior. The ultimate goal is, however, to analyze the overall behavior of embedded bars. Refs. 11, 23, and 53 have suggested some methods for using the local bond stress-slip relationship in predicting the overall behavior of embedded bars subjected to cyclic loads.

In the typical method developed in Ref.11, the actual behavior of a bar of finite length embedded in a concrete block has been studied using an idealized one-dimensional mathematical model (Figure 4.33). The governing equilibrium equation of this model may be written as:

$$dN(x)/dx - q(x) = 0 \qquad (4\text{-}10)$$

where: $q$ = bond force per unit length

$= \pi d_b \tau(x)$;

$N$ = bar force

$= A\sigma(x)$;

$\tau$ = bond stress;

$d_b$ = bar diameter;

$A$ = area of the bar cross-section.

This relation expresses equilibrium of an infinitesimal portion of the bar [Figure 4.34(a)]. It has to be coupled with the constitutive laws for steel and bond, which can be expressed as:

$$\sigma = \sigma(\epsilon(x)) \approx \hat{\sigma}\left[\frac{ds(x)}{dx}\right]$$
$$\tau = \hat{\tau}(s(x)) \qquad (4\text{-}11)$$

where s(x) is the slip along the bar. Note that here the influence of concrete deformation on slip has been considered negligible, as commonly assumed. As a consequence, the strain in steel, $\epsilon$ , has been set equal to ds/dx.

Boundary values are specified at the two end points of the bar. Three different cases, in particular, has been considered [Figure 4.34(b)]:

(1) The displacement (slip) values at the two ends are assigned (this is the case , for example, of a pull-push test with displacement controlled at both ends).

(2) The displacement is assigned at one end only, together with the axial force at the other end (this is the case of a pull test with displacement controlled at the pull end).

(3) while at one end the displacement is assigned, at the other end the magnitude of force is constrained to be equal to the one at the first end (this corresponds to a pull-push test arrangement where the displacement is controlled at one end only, but the pull and push forces are constrained to have same magnitude).

Ref. 11 suggests an incremental solution process for the bond nonlinear equation presented above. In this solution, small increments of the assigned boundary conditions define the loading. In Ref. 11, the bond

equations are recast into the following nonlinear initial value form:

$$dN(x)/dx - q(x) = 0$$
$$N(x) = \hat{N}(\epsilon(x)) = \hat{N}(ds(x)/dx) \qquad (4\text{-}12)$$
$$q(x) = \pi d_b \tau(x), \text{ with } \tau(x) = \hat{\tau}(s(x))$$

The above equations govern the behavior on the interval [0,L] of the real axis x [Figure 4.34(c)], with the initial conditions:

$$\epsilon(0) = (ds/dx)_{x=0} = \epsilon_1 ;$$
$$s(x=0) = s_1$$

In order to solve this problem numerically, the interval [0,L] is first divided at the position (or stations) $x_i$ ($i = 1,2,.....,n$; $x_1=0$, $x_n=L$, $x_i = x_{i+1}-x_i$), by n points into n-1 sub-intervals [Figure 4.34(c)].

Once the values $N_i$, $q_i$, $\epsilon_i$, and $s_i$ of the functions N(x), q(x), $\epsilon$(x), and s(x) at station i are known, the solution is advanced to the next station i+1 using the following relations:

$$s_{i+1} = s_i + [(\epsilon_i + \epsilon_{i+1})/2]\Delta x_i$$
$$N_{i+1}(\epsilon_{i+1}) - N_i - [\{q_i + q_{i+1}(s_{i+1})\}/2]\Delta x_i = 0 \qquad (4\text{-}13)$$

which express an approximate integration of the bond equations given earlier on the sub-interval $(x_i, x_{i+1})$. The above two equations combined together result in a nonlinear equation with only one unknown $\epsilon_{i+1}$, the solution of which requires repeated evaluation of the functions $N(\epsilon)$, q(s) at

point i+1. Once $\epsilon_{i+1}$ has been determined, and $s_{i+1}$, $N_{i+1}$, and $q_{i+1}$ are available, the procedure can be applied to the next sub-interval and continued up to the end point n.

The type of integration scheme presented above is implicit and has the disadvantage of requiring at each step (interval) the iterative solution of a nonlinear equation. Furthermore, since the regular boundary conditions presented in Figure 4.34(b) define the conditions at both ends, a shooting technique should be implemented and this involves additional level of iterations that makes the solution very time-consuming.

The method presented in Ref. 53 is also very similar to the above method of Ref. 11 except that the concrete strains are approximately taken into account in Ref. 53.

An interesting aspect of model presented in Ref. 11 and 23 is the distinction between confined and unconfined concrete in specifying the bond stress-slip envelope curves along the bar embedded length. According to these references, the dividing line between the confined and unconfined conditions can not be sharply defined in the joint. Therefore, it is suggested to assume a gradual transistion between the region of well-confined concrete and the region of unconfined concrete. In summary the following regions have been assumed in Ref. 23 (Figure 4.35) on the basis of a limited number of test results.

(1) Unconfined concrete extends $ld_b$ into the column cover region on both ends of the joint, where $d_b$ is the

reinforcing bar diameter;

(2) Transistion region between unconfined and confined concrete extends $2d_b$ from the end of the unconfined region on both ends of the joint,

(3) The remaining length inside the column core is considered as confined concrete region.

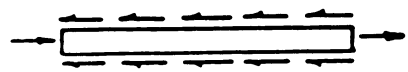

One-Dimensional Model

Figure 4.33: Physical Idealization of Anchored Bar.

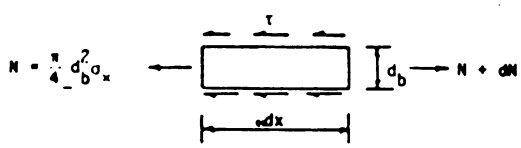


$$\frac{dN(x)}{dx} - d_b = 0$$

$\sigma(x) = \sigma(\varepsilon(x))$, $\tau(x) = \tau(s(x))$

$\sigma(\varepsilon)$ = constitutive law for steel

$\tau(x)$ = " " " Bond

(a) Different Equation For Bond

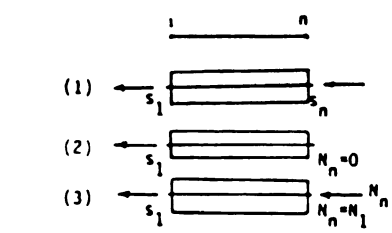


(b) Boundary Conditions Considered

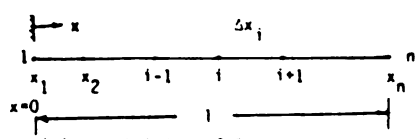


(c) Subdivision of Bar

Figure 4.34: Mathematical Model of Deformed Bar.

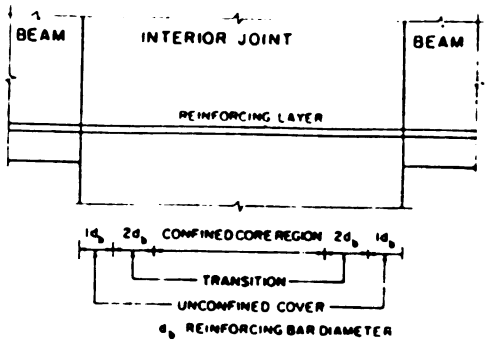


Figure 4.35: Subdivision of Bar Anchorage Length Into Different Bond Regions (Ref. 23).

# CHAPTER 5

# ANALYTICAL STUDIES ON PULL-OUT BEHAVIOR OF BEAM LONGITUDINAL BARS BONDED BEAM-COLUMN CONNECTIONS

## 5-1 INTRODUCTION

This Chapter illustrates the analytical studies performed on the pull-out behavior on the beam longitudinal bars embedded in interior beam-column connections. First an improved local bond stress-slip relationship is presented and then a new modeling technique that is based on the displacement method of analysis is presented. This technique is significantly more efficient than the available ones. The Chapter concludes with a parametric studies on the pull-out behavior of embedded bars.

## 5-2 AN IMPROVED LOCAL BOND CONSTITUTIVE MODEL

The model developed in Ref. 19 (presented in section 4-3 ) assumes that on the reloading curve, the frictional bond resistance remain constant before reaching the peak slip value of the previous cycle in the corresponding direction, and then the resistance jumps suddenly to the reduced envelope curve Figure 5.1(a). In order to improve this model, Ref. 23 has suggested a gradual increase in the force carried by the bar according to a fourth degree polynomial [Figure 5.1(b)]. The constant friction assumption of Ref. 5 does not agree well with the test results, and the gradual increase of the bond resistance during the loading proposed in Ref. 23 adds to the complexity of the model. In this study, the following

simple and realistic law for reloading up to the peak slip value in the previous cycle was developed [Figure 5.1(c)].

If after the first loading up to point A shown in Figure 5.1(c), unloading and reloading takes place, after the elastic part is over in point B, a constant frictional resistance is assumed to be effective up to reaching the envelope curve in the reversed direction at point C. This is similar to the assumption of Ref. 19. In the subsequent reloading, however, the path is suggested to be different. In the proposed model it is assumed that the frictional resistance, that becomes effective at point E in Figure 5.1(c), remains constant up to point F the slip value of which is the average of the maximum and minimum slip value so far reached at points A and D, respectively, except that the sign of the slip value at F should be different from the one at E, otherwise the slip at F should be taken equal to zero. This means that line EF either crosses the vertical axis with zero slip value or at least reaches this axis. After reaching point F, if the reloading is continued, the path follows a line drawn from F to G on the reduced envelope curve as shown in Figure 5.1(c). Thereafter, the reduced envelope curve is followed. In incomplete cycles, if the elastic reloading path intersects EF between E and F [see path HIJK in Figure 5.1(c)], thereafter the path follows EF up to F, and then goes linearly towards G as discussed above. In case of incomplete cycles that intersect the line EF outside the E-

F range [like path HILM in Figure 5.1(c) ], then from M the reloading path directly goes towards G on a linear path.

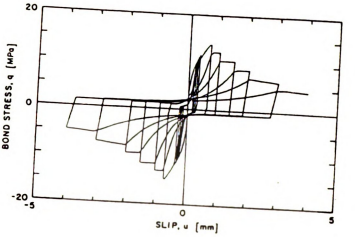


(a) Model of Ref. 23

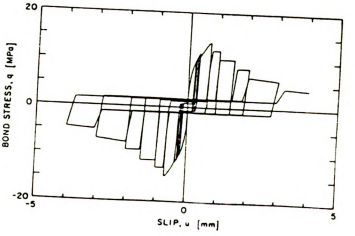


(b) Model of Ref. 19

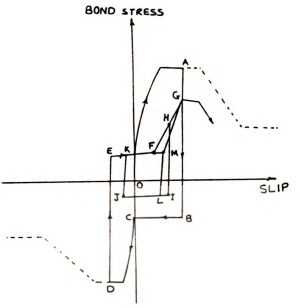


(c) Improvement on the Reloading Branch of Berkeley Models

Figure 5.1: Comparison of Hysteretic Bond Stress Behavior With Models Proposed at Berkeley.

Figures 5.2(a), 5.2(b), and 5.2(c) that compare an experimental cyclic bond stress-slip curve with the ones predicted by the proposed model and the model of Ref. 19 show the improvements achieved by the proposed modification of the model of Ref. 19.

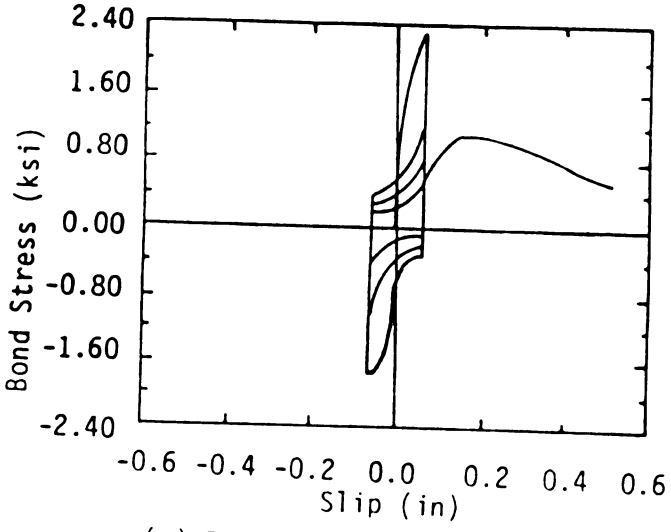


(a) Test (Ref. 19)

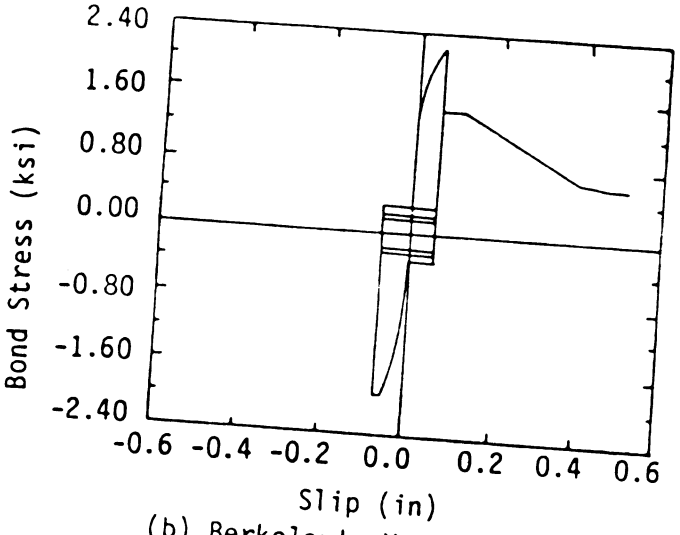


(b) Berkeley's Model (Ref. 19)

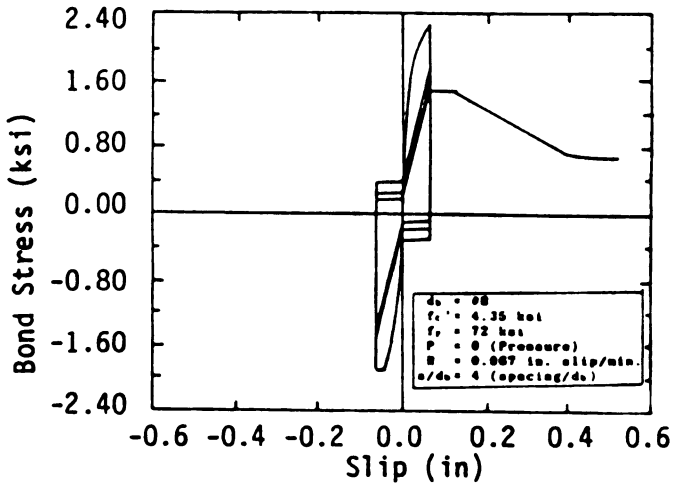


(c) Proposed Modification

Figure 5.2: Comparison of Cyclic Bond Stress-Slip (Test and Theory).

Figures 5.3, 5.4, 5.5, 5.6, and 5.7 show some cyclic test results as well as the predictions of the proposed version of the Berkeley's model. The properties of the test specimen[19] are also shown in these figures. The model is observed to predict the test results with reasonable accuracy.

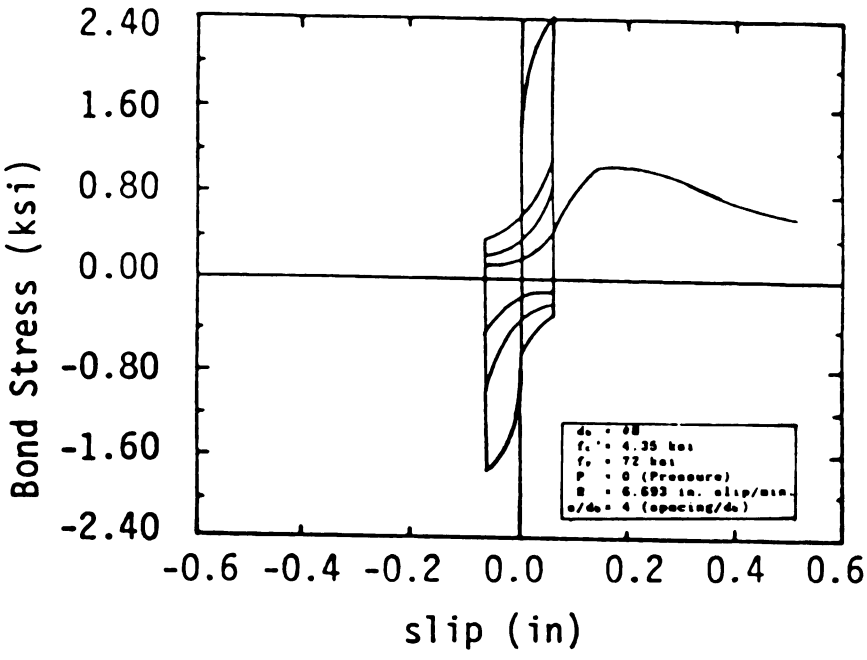


(a) Test (Ref. 19)

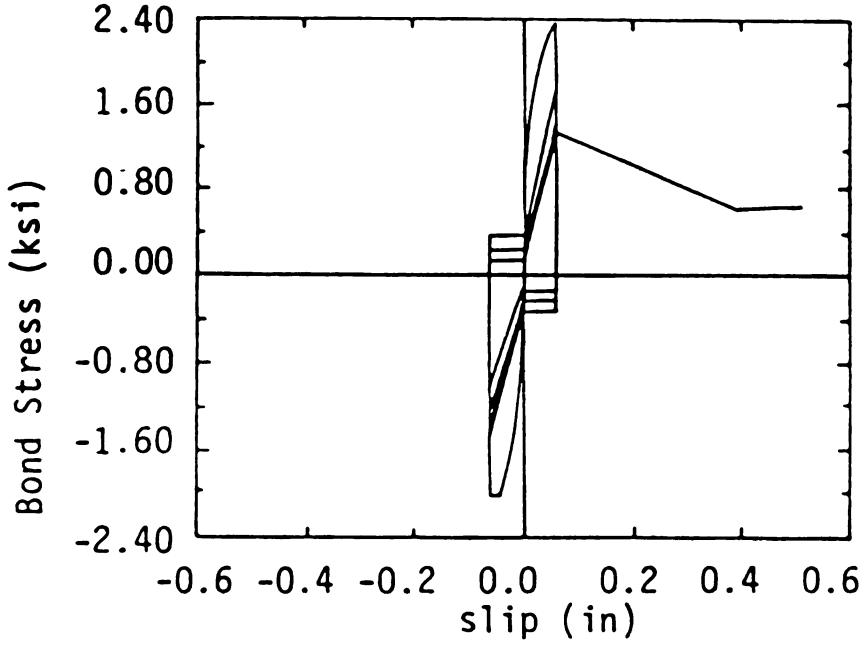


(b) Proposed Model

Figure 5.3: Comparison of Model With Test (Ref. 19).

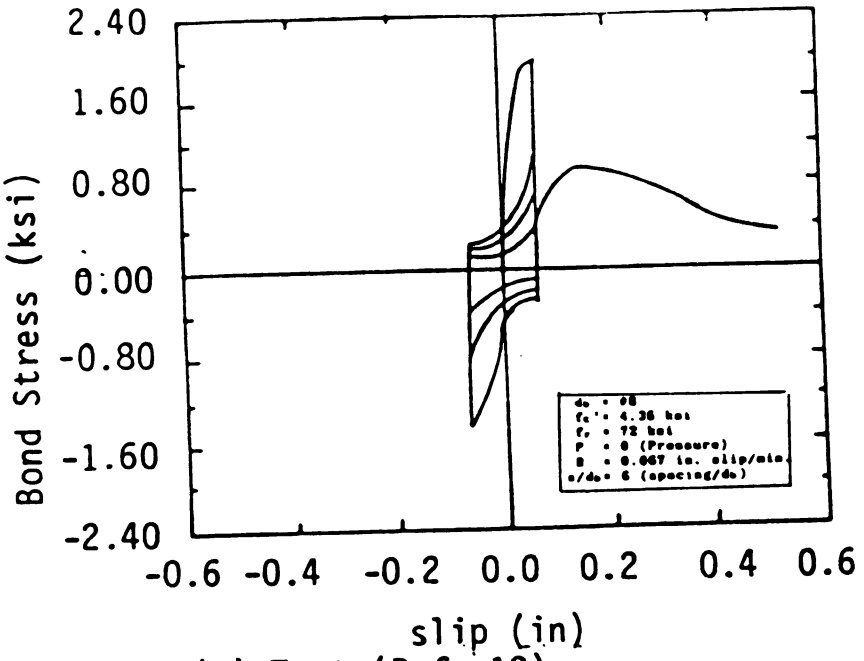


(a) Test (Ref. 19)

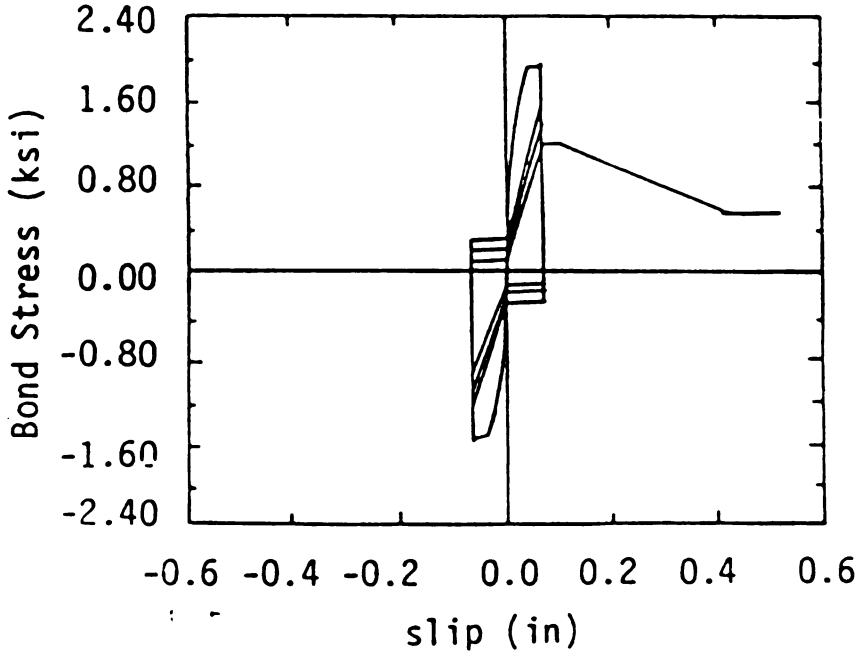


(b) Proposed Model

Figure 5.4: Comparison of Model With Test (Ref. 19).

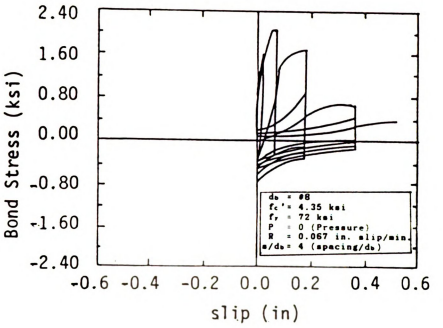


(a) Test (Ref. 19)

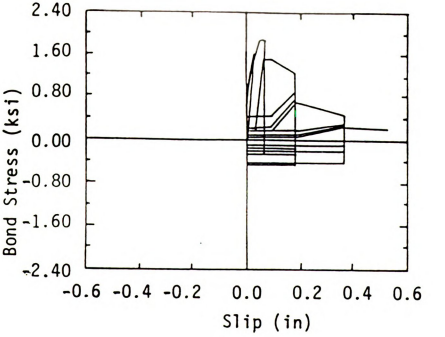


(b) Proposed Model

**Figure 5.5: Comparison of Model With Test (Ref. 19).**

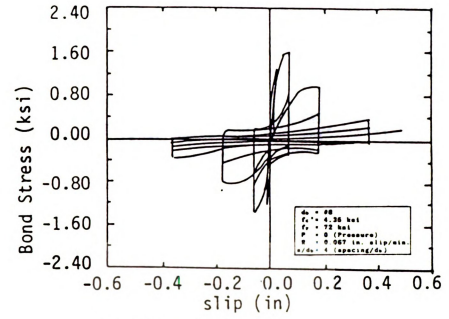


(a) Test (Ref. 19)

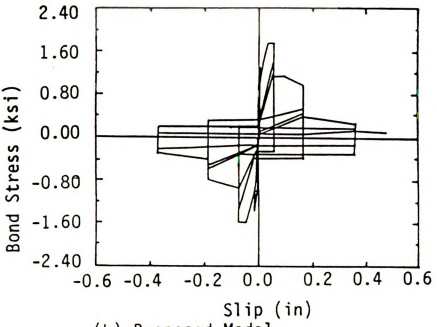


(b) Proposed Model

Figure 5.6: Comparison of Model With Test (Ref. 19)

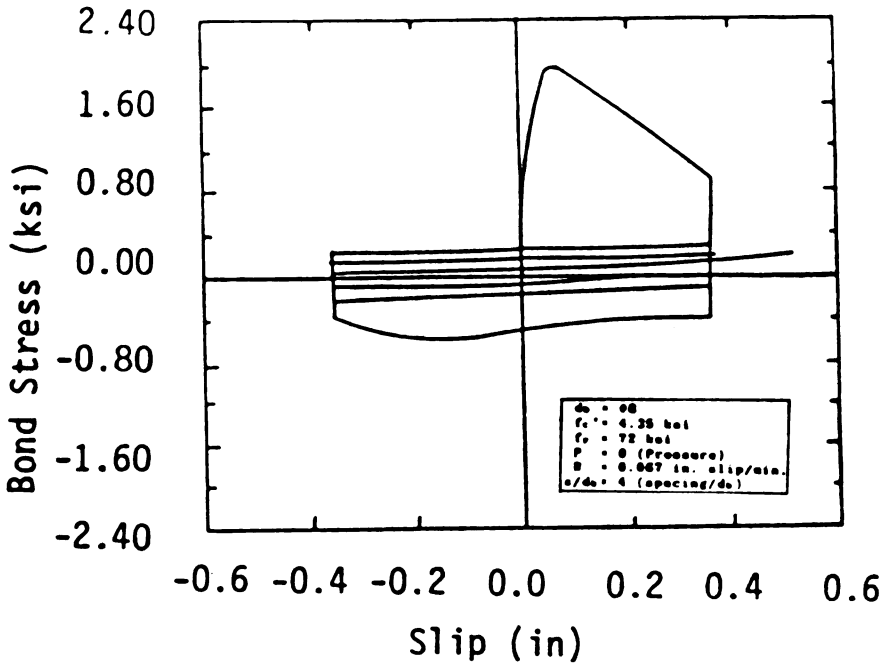


(a) Test (Ref. 19)

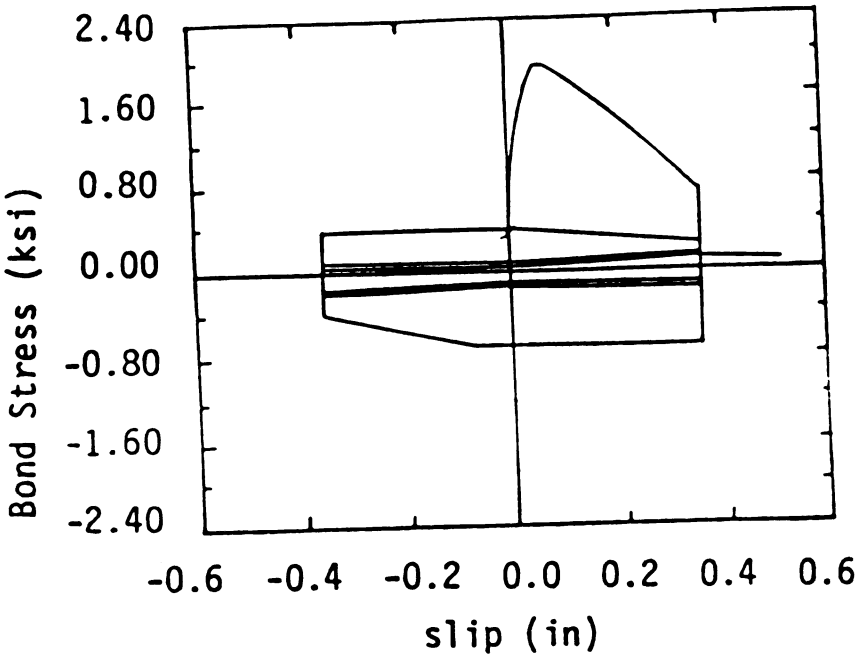


(b) Proposed Model

Figure 5.7: Comparison of Model With Test (Ref. 19).

## 5-3 A NEW ANALYTICAL MODEL FOR PULL-OUT BEHAVIOR OF EMBEDDED BARS

In this study, a technique based on the displacement method of analysis has been developed for predicting the behavior of anchored bars under the action of random load histories. This approach does not involve iterations at each load step, and thus it is time efficient for computer analysis.

In finite element modeling of reinforced concrete structures, the bond between steel and concrete is sometimes idealized by discrete springs connecting the bar at different points along its length to concrete.[4] In the model developed in this study, the idea of idealizing bond with discrete springs has been employed for deriving a more efficient procedure for predicting the behavior of anchored bars with any of the boundary conditions shown in Figure 4.34(b).

The proposed model is shown in Figure 5.8. Each spring in this model represents the bond resistance provided by its tributary length of the anchored bar. In this one-dimensional model, the concrete strains are assumed to have negligible effects on the anchored bar behavior[11] and thus the springs in Figure 5.8 are assumed to be rigidly fixed at the ends connected to concrete.

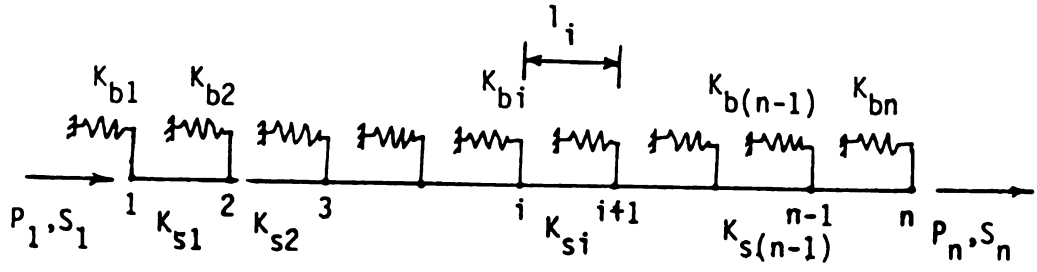


**Figure 5.8: The Proposed Idealization of the Deformed Bar-Concrete Interaction.**

Construction of the tangent stiffness matrix of the anchored bar model in Figure 5.8 requires knowledge of the steel and bond constitutive laws. Assuming that these laws are known, and the history and values of dispacement (slip) at any of the discrete points along the bar length Figure 5.8 are available, then the bond tangent stiffness ($k_{t\,i}$) and the steel tangent stiffness ($k_{f\,i}$) can be derived. The stiffnesses of the springs ($k_{s\,i}$) and the steel segments ($k_{b\,i}$) can be computed at each stage of loading history:

$$k_{b\,i} = k_{t\,i}(\pi d_b) l_i \qquad (5\text{-}1)$$

$$K_{s\,i} = k_{f\,i}(\pi d_b^2/4)/l_i \qquad (5\text{-}2)$$

where: $d_b$ = bar diameter;

$l_i$ = length of the ith steel segment (Figure 5.8)

Knowing the tangent stiffnesses, steel segment and springs, the overall tangent stiffness matrix ($k_T$) of the idealized system shown in Figure 5.8 with n degrees of fredom (n is the number of discrete points along the bar length) can be constructed as follows:

$$K_T = \begin{array}{c} \\ 1 \\ 2 \\ 3 \\ \\ \\ \\ n-1 \\ n \end{array} \begin{array}{c} \begin{array}{cccccccc} 1 & 2 & 3 & & n-2 & n-1 & n \end{array} \\ \begin{bmatrix} K_{b1}+K_{s1} & -K_{s1} & 0 & \cdots & 0 & 0 & 0 \\ -K_{s1} & K_{b2}+K_{s1}+K_{s2} & -K_{s2} & \cdots & 0 & 0 & 0 \\ 0 & -K_{s2} & K_{b3}+K_{s2}+K_{s1} & \cdots & 0 & 0 & 0 \\ \vdots & \vdots & \vdots & \cdots & \vdots & \vdots & \vdots \\ 0 & 0 & 0 & \cdots & -K_{s(n-2)} & K_{b(n-1)}+K_{s(n-2)}+K_{s(n-1)} & -K_{s(n-1)} \\ 0 & 0 & 0 & \cdots & 0 & -K_{s(n-1)} & K_{bn}+K_{s(n-1)} \end{bmatrix} \end{array} \quad (3.16)$$

Eqn. (5-3) (tangent stiffness matrix) defines the relationship between incremental end forces ($dP_1$ and $dP_n$ in Figure 5.8) and the incremental slip values along the bar length ($dS_1$, $dS_2$,.., ,$dS_i$,....,$dS_n$) according to the following expression:

$$\begin{Bmatrix} dP_1 \\ 0 \\ . \\ . \\ . \\ 0 \\ dP_n \end{Bmatrix} = K_T \begin{Bmatrix} dS_1 \\ dS_2 \\ . \\ . \\ . \\ dS_{n-1} \\ dS_n \end{Bmatrix} \qquad (5\text{-}4)$$

or assuming that $F = K_T^{-1}$.

$$\begin{Bmatrix} dS_1 \\ dS_2 \\ dS_2 \\ . \\ . \\ . \\ dS_{n-1} \\ dS_n \end{Bmatrix} = F \begin{Bmatrix} dP_1 \\ 0 \\ 0 \\ . \\ . \\ . \\ 0 \\ dP_n \end{Bmatrix} \qquad (5\text{-}5)$$

It can be concluded from Eqn. (5-5) that:

$$dS_1 = f_{1,1}\,dP_1 + f_{1,n}\,dP_n \qquad (5\text{-}6)$$

$$dS_n = f_{n,1}\,dP_1 + f_{n,n}\,dP_n \qquad (5\text{-}7)$$

where: $f_{i,j}$ = the element in the ith row and the jth column

of matrix F.

Eqns. (5-6) and (5-7) give the incremental values of end slip in terms of the incremental end forces. Such expressions are helpful if the loading is defined by assigning the two end forces. The loads applied on the anchored bars are, however, generally defined by assigning one of the three boundary conditions shown in Figure 4.34(b). In the following, Eqns. (5-6) and (5-7) are reorganized for use with any of these three boundary conditions.

Case 1:- slip assigned at both ends: solving Eqns. (5-6) and (5-7) for the incremental end forces we get:

$$dP_1 = dS_1/f_{1,1} - (dS_n f_{1,1} - dS_1 f_{n,1})/(f_{n,n} f_{1,1}^2/f_{1,n} - f_{n,1} f_{1,1}) \quad (5\text{-}8)$$

$$dP_n = (dS_n f_{1,1} - dS_1 f_{n,1})/(f_{n,n} f_{1,1} - f_{1,n} f_{n,1}) \quad (5\text{-}9)$$

Eqns. (5-8) and (5-9) give the incremental end forces in terms of the input values of the incremental end slips.

Case 2:- slip assigned at one end with force at the other end equal to zero: by substituting dP with zero in Eqns. (5-6) and (5-7), and solving for $dP_n$ and $dS_n$ we get:

$$dP_n = dS_n/f_{n,n} \quad (5\text{-}10)$$

$$dS_1 = (dS_n - f_{1,n})/f_{n,n} \quad (5\text{-}11)$$

Case 3:- slip assigned at one end with the force at two ends constrained to be equal: by substituting $dP_n$ and $dP_1$, and cancelling $dP_1$ in Eqns. (5-6) and (5-7) the following expression can be derived for the unknown value of $dS_1$ in

terms of $dS_n$:

$$dS_1 = dS_n.(f_{1,n}+f_{1,1})/(f_{n,n}+f_{n,1}) \qquad (5\text{-}12)$$

The incremental end forces can then be computed using Eqn. (5-6) or (5-7).

For any of the above boundary conditions, the solution algorithm at each load step will be as follows:

(1) Using the slip values of the previous load step, construct the overall tangent stiffness matrix of the system using bond and steel constitutive laws with Eqns. (5-1), (5-2), and (5-3). Invert this tangent stiffness matrix to get matrix F (and its elements $f_{1,1}$, $f_{1,n}$, $f_{n,1}$, and $f_{n,n}$);

(2) In case 1: Given $dS_1$ and $dS_n$, find $dP_1$ and $dP_n$ using Eqns. (5-8) and (5-9),

In case 2: Given $dS_n$ and $dP_1=0$ find $dP_n$ and $dS_1$ using Eqns. (5-10) and (5-11),

In case 3: Given $dS_n$ and $dP_1=dP_n$, find $dS_1$ from Eqn. (5-12) and $dP_1=dP_n$ from Eqn. (5-6) or (5-7).

(3) Find all the incremental slip values along the bar length using Eqn. (5-4).

The above algorithm gives the slip values along bar the length at the end of the current time step. This is the information needed for constructing the new tangent stiffness matrix for the next time step. Consequently, the above algorithm can be repeated for the consequent load step up to the end of the loading history.

The above approach to analysis of anchored bars, unlike the other available methods,[4,11,19] does not involve iterative solution of nonlinear equation and thus it is time efficient for analysis by computer. The proposed approach is also based on the displacement method of analysis that is commonly used in conventional computer programs for static and dynamic analysis of complete structures. Consequently, this model of anchored bars can be incorporated into such programs conviniently. This might provide researchers with a practical tool for studying the effects of bar slippage (e.g. in reinforced concrete beam-column connections) on the overall response of the reinforced concrete structures.

## 5-4 COMPARISON OF THE PROPOSED EMBEDDED BAR MODEL WITH TEST RESULTS

The proposed embedded bar model together with a bilinear hysteretic model of steel (Figure 5.9) and bond constitutive laws presented in section 5-2 [Figure 5.1(c)] were incorporated into a computer program for predicting the behavior of anchored bars under random cyclic loads. The analytical results were compared with test results reported in Ref. 56 in order to check the accuracy of the proposed model.

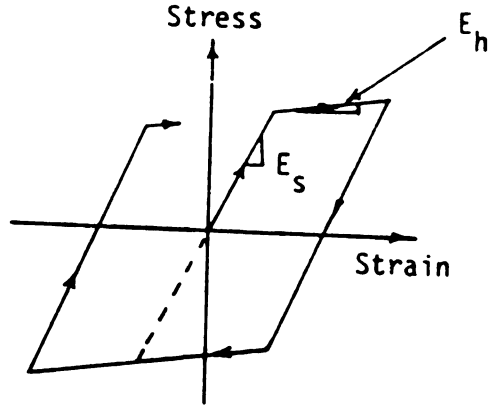


Figure 5.9: Steel Constitutive Model.

In all of the selected tests, #8 deformed bars with yield strength of 65,000 psi (450 MPa) were anchored in a confined concrete specimens (Figure 5.10) with compressive strength of 4,350 psi (30 MPa). The anchorage length was 25 times the bar diameter. The load histories in the selected tests included: monotonic pull only [boundary conditions (2) in Figure 4.34(b)], monotonic pull-push and cyclic pull-push both with equal end forces [boundary condition (3) in Figure 4.34(b)].

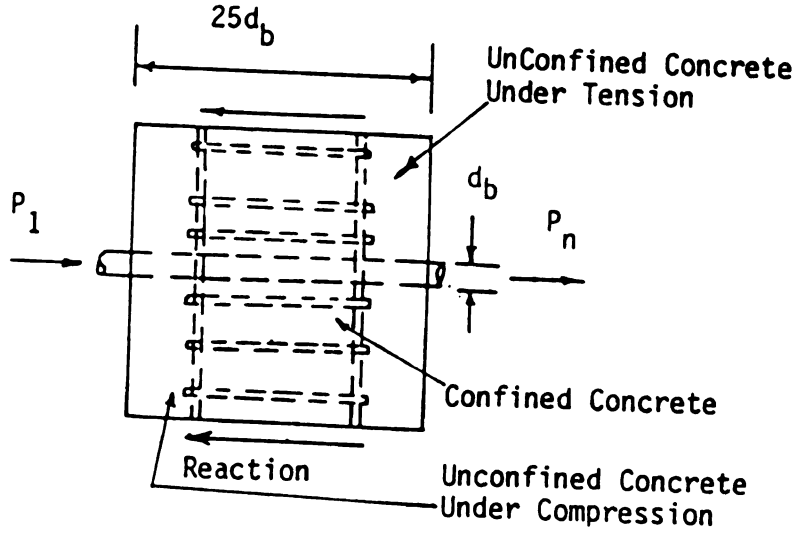


Figure 5.10: Test Specimen Used For Analytical Studies.

The anchored bar was modeled as shown in Figure 5.8 with 25 springs simulating the bond between steel and concrete. In the model it was assumed that the cover (unconfined) concrete thickness was equal to four times the bar diameter on each side.

Figure 5.11(a) compares the experimental and theoretical end force-end slip relationships for the specimen tested under monotonic pull only, and Figures 5.11(b), 5.11(c), and 5.11(d) present similar comparisons for the distributions of slip, bar force, and bond force per unit length, along the anchorage length of this specimen at an end slip value of 6 mm (0.24 in). Comparison between test and theory in all these figures is observed to be reasonably well in aggrement.

The comparison between the experimental and theoretical end force-end slip relationships at the pull end of the bar for the specimen subjected to the monotonic push-pull at the two ends (with equal end forces) is presented in Figures 5.12(a). Figures 5.12(b), 5.12(c), and 5.12(d) also present the comparisons of the distributions of slip, bar force , and bond force per unit length along the anchorage length of this specimen at a slip value of 6 mm at the pulled end. A reasonable comparison is obtained in this case.

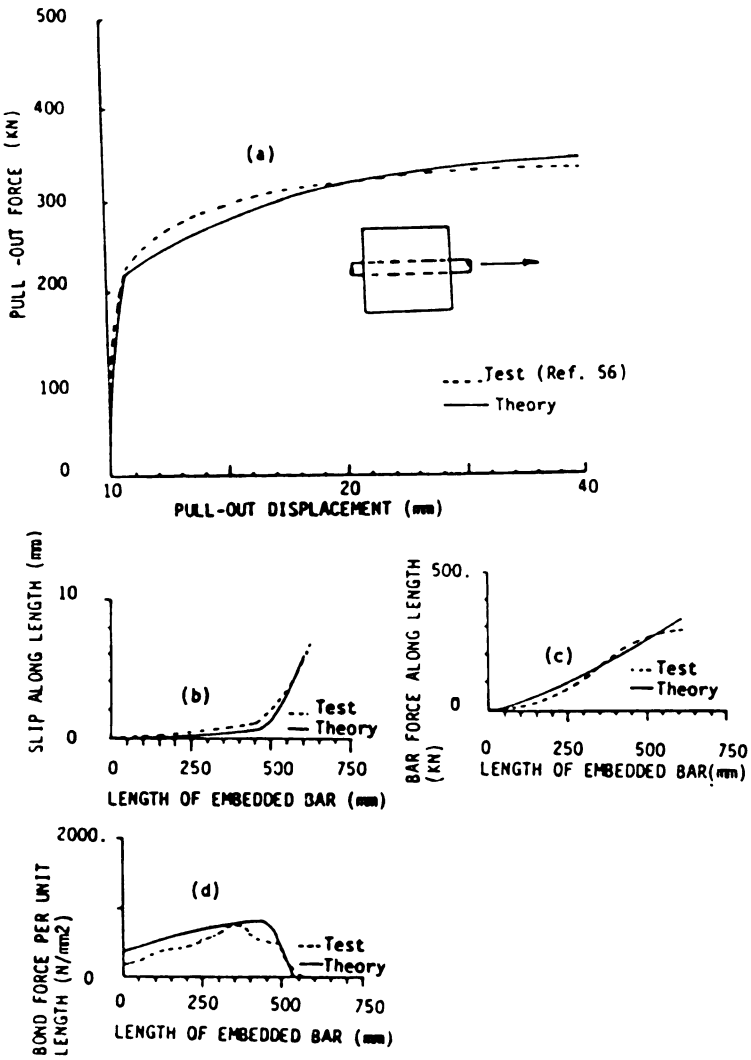


Figure 5.11: Comparison of Experimental and Theoretical Results For the Specimen Pulled at One End Only: (a) End Force-End Slip Relationship @ 6.0 mm Slip; (b) Slip Along the Anchorage Length @ 6.0 mm Slip; (c) Bar Force Along the Anchorage Length @ 6.0 mm Slip; (d) Bond Force Per Unit Length Along the Anchorage Length @ 6.0 mm Slip. ( 1 mm = 0.0394 in.; 1 N/mm² = 6.9 ksi; 1 KN = 2.28 kips).

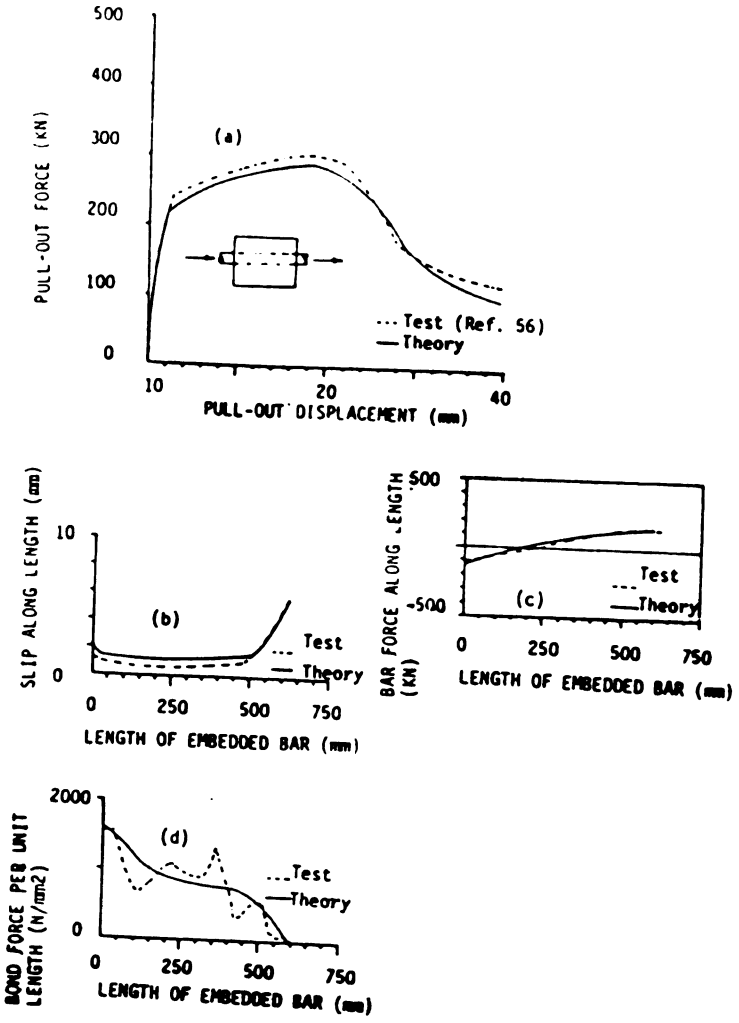


**Figure 5.12: Comparison of Experimental and Theoretical Results For the Specimen with Monotonic Pull-Push at the Two Ends: (a) End Force-End Slip Relationship @ 6.0 mm Slip; (b) Slip Along the Anchorage Length @ 6.0 mm Slip; (c) Bar Force Along the Anchorage Length @ 6.0 mm Slip; (d) Bond Force Per Unit Length Along the Anchorage Length @ 6.0 mm Slip. (1 mm = 0.0394 in.; 1 N/mm² = 6.9 ksi; 1 KN = 2.28 kips).**

Figures 5.13(a) compares the experimental and theoretical end force-end slip relationships for the specimens subjected to cyclic pull-push at the two ends

(with equal end forces). Figures 5.13(b), 5.13(c), and 5.13(d) present comparisons between theoretical and experimental distributions of slip, bar force, and bond force per unit length along the anchorage length of this specimen at the peak of the second cycle with an end slip value of 0.023 in (0.580 mm). for this specimen also the comparison between test and theory is reasonably well.

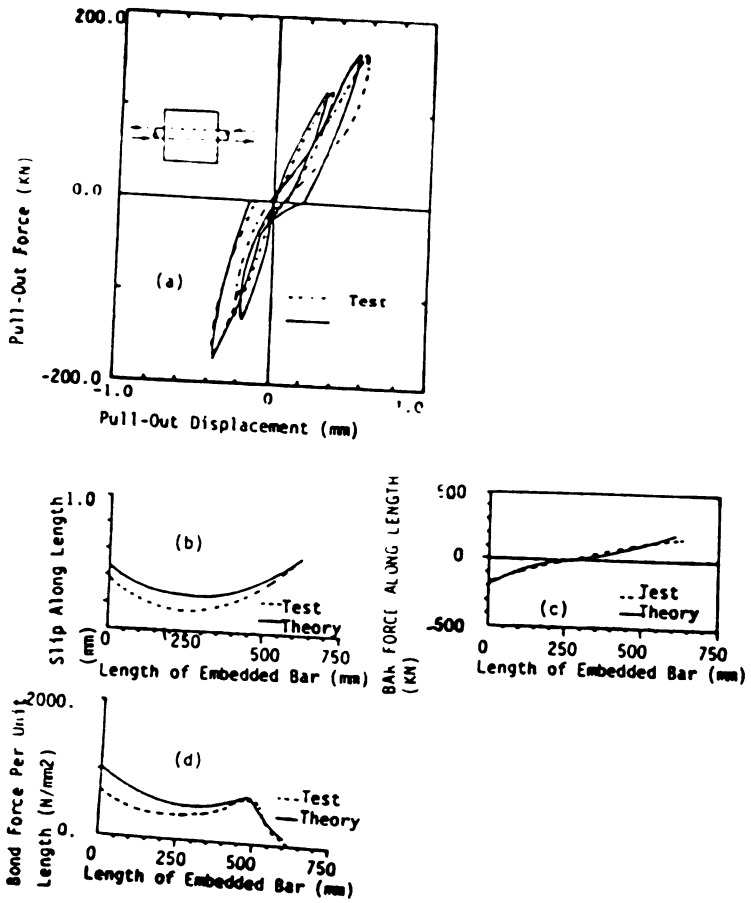


Figure 5.13: Comparison of Experimental and Theoretical Results For the Specimen Subjected to Cyclic Pull-Push at the Two Ends: (a) End Force-End Slip Relationship @ 0.1 mm Slip; (b) Slip Along the Anchorage Length @ 0.1 mm Slip; (c) Bar Force Along the Anchorage Length @ 0.1 mm Slip; (d) Bond Force Per Unit Length Along the Anchorage Length @ 0.1 mm Slip. (1 mm = 0.0394 in.; 1 N/mm$^2$ = 6.9 ksi; 1 KN = 2.28 kips).

## 5-5 RESULTS OF PARAMETRIC STUDIES WITH THE PROPOSED EMBEDDED BAR MODEL

Effects of variations in bar dimeter and yield strength, concrete compressive strength and column axial pressure on the computed response of anchored bars subjected to equal push and pull forces at two ends are presented in the following. Loading rate effects of pull-out behavior of anchored bars pulled at one end are also discussed. For the purposed of this parametric study, a basic specimen similar to the one shown in Figure 5.10 was chosen. The basic values used for bar diameter, concrete compressive strength, bar yield strength, and column pressure were 1 in (25 mm), 4,350 psi (30 $N/mm^2$), 65,000 psi (450 $N/mm^2$), and 0, respectively. Unless mentioned otherwise, these basic values are the ones chosen in the following discussion.

5-5.1 Effect of Bar Diameter: Figure 5.14(a) shows pull-out force-displacement relationships for embedded bars with different bar diameters. It can be seen in this figure that with decrease in bar diameter, the pull-out strength decreases but better pull-out behavior at large slip values is obtained. The inferior ductility of larger bars can be illustrated through comparison of bar slip distribution along its embedded length (at an end pull-out displacement of 0.236 in or 6.0 mm) shown in Figure 5.14(b). This figure shows that as the bar diameter (and consequently the strength and stiffness) of the bar increases, distribution

of slip along the bar length tends to be more uniform. This means that larger bars are less stressed along their embedment length and thus tend to pull out from concrete like a rigid rod. In this condition, the pull-out displacement consists more of bond slip and less of bar stretching. The fact that bond behavior is not as ductile as steel stretching behavior illustrates the inferior behavior at large displacements of bars with larger diameter.

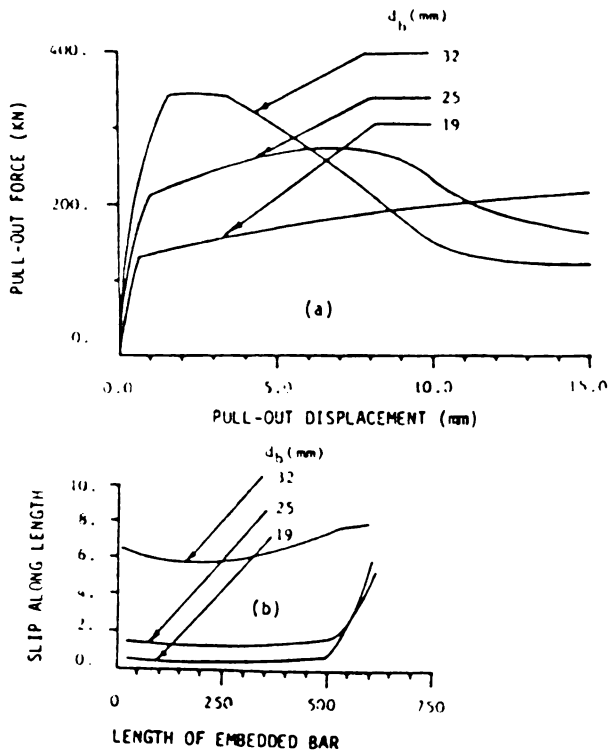


Figure 5.14: Effects of Bar Diameter On Pull-Out Behavior:
(a) Pull-Out Force-Displacement Relationship;
(b) Bond Slip Distribution
(1 mm = 0.0394 in.; 1 N/mm$^2$ = 6.9 ksi;
1 KN = 2.28 kips).

5-5.2 Effect of Concrete Compressive Strength: Comparison of pull-out force-displacement relationships in Figure 5.15(a) as well as slip distribution along the embedded length of bars [at a pull-out displacement of 0.236 in (6.0 mm)] in Figure 5.15(b) indicate that the improvement in pull-out behavior with increase in concrete compressive strength is not significant.

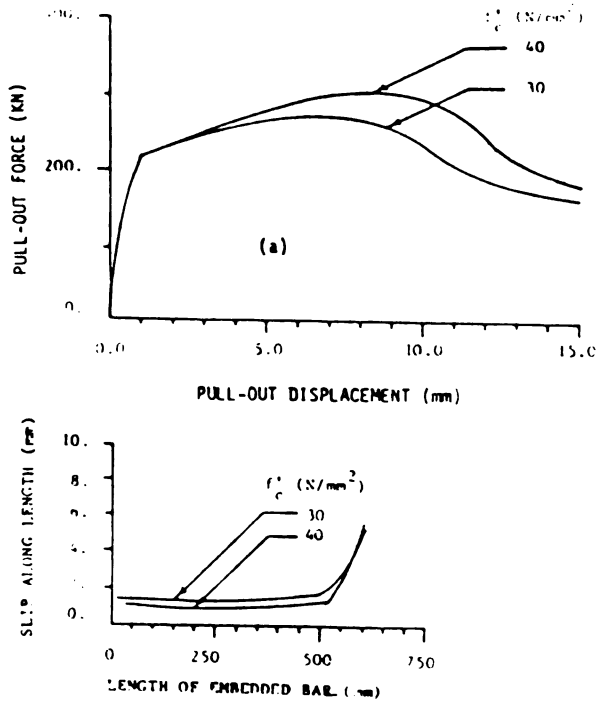


Figure 5.15: Effects of Concrete Strength On Pull-Out Behavior: (a) Pull-Out Force-Displacement Relationship; (b) Bond Slip Distribution (1 mm = 0.0394 in.; 1 N/mm² = 6.9 ksi; 1 KN = 2.28 kips).

5-5.3 Effect of Bar Yield Strength:

Increase in bar yield strength is shown in Figure 5.16(b) to increase the pull-out strength of the anchored bar, but does not damage its ductility. This can be illustrated (like the effect of bar diameter) by the more uniform distribution of slip along the embedment length of higher strength bars shown in Figure 5.16(b).

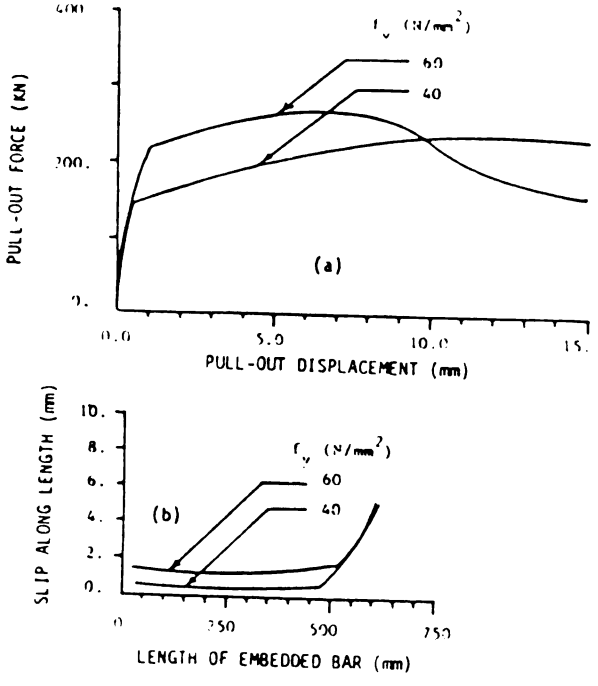


Figure 5.16: Effects of Bar Yield Strength On Pull-Out Behavior: (a) Pull-Out Force-Displacement Relationship; (b) Bond Slip Distribution. (1 mm = 0.0394 in.; 1 N/mm² = 6.9 ksi; 1 KN = 2.28 kips).

5-5.4 Effect of Column Pressure: Increase in column pressure is shown in Figure 5.17(a) and 5.17(b) to result in a slight improvement of the pull-out behavior. This improvement, however, does not seem to have any practical significance.

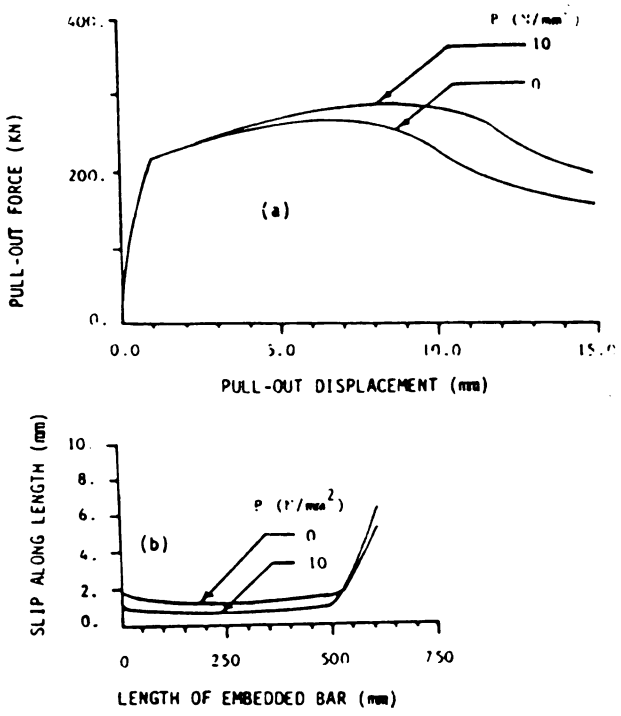


Figure 5.17: Effects of Column Pressure On Pull-Out Behavior: (a) Pull-Out Force-Displacement Relationship; (b) Bond Slip Distribution. (1 mm = 0.0394 in.; 1 N/mm² = 6.9 ksi; 1 KN = 2.28 kips).

5-5.5 Effect of Loading Rate: The behavior of anchored bars apart from their dependency on the mechanical properties of steel and the bond between steel and concrete, are also sensitive to variations in the rate of loading.[19,49(a)] Consequently, the anchored bar behavior under high earthquake-induced loading rates is expected to be different from the behavior under quasi-static loads. This difference might influence the current anchorage design requirements that are based on quasi-static test results.

The particular study reported in this section utilizes the available test data on loading rate-sensitivity of steel and bond constitutive laws for analyzing the loading rate-sensitivity of the anchored bar behavior. Loading rate effects on the bond constitutive behavior were discussed earlier in section 3.2. The steel strain rate-sensitive constitutive model used in this study has been developed in Ref. 49(a):

$$f_s = \begin{cases} E_s \cdot \epsilon_s & \text{for } \epsilon_s < f_y'/E_s \\ f_y' + E_h'(\epsilon_s - f_y'/E_s) & \text{for } f_y'/E_s < \epsilon_s < \epsilon_u' \\ 0 & \end{cases} \qquad (5\text{-}13)$$

where: $f_s$ = steel stress;

$\epsilon_s$ = steel strain;

$E_s$ = steel elastic modulus;

$f_y'$ = dynamic yield strength of steel

$= f_y.[(-4.51\times10^{-6} f_y + 1.46) + (-9.20\times10^{-7} f_y + 0.927)\log_{10}\dot{\epsilon}\,]$;

$f_y$ = quasi-static yield strength of steel (psi);

= strain rate (1/sec);

$E_h'$ = dynamic strain hardening modulus of steel

$= E_h.[2x10^{-5}f_y + 0.077$

$+ (4x10^{-6}f_y - 0.185)\log_{10}\dot{\epsilon}\ ] < E_h$;

$E_h$ = quasi-static strain hardening modulus of steel;

$\epsilon_u'$ = dynamic ultimate strain of steel

$= \epsilon_u.[(-8.93x10^{-6}f_y + 1.4)$

$+ (-1.79x10^{-6}f_y + 0.0827)\log_{10}\dot{\epsilon}\ ]$;

$\epsilon_u$ = quasi-static ultimate strain of steel.

Figure 5.18 presents a typical comparison of the steel constitutive model with test results.

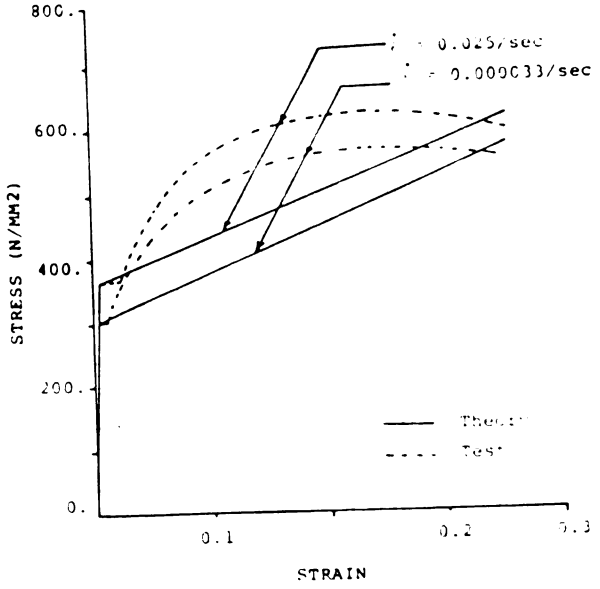


Figure 5.18: Strain Rate-Sensitivity Steel Model [Ref. 49(a)]

The steel and bond loading rate-sensitive constitutive laws together with the proposed model of embedded bars were

used to study the loading rate effects on anchored bars similar to the one shown in Figure 5.19 (pull from one side only) in which a #8 deformed bar with yield strength of 65,000 psi (450 MPa) is embedded in confined concrete with a compressive strength of 4,350 psi (30 MPa), and is subjected to a monotonic pull at one end. Figure 5.20(a) presents loading rate effects on the end force-slip relationship of this anchored bar. The end slip rates used in producing Figure 5.20(a) ranged from $5x1^{-5}$ in/sec. ($2x10^{-5}$ mm/sec), that corresponds to quasi-static loading conditions, to 0.5 in/sec (0.02 mm/sec), that is a typical rate expected under seismic loads. From Figure 5.20(a) it can be concluded that with increasing slip rate, the anchored bar resistance against pull-out increases, but its stiffness remains practically unchanged. The load at which large inelastic pull-out of the anchored bar initiates (from now on this is refered to as the anchorage yield load) increases by 8.6% in Figure 5.20(a) as the loading rate increases from the quasi-static level to the values expected under earthquakes. During analysis, the steel strain rate was also computed at the point of load application. Using the steel strain rate- sensitive model, it was found that the steel yield strength just outside the anchored bar region increased by 12% as the quasi-static rate was increased to rate expected under earthquakes. This shows that the increase in anchorage yield strength with increasing loading rate cannot match the corresponding

increase in bar yield strength. Consequently, if an anchorage is designed to remain elastic before bar yielding under quasi-static loads, its yield might undesirably precede bar yielding under dynamic loads.

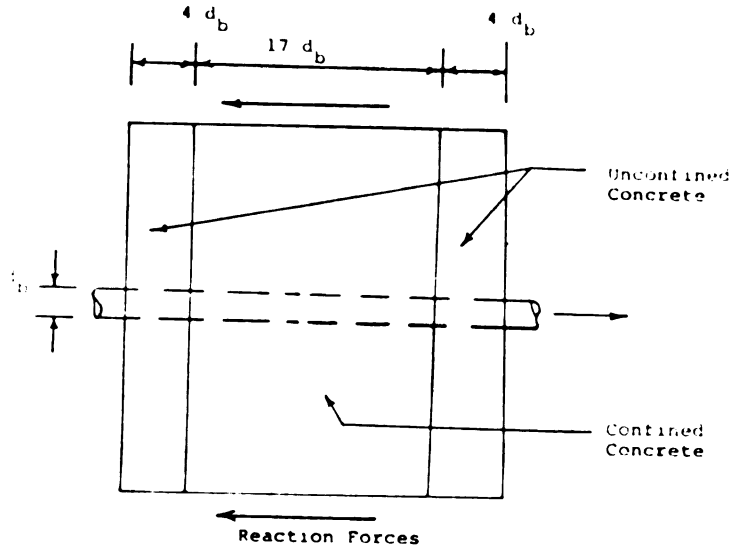


Figure 5.19: Test Specimen (Pull From One Side Only Used In Studying Rate of Loading.

The same undesirable effects of loading rate increase can be seen in Figures 5.20(b) and 5.20(c) for specimens that simulate the one used for deriving Figure 5.20(a) [see Figure 5.19(a)] with the same bar yield and concrete compressive strengths but different bar diameters. For #6 bar [Figure 5.20(b)] the anchorage yield strength increased by 3.5% that is considerably lower than the 12.1% increase in bar yield strength as the loading rate was increased from quasi-static to the seismic level. The corresponding

increases in anchorage and bar yield strengths of #10 bar were 9.2% and 13.2%, respectively.

The effects of concrete compressive strength on anchored bar strain rate-sensitivity are studied in Figures 5.20(d) and 5.20(e). In Figure 5.20(d) with a low-strength concrete ($f_c'$ = 2.9 ksi or 20 MPa), the anchorage yield strength increased by 10.3% compared to 13.1% increase in the bar yield stength with loading rate increasing from a quasi-static level to that expected under earthquake earthquakes. The corresponding increases in anchorage and bar yield strengths for the high strength concrete ($f_c'$ = 7.25ksi or 50.0MPa) in Figure 5.20(e) are observed to be 11.8% and 13.1% respectively. Hence, the effects of increasing loading rates are still undesirable, and irrespective of concrete compressive strength, the increase in the anchorage yield strength at higher loading rates is less than the corresponding increase in bar yield strength. In Figures 5.20(b) through 5.20(e) the anchorage stiffness can be seen to remain insensitive to loading rate variations for diffeerent bar diameters and concrete compressive strengths.

The effect of bar yield strength on anchorage loading rate-sensitivity are studied in Figures 5.20(f) and 5.20(g). the specimens for these figures were similar to the one used for producing Figure 5.20(a) except for the bar yield strength. It should be noticed that the strain rate-sensitivity of bar yield strength is stronger for

lower strength concrete.[4,7,8] The anchorage yield strength for the low-strength steel bar ($f_y$ = 43.5 ksi or 300 MPa) in Figure 5.20(f) increased by 17.4% that was still lower than the corresponding increase of bar yield strength (21.3%). Hence, for low-strength steel too, the increase in loading rate produces undesirable effects. For the high-strength steel bar ($f_y$ = 87.0Ksi or 600 MPa) in Figure 5.20(g), however, the increase in anchorage yield strength (6.8%) was higher than the corresponding increase in bar yield strength (5.4% as the loading rate increased from the quasi-static level to the level typically expected under earthquakes. Hence, for a very high-strength steel, the increase in loading rate has a desirable effect and increases the safety against possibility of bar pull out before steel yielding. At different bar yield strengths also, the anchorage stiffness is not loading rate-sensitive.

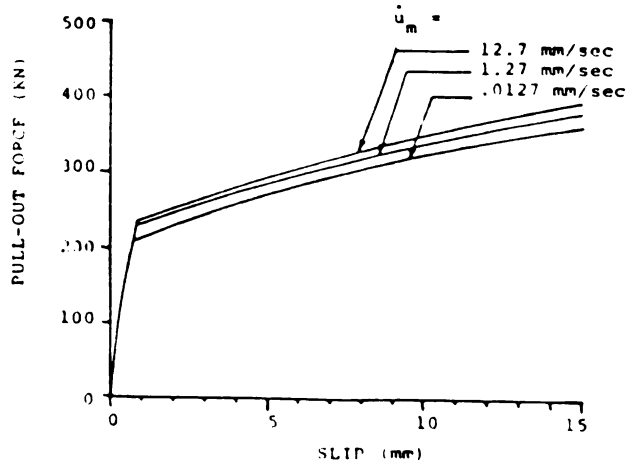


(a) $d_b$=25.4 mm, $f_y$ = 450 MPa, $f'_c$=30 MPa

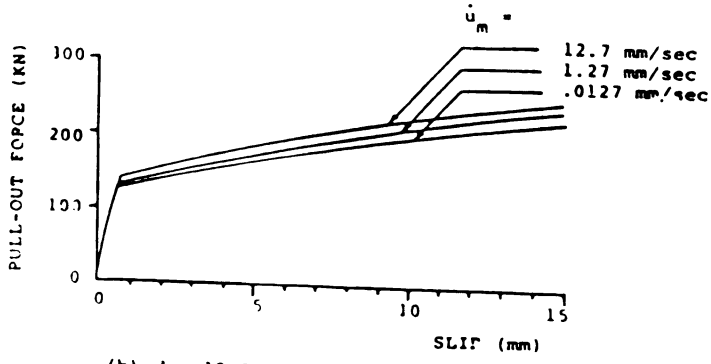


(b) $d_b$ = 19.0 mm, $f_y$=450 MPa, $f'_c$ = 30 MPa

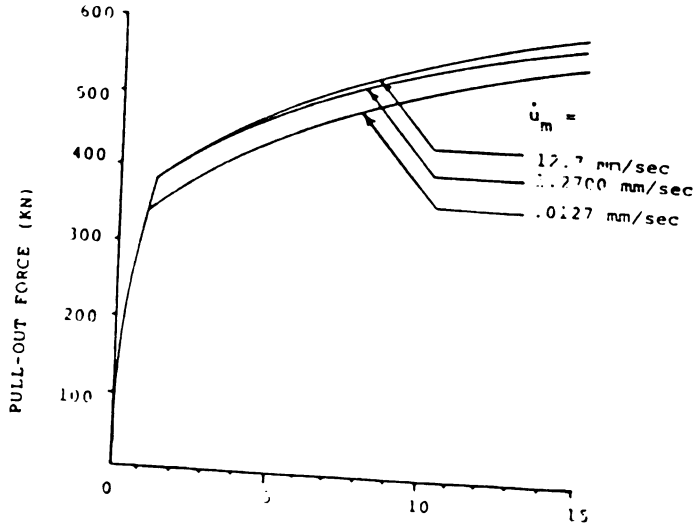


(c) $d_b$=32.0 mm, $f_y$= 450 MPa, $f'_c$ = 30 MPa

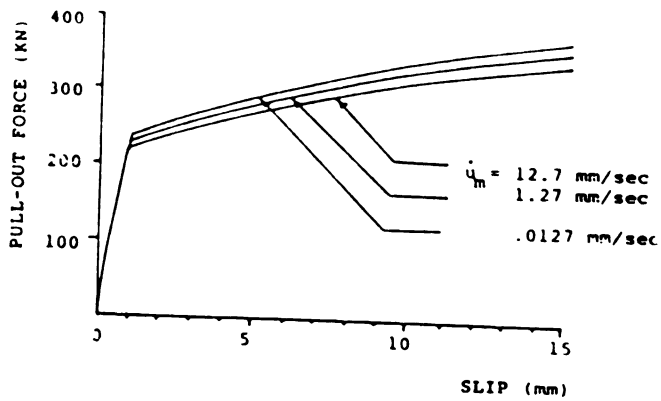


(d) $d_b$=25.4 mm, $f_y$= 450 MPa, $f'_c$ = 20 MPa

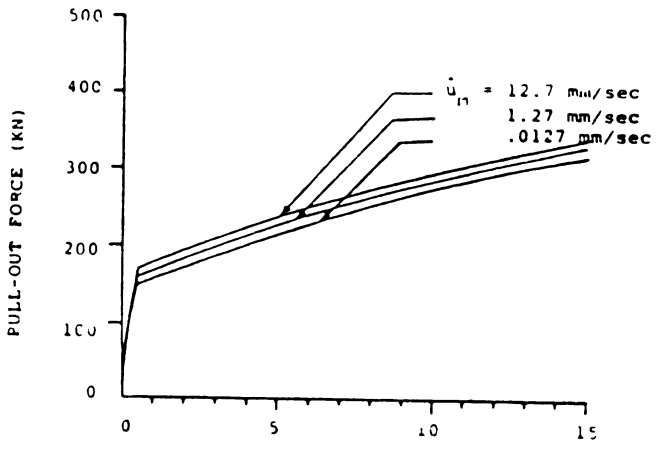


(f) $d_b$=25.4 mm, $f_y$=300MPa, $f'_c$ = 30 MPa

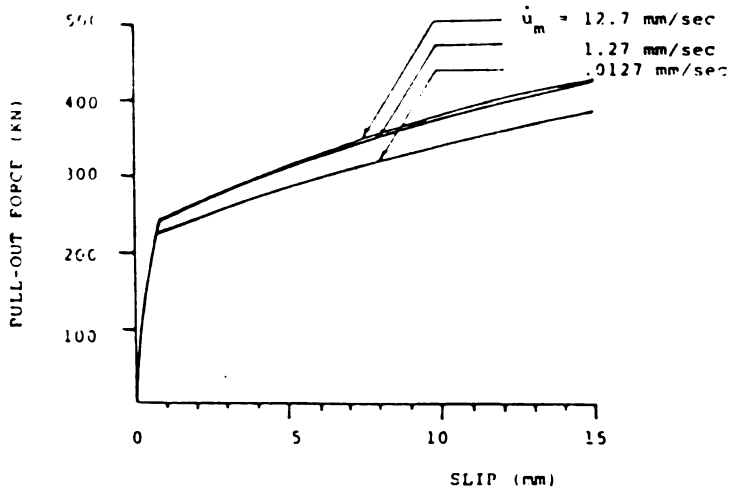


(e) $d_b$=25.4 mm, $f_y$= 450 MPa, $f'_c$ =50 MPa

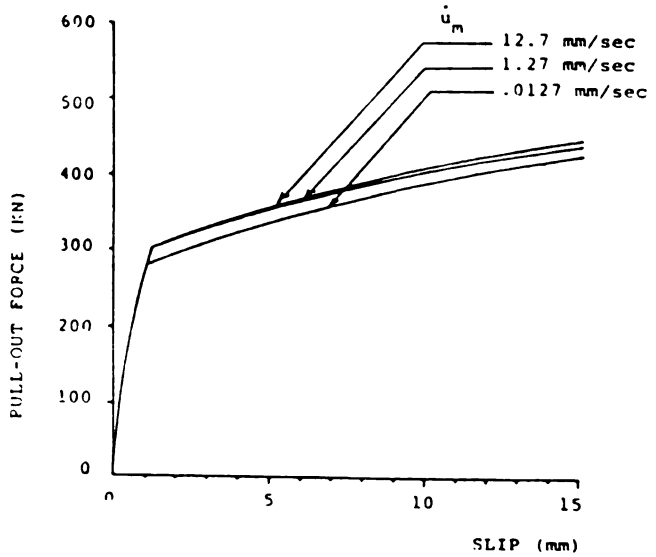


(g) $d_b$=25.4 mm, $f_y$=600 MPa, $f'_c$=30 MPa

Figure 5.20: Loading Rate Effects On End Force-End Slip Relationship of Anchored Bars. (1 in. = 25.4 mm; 1 ksi = 0.0069 MPa; 1 kip = 0.445 KN)

# CHAPTER 6

# PULL-OUT BEHAVIOR OF BEAM LONGITUDINAL BARS HOOKED IN BEAM-COLUMN CONNECTIONS

## 6-1 INTRODUCTION

Longitudinal bars of reinforced concrete beams are generally anchored in the exterior beam-column connections by 90° hooks [Figure 6.1(a)]. these hooks resist pull-out forces, and prevent large fixed-end rotations that can contribute significantly to the overall beam deflections [Figure 6.1(b)].[23] It is thus important to assess the behavior of hooked bars under pull-out forces in order to predict the beam fixed-end rotations.

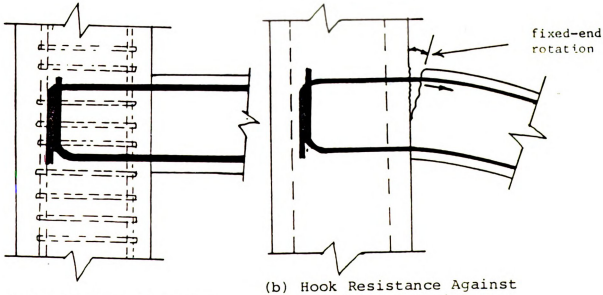


Figure 6.1: Behavior of Exterior R/C Connections Under Beam End-Moment.

The resistance of hooked bars against pull-out is provided by the bond between steel and concrete along the straight embedded length of the bar, and by the hook itself (Figure 6.2).[1] Bond between deformed bars and concrete has been studied rather extensively,[1,11,19,23,44,53,56] while the reported studies on hook behavior are scarce.[37(a),38(c),44] The present work is an experimental study on the behavior of 90° standard hooks embedded in confined concrete specimens (that simulate the exterior beam-column connections) under the action of monotonic pull-out forces.

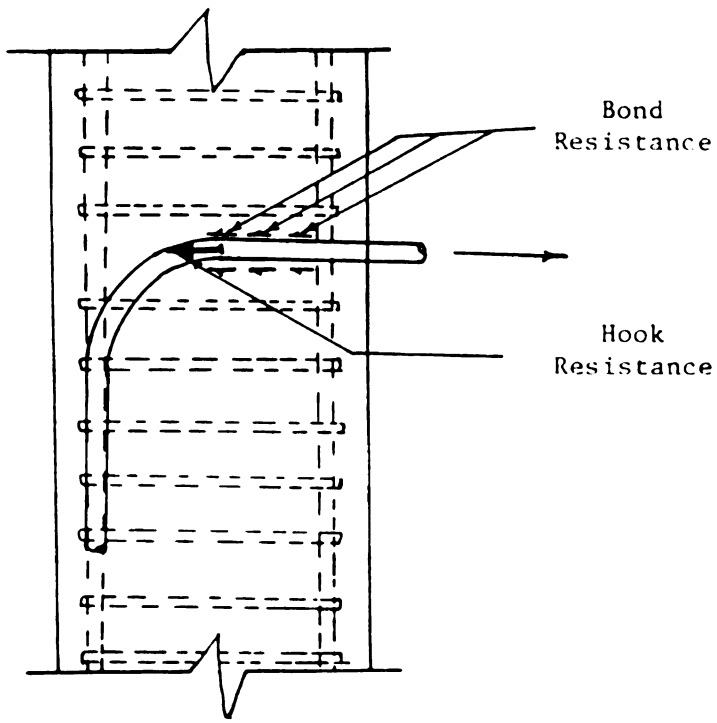


Figure 6.2: Resistance of Hooked Bars Against Pull-Out Forces.

## 6-2 BACKGROUND

The available test data on hook behavior are very limited. Refs. 20, 37(a), and 38(c) have reported some test results on specimens shown in Figures 6.3(a), 6.3(b), and 6.3(c), respectively. From test data reported in Ref. 38(c) it can be concluded that for hooks embedded in plain concrete specimens (Figure 6.3), an increase in the angle of bend reduces the hook pull-out stiffness, but does not change the pull-out strength.

The full-scale exterior beam-column joints tested in Ref. 37(a) [Figure 6.3(b)] failed suddenly with entire side of the column face spalling. Increase in concrete cover thickness normal to the hook plane increased the ductility of hooked bars subjected to pull-out forces. Confinement of concrete surrounding the hook was also found to improve the behavior of #11 hooked bars, but did not significantly influence the performance of #7 hooked bars. Test results reported in Ref. 37(a) showed no effect of column axial load or angle of hook bent on the overall hook behavior.

Ref. 20 has summarized results of a limited number of tests on single #8 hooked bars embedded in confined concrete specimens that simulated exterior beam-column connections [Figure 6.3(c)]. An empirical constitutive model was developed for 90° standard hooks in Ref. 20, which will be presented later.

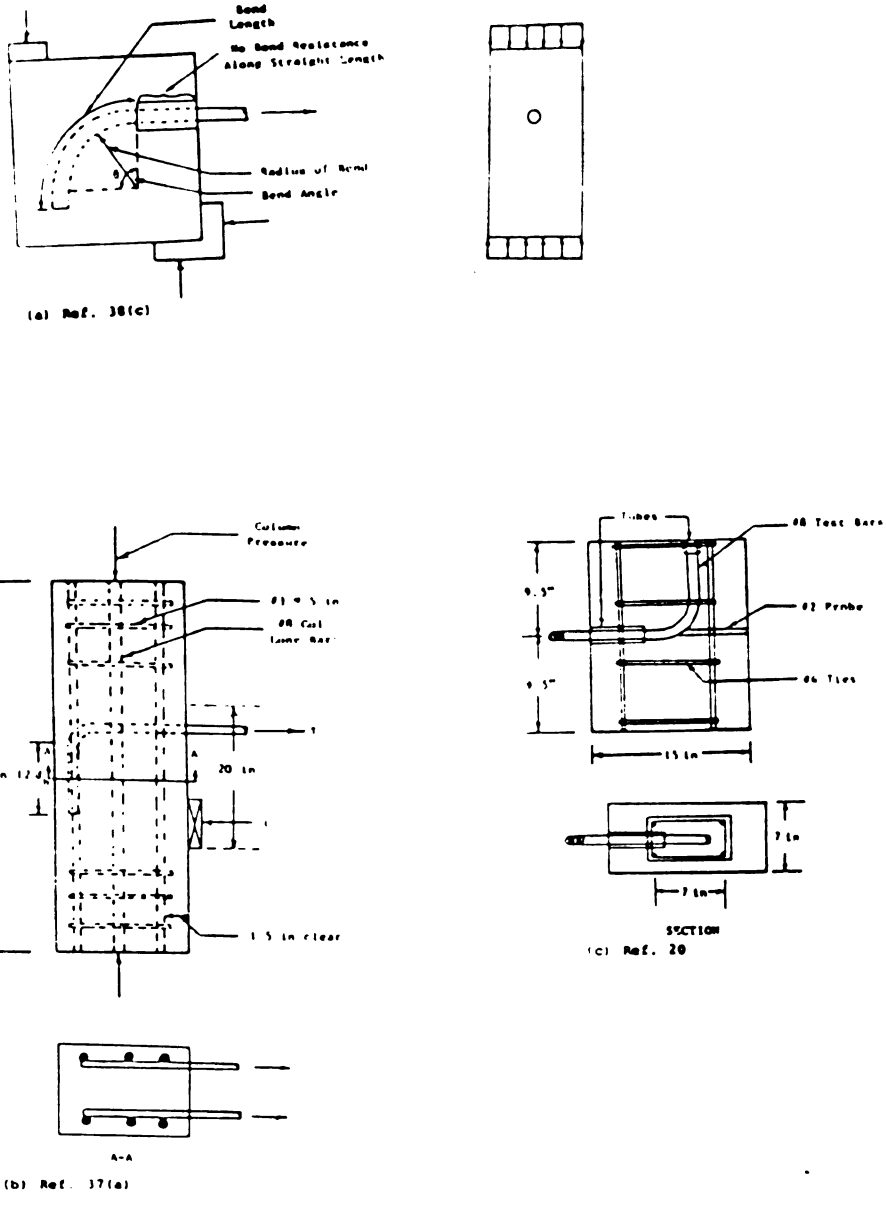


Figure 6.3: Hook Test Specimens [Refs. 20, 37(a), 37(c)].

## 6-3 Test Program

The specimen tested in this study (Figure 6.4) simulate the behavior of hook inside an exterior beam-column connection. The connection was confined according to the ACI code[1] requirements for R/C frames located in high seismic risk zones. The straight embedded length of bar was covered with a plastic tube. This eliminated the bond resistance, and left the 90° standard hook to provide the pull-out resistance. The compression zone of the beam was duplicated in these tests with a steel plate bearing against column face.

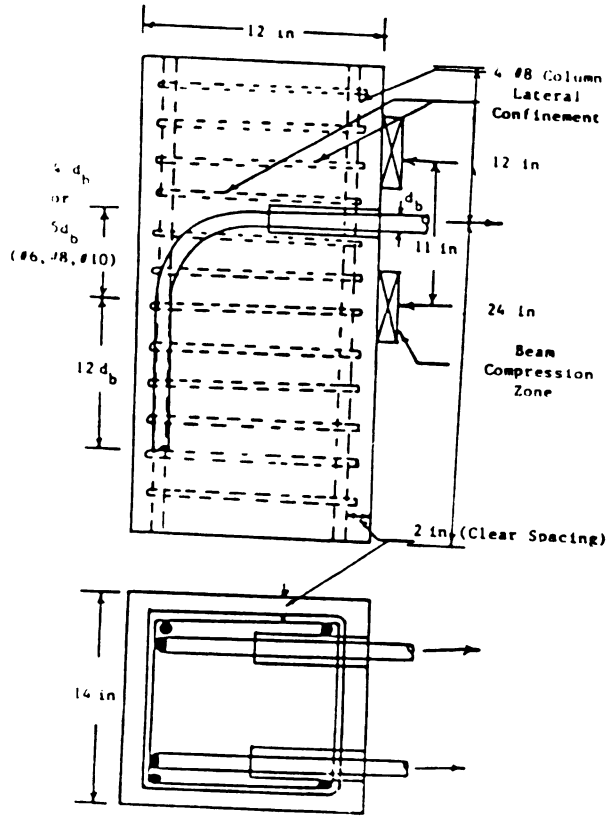


Figure 6.4: Hook Test Specimen (used in this Study).

Concrete was cast vertically in the direction of hook bent. A plastic sheet was placed horizontally at the level of anchored bars in concrete cover in order to artificially produce the radial cracks that could occur under pull-out forces if the bond between straight segment of the bar and concrete was not eliminated. Type IA Portland cement, and aggregate with a maximum size of 3/4 in. (19.1 mm) were used in the mix. The specimens were cured in moist room for seven days before their wood forms were removed. They were then kept in moist room for another seven days after which they were exposed to the uncontrolled lab environment. The specimens were tested at the age of 30 $\pm$ 2 days. All the steel bars used in reinforcing the specimens were grade 60, and their actual yield strength obtained from tensile tests was about 70 ksi (480 MPa).

The seven specimens tested in this study had the same general geometry (Figure 6.4), but the hooked bar size, confinement, and concrete strength varied in different specimens are discussed below:

a) Anchored bars were #6, #8, and #10;

b) confinement was provided by #3 ties spaced at 3 in. (76.2 mm) or 4 in. (101.6 mm), or #4 ties spaced at 3 in (76.2 mm) center to center;

c) the concrete compressive strength were either 3,780 psi (26.1 MPa) or 6,050 psi (41.7 MPa).

Table 6-1: summarizes the properties of the seven specimens tested in this study.

Table 6-1: Properties of Test Specimens on Hook

| | Specimen | Bar Size | Lateral Confinement | Concrete Compressive Strength (psi) |
|---|---|---|---|---|
| 1 | Standard | #8 | #3 @ 3" | 3780 |
| 2 | Standard | #8 | #3 @ 3" | 3780 |
| 3 | Low Confinement | #8 | #3 @ 4" | 3780 |
| 4 | High Confinement | #8 | #4 @ 3" | 3780 |
| 5 | High Concrete Strength | #8 | #3 @ 3" | 6050 |
| 6 | Small Hooked Bars | #6 | #3 @ 3" | 3780 |
| 7 | Large Hooked Bars | #10 | #3 @ 3" | 3780 |

The test setup is shown in Figure 6.5. Two hydraulic actuators bearing on concrete column applied quasi-static pull-out force on the hooked bars. The load was measured by a load cell located midway between the two bars. Four electrical displacement transducers (two for each bar) were used to measure pull-out displacements at a point on anchored bars 4 in. (101.6 mm) above the column face. The hook pull-out (at point A in Figure 6.5) was obtained by subtracting the extension of anchored bar between point A and the point to which transducers were fixed from the

average measurements of the two transducers (bar extensions were measured in seperate tension tests). The tests were discontinued after excessive cracking of specimens and large pull-out displacements.

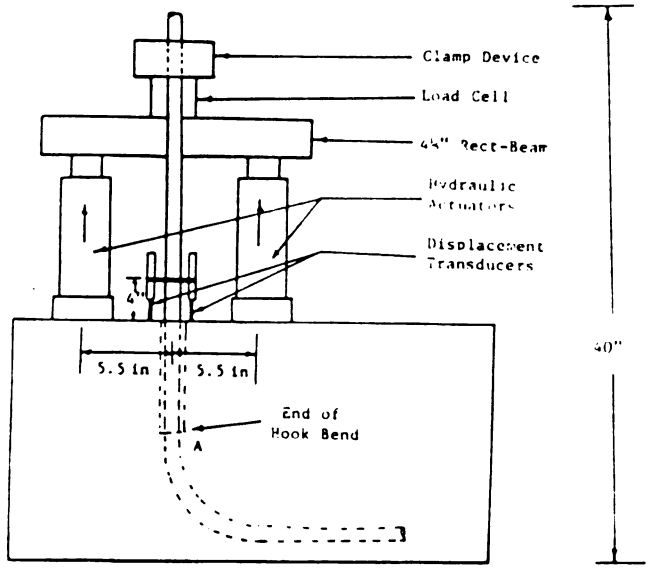


Figure 6.5: Test Set-Up Used In This Study.

## 6-4 Test Results

The crack pattern and general behavior of all specimens were similar. At about half the ultimate load, the crack that was artificially produced by placing plastic sheets in specimens started to grow and extended along the hook [Figure 6.6(a)]. Radial cracks normal to the direction of artificially produced cracks appeared later in the loading history [Figure 6.6(b)]. Near ultimate load, the specimens had a clear tendency to expand in the direction normal to

the hook plane. This resulted in spalling of concrete cover [Figures 6.6(c) and 6.6(d)]. This tendency to expand can be illustrated by the fact that pull-out forces produce large compressive stresses inside the hook bend [Figure 6.7][38(c)], and with the increasing poisson's ratio of concrete under high compressive stresses, concrete tends to expand laterally and push against the ties and the cover.

Figures 6.8(a) through 6.8(g) show pull-out force versus hook pull-out displacement relationships for the seven specimens tested in this study. The curves in this figures represent the average behavior of the two hooks in each specimen. These two hooks behaved almost identically under pull-out forces.

From test results presented in Figure 6.8 it can be concluded that: (a) with increasing bar diameter, the hook ultimate pull-out force as well as its pull-out resistance at large displacements increase considerably [see Figure 6.9(a)]. This increase is, however, smaller than the increase in bar yield strength; (b) the hook pull-out resistance also increase with increasing confinement [Figure 6.9(b)]; (c) the higher concrete strength used in specimen 5 did not significantly improve the hook behavior, but more test data are needed before a final conclusion can be made in this regard.

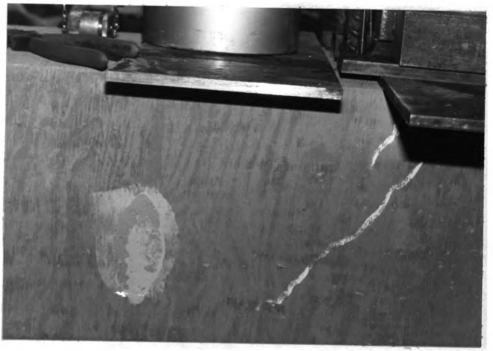

(a) Cracking Along Hook.

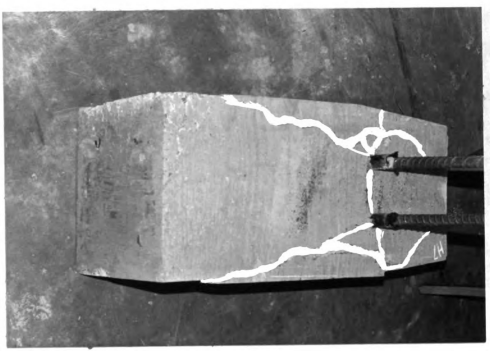

(b) Radial Cracks Normal to Direction of Artificially Produced Cracks.

(c) Spalling of Concrete Cover.

(d) Total Spalling of Concrete Cover.

Figure 6.6: Cracking of Specimen Under Gradual Increasing Load.

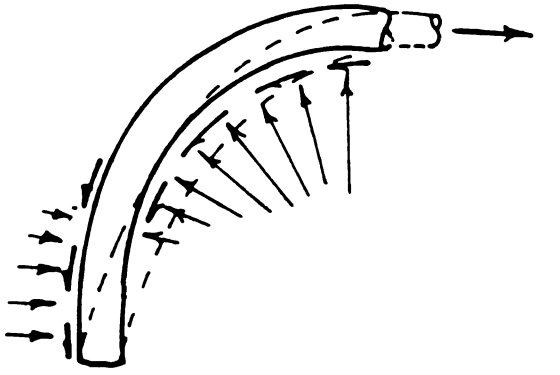

Figure 6.7: Compressive Stresses Inside the Hook Bent.

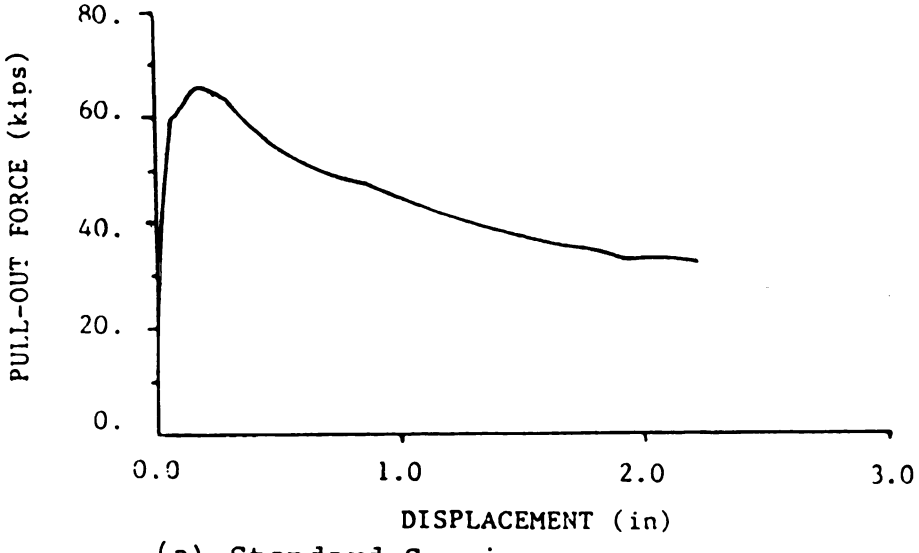


(a) Standard Specimen (1)

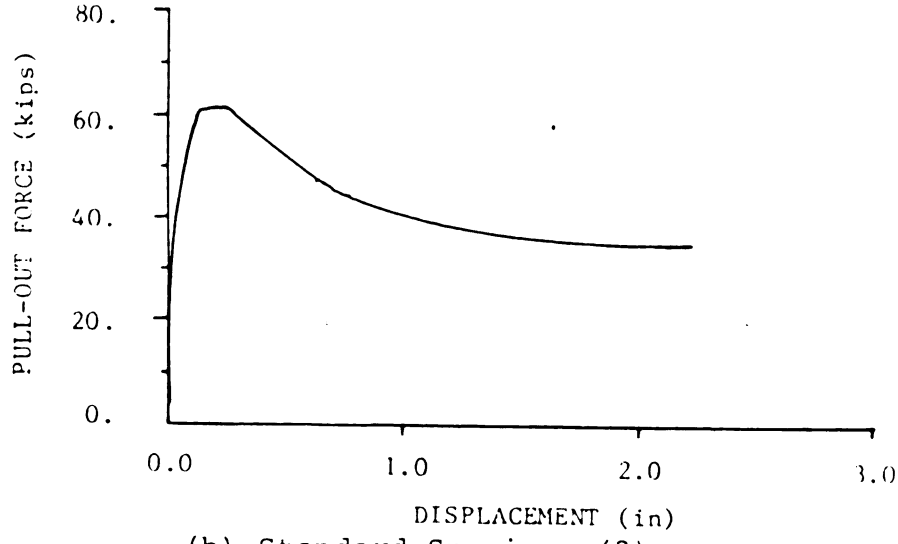


(b) Standard Specimen (2)

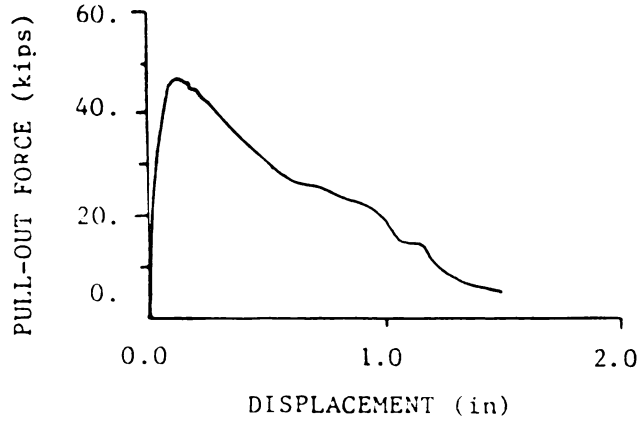


(c) Low Confinement Specimen (3)

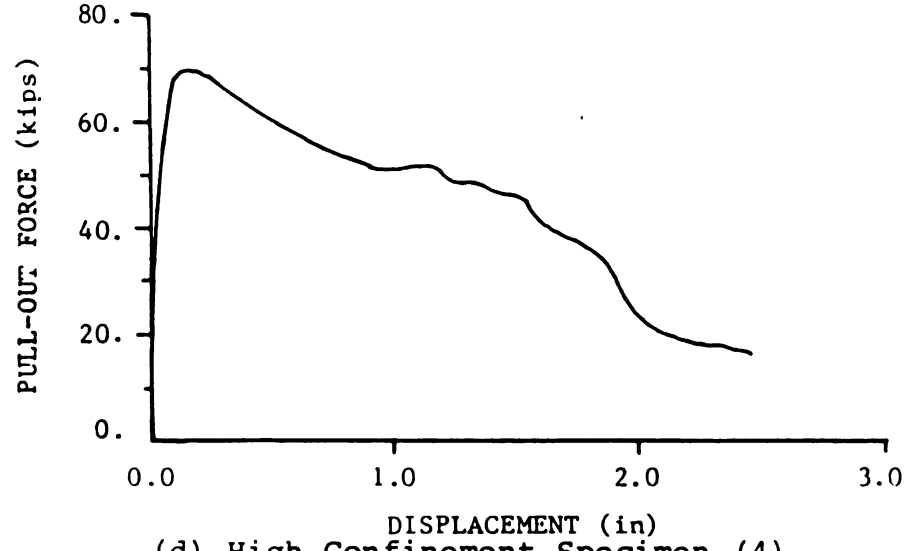


(d) High Confinement Specimen (4)

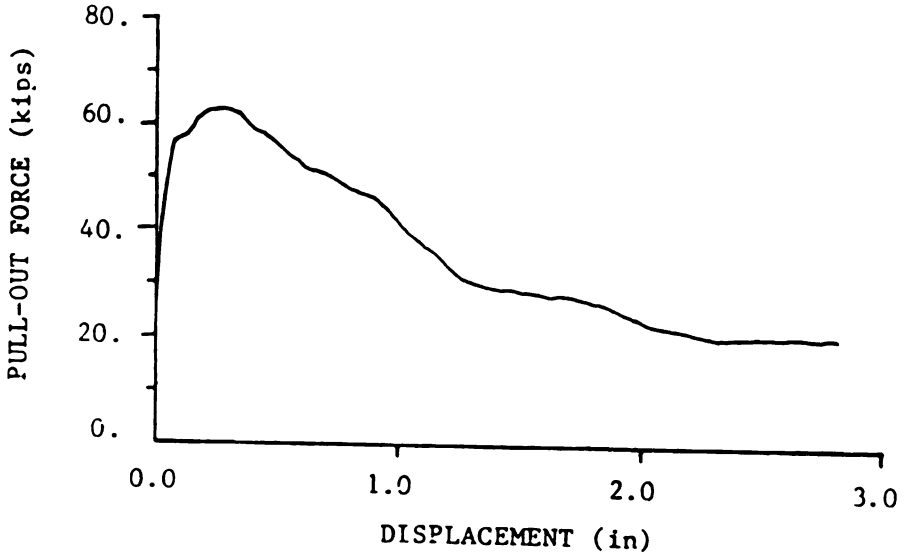


(e) High Strength Specimen (5)

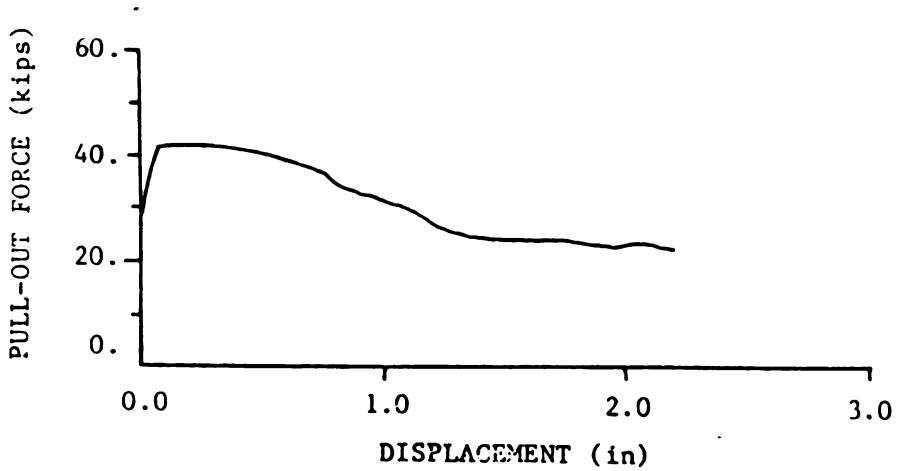


(f) Small Bar Specimen (6)

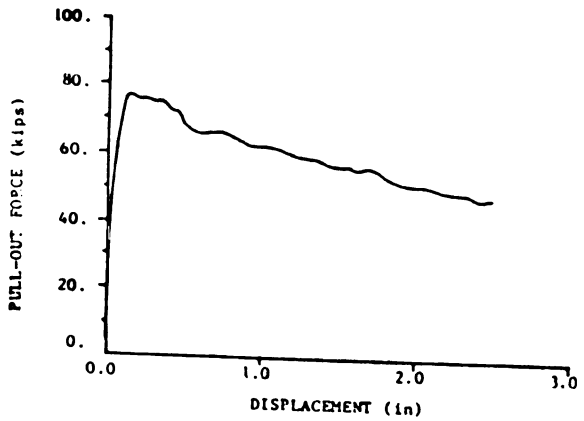


(g) Large Bar Specimen (7)

**Figure 6.8: Experimental Pull-Out Force-Displacement Relationships. (1 in. = 25.4 mm; 1 kip = 0.445 KN).**

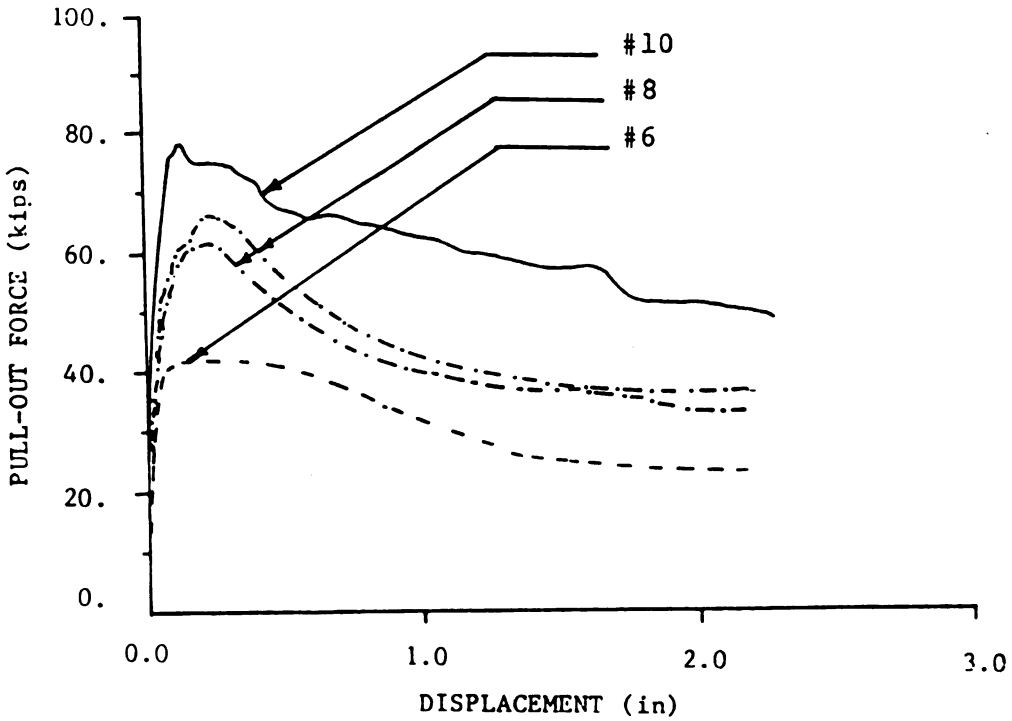


(a) Effect of Bar Size

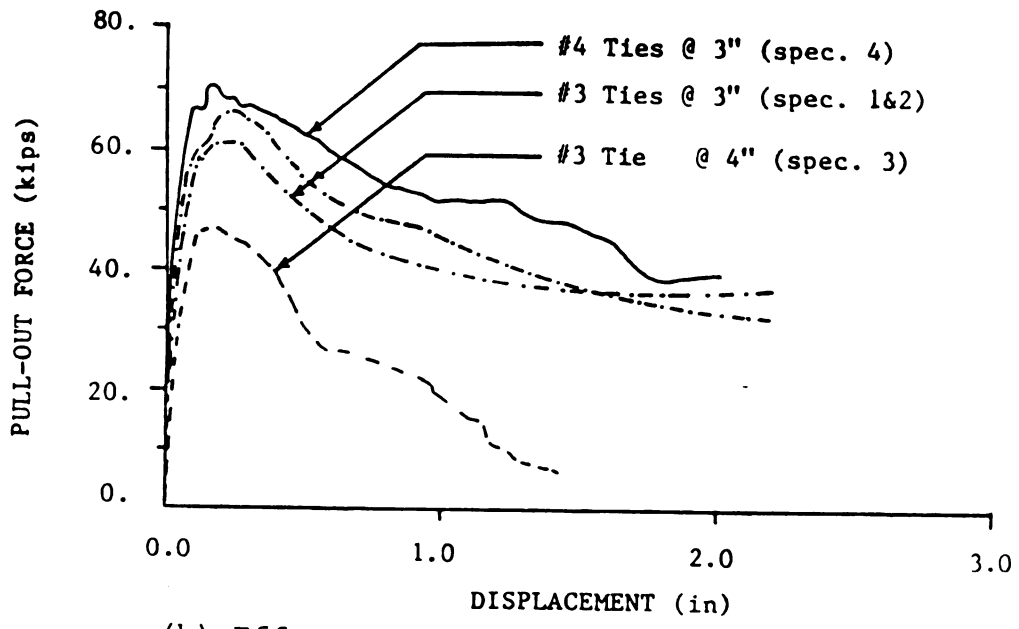


(b) Effect of Confinement

**Figure 6.9: Factors Influencing the Hook Behavior. (1 in. = 25.4 mm; 1 kip = 0.445 KN).**

## 6-5 EMPIRICAL FORMULATIONS

The following equations (Figure 6.10)[20] were chosen to represent the relationship between the hook pull-out force (P) and its pull-out displacement (u)[20]:

$$P = \begin{cases} P_1 . (u/u_1)^{0.2} & \text{for } u \leq u_1 \\ P_1 & \text{for } u_1 \leq u \leq u_2 \\ P_1 - (u-u_2)(P_1-P_3)/(u_3-u_2) > P_3 & \text{for } u > u_2 \end{cases} \quad (6\text{-}1)$$

The characteristic displacement values ($u_1$, $u_2$, and $u_3$) in the above constitutive model were derived from test results:

$u_1$ = 0.1 in. (2.5 mm)

$u_2$ = 0.3 in. (7.6 mm)

$u_3$ = 1.5 in. (38.1 mm)

Characteristics force values ($P_1$ and $P_3$) in this model were derived from results of tests on different specimens, and they are presented in Table 6-2. For well confined concrete specimens with compressive strength of about 4,000 psi (about 30 MPa), these values can be approximated by:

$P_1 = 61(1.2d_b - 0.2)$ kips (with $d_b$ in inches)

$= 27.1(0.5d_b - o.25)$ KN (with $d_b$ in mm);

$P_3 = 33(1.2d_b - 0.2)$ kips (with $d_b$ in inches)

$= 14.7(0.05d_b - 0.25)$ KN (with $d_b$ in mm);

where $d_b$ = bar diameter.

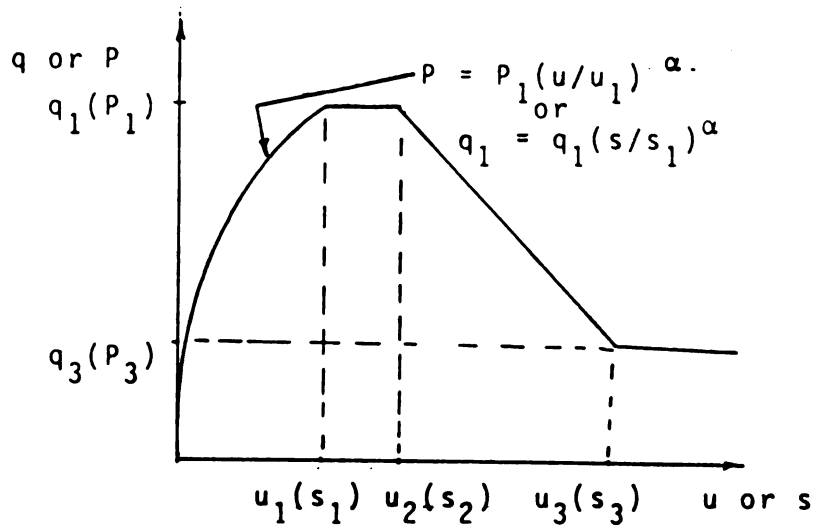


Figure 6.10: General Shape of Hook and Bond Constitutive Models.

Table 6-2: Characteristic Pull-Out Force Values In the Constitutive Model of Hooks Given In Eqn. (6-1)

| Specimen | $P_1$ (kips) | $P_3$ (kips) |
|---|---|---|
| 1 (Standard) | 64 | 34 |
| 2 (Standard) | 58 | 32 |
| 3 (Low Confinement) | 47 | 6 |
| 4 (High Confinement) | 66 | 35 |
| 5 (High Concrete Strength) | 61 | 22 |
| 6 (Small Hooked Bar) #6 | 41 | 25 |
| 7 (Large Hooked Bar) #10 | 77 | 48 |

Specimens 1 and 2 in this study were similar to the specimens tested in Ref. 20 except for the number of hooked bars which were two in this study (Figure 6.4) and one in Ref. 20 [Figure 6.3(c)]. The constitutive model that represents the behavior of hooks in the specimens of Ref. 20 is compared in Figure 6.11 with the experimentally observed behavior of hooks in specimens 1 and 2 of this study. This figure also shows the constitutive model developed in this study.

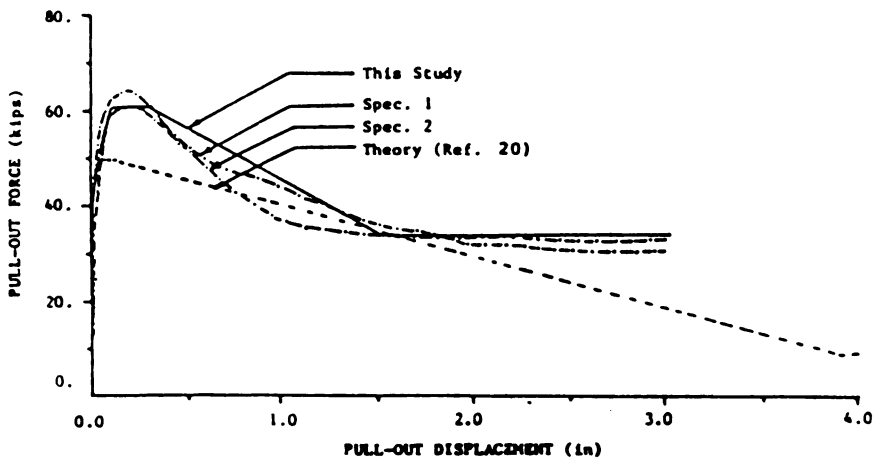


Figure 6.11: Comparison of Hook Behavior Observed in This Study With Ref. 20. (1 in. = 25.4 mm; 1 kip = 0.445 KN).

## 6-6 ANALYTICAL STUDIES ON THE HOOKED BAR BEHAVIOR

A hooked bar consists of a standard hook and a straight segment of the bar embedded in concrete. The physical model shown in Figure 6.12 was used in this study for analytical studies on the hooked bar behavior under pull-out forces. In this model, bond is simulated by springs connecting the bar to concrete along the embedded length.[44] The hook is also idealized as a single spring connecting the bar end to concrete.

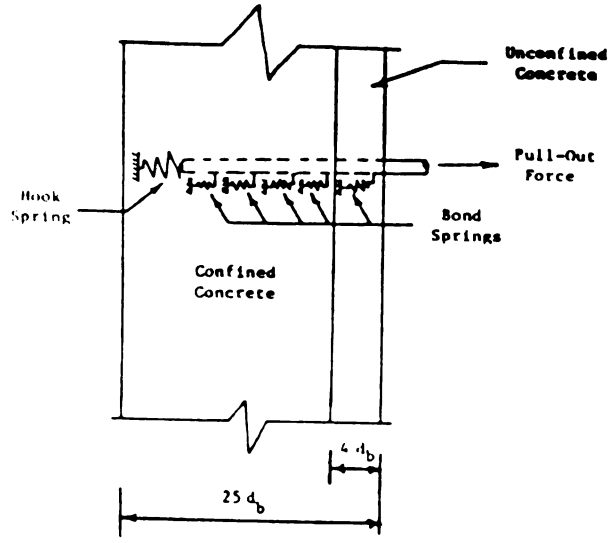


Figure 6.12: Physical Model of Hook Anchorage.

Constitutive models of the springs in Figure 6.12 as well as the steel constitutive law are needed for

constructing the tangent stiffness matrix of the anchored bar. This stiffness matrix can be used for analysis of bar pull-out behavior.

The bond constitutive model used in this study is an empirical one presented in Ref 19 (that was also presented in Chapter 5):

$$q = \begin{cases} q_1 (u/u_1)^{0.4} & \text{for } u \leq u_1 \\ q_1 & \text{for } u_1 \leq u \leq u_2 \\ q_1 - (u-u_2)(q_1-q_3)/(u_3-u_2) \geq q_3 & \text{for } u > u_2 \end{cases} \quad (6\text{-}3)$$

where: $q$ = bond stress;

$u$ = slip; and for a concrete with compressive strength of about 4,000 psi (about 30 MPa):

$u_1$ = 0.394 in. (1.0 mm) for confined concrete

= 0.0118 in. (0.3 mm) for unconfined concrete in tension;

$u_2$ = 0.118 in. (3.0 mm) for confined concrete

= 0.0118 in. (0.3 mm) for unconfined concrete in tension;

$u_3$ = 0.413 in. (10.5 mm) for confined concrete

= 0.0394 in. (1.0 mm) for unconfined concrete in tension;

$q_1$ = 1,960[(3.5-$d_b$)/2.5] (psi) for confined concrete with $d_b$ in inches

= 13.5[(89-$d_b$)/63.5] (MPa) for confined concrete with $d_b$ in mm

= 725[(3.5-$d_b$)/2.5] (psi) for unconfined concrete in tension with $d_b$ in inches

$= 5[(89-d_b)/63.5]$ (MPa) for unconfined concrete in tension with $d_b$ in mm;

$q_3$ = 725 psi (5 MPa) for confined concrete

= 0 for unconfined concrete in tension;

$d_b$ = bar diameter.

The constitutive model for spring representing 90° standard hooks was presented earlier ( see Eqn. 6-1 and Figure 6.10). A bilinear model was used in this study to represent the steel sress-strain relationship. The strain hardening modulus was assumed to be 1.7% of the elastic modulus in this model.

The validity of the above anchored bar model was checked through comparison of its predictions with test results reported in Ref. 37(a). This reference has presented experimental pull-out force displacement relationships for deformed bars anchored by 90° hooks in confined concrete specimens [Figure 6.3(a)]. Concrete compressive strength in these tests was about 4,000 psi (about 30 MPa), and steel yield strength was 65,000 psi (450 MPa). Figure 6.13 shows a comparison of test results on two different sizes of anchored bars with analytical predictions based on the physical model shown in Figure 6.12. The model is observed to be capable of predicting test results with a reasonable accuracy.

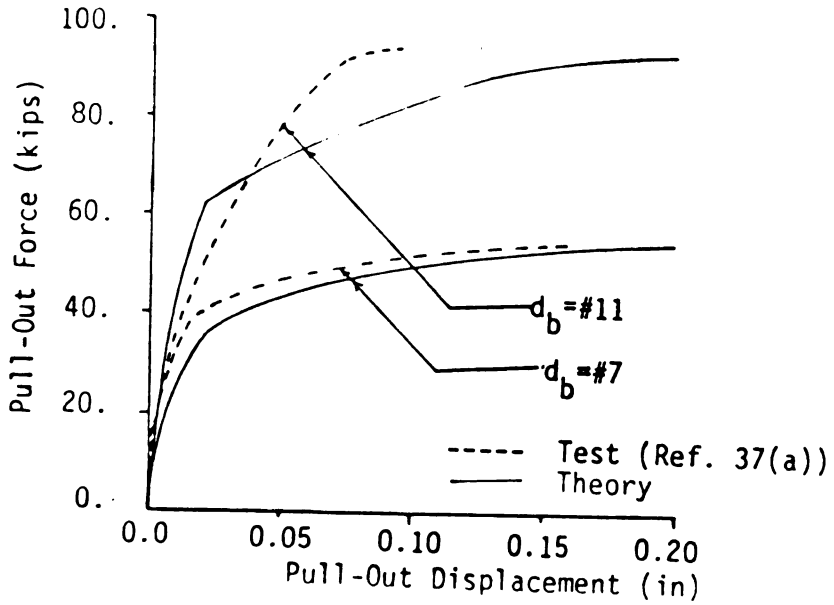


Figure 6.13 Comparison of Test [Ref. 37(a)] and Theory. (1 in. = 25.4 mm; 1 kip = 0.445 KN).

The above analytical model of hooked bars was also used to evaluate the new ACI code[1] requirements for anchorage of deformed bars by standard hooks. ACI code (318-83)[1] suggests the following equation for basic development length of hooked bars:

$$l_{hb} = 1200\, d_b / \sqrt{f_c'} \qquad (6\text{-}3)$$

where: $l_{hb}$ = basic development length (in.);

$d_b$ = bar diameter (in.);

$f_c'$ = concrete compressive strength (psi);

For well-confined concrete, the basic development length shall be multiplied by a modifying factor of 0.8 . Following these ACI guidelines, grade 60 hooked bars #6, #8, and #10 require development lengths of 12 in. (305 mm),

15 in. (381 mm), and 19 in (483 mm), respectively, when embedded in confined concrete with compressive strength of 4,000 psi (27.6 MPa). Hooks with these devopment lengths were modeled as shown in Figure 6.12, and the constitutive models of bond and hook given Eqns. (6-1) and (6-2) were utilized for deriving pull-out force-displacement relationships of hooked bars. The analytical results presented in Figure 6.14 for hooked bars #6, #8, and #10, respectively, indicate that if the current ACI requirements for development of 90° standard hooks in tension are followed, a satisfactory ductile behavior will be achieved in which the bar yields before the anchorage fails.

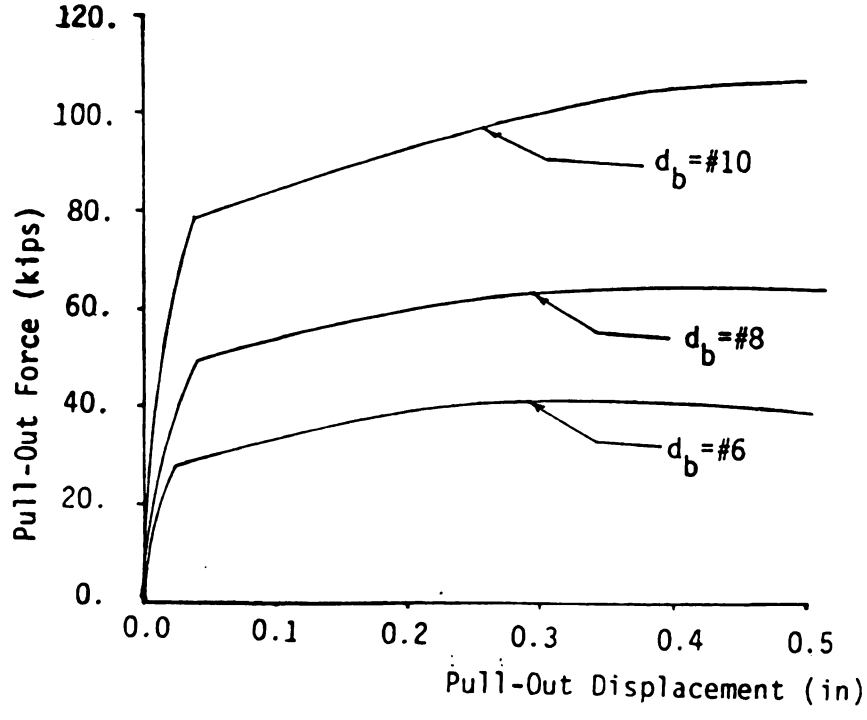


Figure 6.14: Effect of Bar Diameter.
(1 in. = 25.4 mm; 1 kip = 0.445 KN).

# CHAPTER 7

## SUMMARY AND CONCLUSIONS

An integrated experimental-theoretical investigation was performed on the cyclic dowel and pull-out behavior of beam longitudinal bars at beam-column connections. The results are expected to facilitate consideration of fixed-end rotation and sliding shear deformation of beams in seismic analysis of reinforced concrete structures. A summary of the major activities and findings of the research project is presented in the following:

DOWEL ACTION OF BEAM LONGITUDINAL BARS AT BEAM-COLUMN INTERFACES: Monotonic cyclic tests were performed on different sizes of dowel bars. The tested specimens simulated behavior of dowel bars in monotonic action against beam core and cover, and in cyclic action. The beam on an elastic foundation theory together with test results were used to develop formulation for dowel strength and load-deflection relationships in action against cover and core, and for hysteretic rules governing the cyclic behavior of dowel bars. The results indicated that:

- In action against beam core, the ultimate strength was reached when a split crack appeared in the plane of dowel bar and load. The major factors influencing behavior of dowel bars in action against core include bar diameter, and to a lesser extent its yield strength. The effect of concrete compressive strength was relatively small;

- In dowel action against cover beam cover, the stiffness dropped when a split crack separated the concrete cover from the core. The ultimate load was reached when the stirrup located near the point of dowel load application yielded. Before split cracking, dowel bars acting against cover behaved similar to the ones against core. After split cracking, however, the action against cover was more flexible;
- Cyclic application of dowel load resulted in severe degradation of dowel bars stiffness and energy absorption capacity. Dowel strength, however, did not deteriorate under cyclic loads, except for very small dowel bars, and the hysteretic envelope practically coincided with the monotonic dowel load-deflection diagrams. The interface crack width was also observed to grow with repeated application of load cycles.

**PULL-OUT BEHAVIOR OF BEAM LONGITUDINAL BAR BONDED IN BEAM-COLUMN CONNECTIONS**: A new modeling technique based on the displacement method of analysis was developed for predicting the behavior of deformed bars anchored in concrete. In this model, the bond between steel and concrete was simulated by discrete springs connecting the bar to concrete along the anchorage length. Unlike the other available analytical models of anchored bars that require iterative solution of the governing nonlinear equations, the proposed approach is non-iterative and it

involves construction of the tangent stiffness matrix of the anchorage model at each load step. This technique is time-efficient for computer analysis, and its predictions were shown to compare well with test results. A parametric study was performed on the pull-out behavior of beam longitudinal bars embedded in interior beam-column connections using the model developed. The results indicated that:

- With increasing bar diameter and yield strength, the pull-out strength increased but the ductility decreased. This can be illustrated by the observation that slip distribution along the embedded length of bars with larger diameter and yield stength tends to be more uniform;
- Increase in concrete compressive strength and column pressure resulted in slight improvements in pull-out behavior that do not appear to be of practical significance;
- The anchored bar pull-out strength increased with increasing loading rate. This increase was in general less than the corresponding increase in the bar yield strength. As a result, anchored bars that yield before pulling out under quasi-static loads might fail by pull-out under dynamic loads. This effect is not desirable and results in loss of energy absorption capacity.

BEHAVIOR OF BEAM LONGITUDINAL BARS HOOKED IN BEAM-COLUMN CONNECTIONS: Pull-out tests were performed on 90° standard hooks anchored in confined concrete specimens that simulated external beam-column connections. The effects of anchored bar diameter, confinement of concrete surrounding the hook, and concrete compressive strength on the hook behavior were studied experimentally. Empirical formulations were also developed for the hook pull-out force-displacement relationship and they were incorporated into a physical model for predicting the pull-out force-displacement relationship of beam longitudinal bars hooked in exterior beam-column connections. The results of analytical approach compared well with test results, and it was used to check adequacy of current ACI requirements for development of 90° standard hooks in tension.

From the experimental and analytical results it could be concluded that:

- The hook pull-out resistance increases with increasing bar diameter, but this increased was lower than the corresponding rise in the bar yield force;
- Better confinement of concrete surrounding the hook also improved the hook behavior.
- Under monotonic pull-out forces, the ACI design guidelines resulted in hooks with a satisfactory ductile behavior.

## REFERENCES


1. American Concrete Institute,"Building Code Requirements for Reinforced Concrete," ACI 318-83, Nov. 1983, 102pp.

2. ACI-ASCE Committee 352,"Recommendations For Design of Beam-Column Joints in Monolithic Reinforced Concrete Structures," Jounal of the American Concrete Institute, Vol. 82, No. 3, May-June 1985, pp. 266-283.

3. Aktan, A.E.; and Bertero, V.V.,"State of the Art and Practice in the Optimum Seismic Design and Analytical Response Prediction of R/C Frame-Wall Structures," Report No. UCB/EERC-82/06, Earthquake Engineering Research Center, University of California, Berkeley, July 1982.

4. Al-Mahaidi, R.H.,"Nonlinear Finite Element Analysis of Reinforced Concrete Deep Members," A Thesis Presented to the Faculty of the Graduate School of Cornell University in Partial Fulfillment for the Degree of Doctor of Philosophy, May 1978, 374 pp.

5. Aristizabaln-Ochoa, J.D.; Shiu, K.N.; and Corley, W.G., "Effects of Beam Strength and Stiffness on Coupled Wall Behavior," Proceedings of the Second U.S. National Conference on Earthquake Engineering, Stanford University, Stanford, California, 1979, pp. 323-332.

6. Bannon, H.; Biggs, J.M.; and Irvine, H.M., "Seismic Damage Concrete Frames," Journal of the Structural Division, American Society of Civil Engineers, Vol. 127, No. ST9, sept. 1981.

7. Barney, G.B.; Shiu, K.N; Rabbat, B.G.; Fiorato, A.E.; Russel, H.G.; and Corley, W.G.,"Behavior of Coupling Beams Under Load Reversals," Research and Development Bulletin RD068.01B, Portland Cement Association, 1980.

8. Bauman, T., "Versuche Zum Studium der Verdubelungswirking der Biegezuberwehrung eines Stahlbetonbalken," Material Prufungsamt fur das Vauwesen der Technishen Hochschule, Munchen, Bericht, No. 77 (in German).

9. Bertero, V.V., "Seismic Behavior of Structural Concrete Linear Elements (Beams, Columns), and Their Connections," Structural Concrete Under Seismic Actions, AICAP Symposium, CEB, Rome, April 1979.

10. Charney, F.A.; and Betero, V.V.,"An Evaluation of the Design and Analytical Seismic Response of A Seven-Story Reinforced Concrete Frame-Wall Structure," Report No. UCB/EERC-82/08, Earthquake Engineering Research Center,

University of California, Berkeley, July 1982.

11. Ciampi, V.; Eligehausen, R.; Bertero, V.V.; and Popov, E.P., "Analytical Model For Concrete Anchorage of Reinforcing Bars Under Generalized Excitations," Report No. UCB/EERC-82/23, Earthquake Engineering Research Center, University of California, Berkeley, Nov. 1982, 111 pp.

12. Cowell, A.D.; Popov, E.P.; and Bertero, V.V., "Effect of Concrete Type and Loading Conditions on Local Bond-Slip Relationships," Report No. UCB/EERC-82/17, Earthquake Engineering Center, University of California, Berkeley, Sept. 1982, 62 pp.

13. Den Hartog, J.P., "Advanced Strength of Materials," McGraw-Hills Book Company, Inc., New York, 1952.

14. Dulacska, H., "Dowel Action of Reinforcement Crossing Cracks in Concrete," Journal of the Americaan Concrete Institute, Vol. 69, No. 12, Dec. 1972, pp. 754-757.

15. Durrani, A.J.; and Wight, J.K., "Behavior of Interior Beam-to-Column Connections Under Earthquake-Type Loading," Journal of the American Concrete Institute, Vol. 82, No. 3, May-June 1985, pp. 343-349.

16. Ehsani, M.R.; and Wight, J.K., "Effect of Transverse Beam-to-Column Connections," Journal of the American Concrete Institute,Vol. 82, March-April 1985, pp. 188-195.

17. Ehsani, M.R.; and Wight, J.K., "Exterior Reinforced Concrete Beam-Column Connections Subjected to Earthquake-Type Loading," Journal of the American Concrete Institute, Vol. 82, No. 4, July-August 1985, pp. 492-499.

18. Eleiott, A.F, "An Experimental Investigation of Shear Transfer Across Cracks in Reinforced Concrete," M.S. Thesis, Cornell University, June 1974.

19. Eligehausen, R., Popov, E.P.; and Bertero, V.V., "Local Bond Stress-Slip Relationships of Deformed Bars Under Generalized Excitations, Test and Analytical Model, " Report No. UCB/EERC-83/23, Earthquake Engineering Research Center, University of California, Berkeley, Oct. 1983, 170 pp.

20. Eligehausen, R.; Bertero, V.V.; and Popov, E.P., "Hysteretic Behavior of Reinforcing Deformed Hooked Bars in R/C Joints," 7$^{th}$ European Conference on Earthquake Engineering, Athens, Sept. 1982, pp. 69-80.

21. Fardis, M.N.; and Buyukozturk, O., "Shear Stiffness of Concrete By Finite Element," Journal of the Structural Division, American Society of Civil Engineering, Vol. 106, No. ST6, June 1980, pp. 1311-1327.

22. Fenwick, R.C., "The Shear Strength of the Reinforced Concrete Beams," Ph.D Thesis, University of Canterbury, Christchurch, NewZealand, 1966.

23. Filippou, F.C.; Popov, E.P.; and Bertero, V.V., "Effect of Bond Deterioration on the Hysteretic Behavior of R/C Joints," Report No. UCB/EERC-83/19, Earthquake Engineering Research Center, University of California, Berkeley, Aug. 1983, 184 pp.

24. Friberg, B.F., "Design of Dowels in Transverse Joints of Concrete Pavements," Transactions, American Society of Civil Engineers, Vol. 105, 1940, pp. 1809-1828.

25. Gosain, N.K.; Brown, R.H.; and Jirsa, J.O., "Shear Requirements For Load Reversals On R/C Members," Journal of Structural Division, American Society of Civil Engineers, Vol. 103, ST7, July 1977, pp. 1461-1476.

26. Hanson, N.W.; and Connor, H.W., "Seismic Resistance of Reinforced Concrete Beam-Column Joints," Journal of the Structural Division, American Society of Civil Engineers, Vol. 93, No. ST5, October 1967, pp. 533-560.

26(a). Hawkins, N.M., "The Bearing Strength of Concrete for Strip Loadings," Magazine of Concrete Research (London), Vol. 22, No. 71, June 1970, pp. 87-98.

27. Houde, J., "Study of Force-Displacement Relationship for the Finite Element Analysis of Reinforced Concrete," Structural Concrete Series, No. 73-2, McGill University, Montreal, December 1973.

28. Ismail, M.A.F.; and Jirsa, J.O., "Bond Deterioration in R/C Subjected to Low Cycle Load," Journal of the American Concrete Institute, Vol. 69, No. 6, June 1972,

pp. 334-343.

29. Jimenez-Perez, R.; Gergeley, P.; and White, R.N., "Shear Transfer Across Cracks in Reinforced Concrete," Report 78-4, Dept. of Structural Engineering, Cornell University, Aug. 1978.

30. Jimenez-Perez, R.; White, R.N., and Gergely, P., "Bond and Dowel Capacities of Reinforced Concrete," Jounal of the American Concrete Institute, Vol. 76, No. 1, June 1979, pp. 73-92.

31. Johnston, D.W.; and Zia, P., "Analysis of Dowel Actions," Journal of the American Society of Civil Engineers, Vol. 97, No. ST5, May 1971, pp. 1611-1630.

32. Kemp, E.C; and Wilhelm, W.J., and Chen, N.J., "An Investigation of the Parameters Influencing Bond Behavior With a View Towards Establishing Design Criteria," Final Report, WVDOH Project No. 46, Report No. FHWA-WV-77-6, Dept. of Civil Engineering, West Virginia University, Morgantown, WV, November 1, 1977.

33. Keshavarzinn, M.; and Schnobrich, W., "Computed Nonlinear Seismic Response of R/C Wall-Frame Structures," Civil Engineering Studies, Structural Research Series No. 515, University of Illinois, Urbana-Champaign, May 1984, 219 pp.

34. Krefeld, W.J.; and Thurston, C.W., "Contribution of Longitudinal Steel to Shear Resistance of Reinforced Concrete Beams," Journal of the American Concrete Institute Vol. 63, No. 3, March 1966, pp. 325-344.

35. Lee, D.C.N.; Wight, M.; and Hanson, R.D., "RC Beam-Column Joints Under Large Load Reversals," Journal of the Structural Division, American Society of Civil Engineers, Vol. 103, No. ST12, December 1977, pp. 2337-2350.

36. Ma, S.M; Bertero, V.V.; and Popov, E.P., "Experimental and Analytical Studies on the Hysteretic Behavior of R/C Rectangular and T-Beams," Report No. UCB/EERC-76/02, Earthquake Engineering Research Center, University of California, Berkeley, May 1976, 254 pp.

37. Marcus, H., "Load Carrying Capacity of Dowel At Transverse Pavement Joints," Journal of the American Concrete Institute, Vol. 23, No. 2, Oct. 1983, pp. 169-184.

37(a). Marques, J.L.G; and Jirsa, J.O., "A Study of Hooked Bar Anchorages in Beam-Column Joints," Journal of the American Concrete Institute, Vol. 72, No. 5, May 1975, pp. 198-209.

38. Meinheit, D.F.; and Jirsa, J.O., "Shear Strength of R/C Beam-Column Connections," Journal of the Structural Division, American Society of Civil Engineers, Vol. 107, No. ST11, November 1981, pp. 2227-2244.

38(b). Mills, G.M., "A Partial Kinking Yield Criterion for Reinforced Concrete Slabs," Magazine of Concrete Research (London), Vol. 27, No. 90: March 1975, pp. 13-22.

38(c). Minor, J.; and Jirsa, J.O., "Behavior of Bent-Bar Anchorages," Journal of the American Concrete Institute, Vol. 72, No. 4, April 1975, pp. 141-149.

39. Morita, S.; and Kaku, T., "Local Bond Stress-Slip Relationships Under Repeated Loading," Proceedings, IABSE Symposium on Resistance and Ultimate Deformability of Structures on by Well Defined Repeated Loads, Lisbon, 1973, pp. 221-226.

40. Oesterle, R.G.; Aristizabal-Ochoa, J.D; Shiu, K.N.; and Corley, W.G., "Web Crushing of R/C Structural Walls," Journal of the American Concrete Institute, Vol. 61, No. 3, May-June 1984, pp. 231-241.

41. Paulay, T., "Simulated Seismic Loading of Spandrel Beams," Journal of the Structural Division, American Society of Civil Engineers, Vol. 97, No. ST9, Sept. 1971, pp. 2407-2419.

42. Paulay, T.; Park, R.; and Philips, M.H., "Horizontal Construction Joints in Cast-in-Place Reinforced Concrete," Shear in Reinforced Concrete, Vol. 2, Special Publication SP-42, American Concrete Institute, Detroit, MI, 1974, pp. 599-616.

43. Paulay, T.; Priestley, M.J.N; and Synge, A.J., "Ductility in Earthquake-Resisting Squat Shear Walls," Journal of the American Concrete Institute, Vol. 9, No. 4, July-August 1982, pp. 257-269.

44. Popov, E.P., "Bond and Anchorage of Reinforcing Bars Under Cyclic Loadings," Journal of the American Concrete Institute, Vol. 81, No. 4, July-August 1984, pp. 340-349.

45. Ramirez, H.; and Jirsa, J.O, "Effect of Axial Load on Shear Behavior of Short R/C Columns Under Cyclic Lateral Deformation," PMFSEL Report No. 80-1, Phil., M. Ferguson Structural Engineering Laboratory, The University of Texas at Austin, June 1980, 162 pp.

46. Scibner, C.F.; and Wight, J.K., "Delaying Shear Strength Decay in R/C Flexural Members Under Large Load Reversals," Report UMEC 78R2, Department of Civil Engineering, The University of Michigan, Ann Arbor, 1978.

47. Sharma, N.K., "Splitting Failures in Reinforced Concrete Members," Ph.D Thesis, Dept. of Structural Engineering, Cornell University, Ithaca, N.Y., June 1969.

48. Shipman, J.M.; and Gerstle, K.H, "Bond Deterioration in Concrete Panels Under Load Cycles," Journal of American Concrete Institute, Vol. 76, No. 2, Feb. 1979, pp. 311-325.

49. Soleimani, P.; Popov, E.P.; and Bertero, V.V., "Hysteretic Behavior of R/C Beam-Column Subassemblages," Journal of the American Concrete Institute, Vol. 76, No. 11 November 1979, pp. 1179-1195.

49(a). Soroushian, P.; and Choi, K., "Steel Mechanical Properties at Different Strain Rates," Journal of Structural Division, American Society of Civil Engineers (Under Review).

50. Stanton, J., "The Dowel Action of Reinforcement and the Nonlinear Dynamic Analysis of Concrete Nuclear Containment Vessels," M.S. Thesis, Cornell University, August 1976.

51. Takayanagi, T.; and Schnobrich, W.C, "Computed Behavior of Reinforced Concrete Coupled Shear Walls," Civil Engineering Studies, Structural Research Series, No. 434, University of Illinois, Urbana-Champaign, December 1976.

52. Tassios, T.P., "Properties of Bond Between Concrete and Steel Under Load Cycles Idealizing Seismic Actions," Structural Concrete Under Seismic Action, AICAP Symposium, CEB, Rome, April 1979.

53. Tassios, T.P.; and Yannopoulus, P.S., "Analytical Studies on Reinforced Concrete Members Under Cyclic Loading Based on Bond Stress-Slip Relationships," Journal of the American Concrete Institute, Vol. 78, No. 3, May-June 1981, pp. 206-216.

54. Taylor, H.P.S., "The Fundamental Behavior of Reinforced Concrete Beams in Bending and Shear," Shear in Reinforced Concrete, Vol. 1, Special Publication SP-42, American Concrete Institute, Detroit, MI, 1974, pp. 43-77.

55. Vallenas, J.M.; Bertero, V.V.; and Popov, E.P., "Hysteretic Behavior of Reinforced Concrete Structural Walls," Report No. UCB/EERC-79/10, Earthquake Engineering Research Center, University of California, Berkeley, August 1979.

56. Viwathanatepa, S.; Popov, E.P.; and Bertero, V.V., "Effects of Generalized Loadings on Bond of Reinforcing Bars Embedded in Confined Concrete Blocks," Report No. UCB/EERC-79/22, Earthquake Engineering Research

Center, University of California, Berkeley, August 1979.

57. Wagner, M.T.; and Bertero, V.V., "Mechanical Behavior of Shear Wall Vertical Boundary Members: An Experimental Investigation," Report No. UCB/EERC-82/18, Earthquake Engineering Research Center, University of California, Berkeley, October 1982.